

MESSENGER Observations of Cusp Plasma Filaments at Mercury

Gangkai Poh¹, James A. Slavin¹, Xianzhe Jia¹, Gina A. DiBraccio², Jim M. Raines¹, Suzanne M. Imber^{1,3}, Daniel J. Gershman^{1,4}, Wei-Jie Sun⁵, Brian J. Anderson⁶, Haje Korth⁶, Thomas H. Zurbuchen¹, Ralph L. McNutt, Jr.⁶, and Sean C. Solomon^{7,8}

¹ Department of Atmospheric, Oceanic and Space Sciences, University of Michigan, Ann Arbor, Michigan, USA,

² Solar System Exploration Division, NASA Goddard Space Flight Center, Greenbelt, Maryland, USA,

³ Department of Physics and Astronomy, University of Leicester, Leicester, United Kingdom,

⁴ Heliophysics Science Division, NASA Goddard Space Flight Center, Greenbelt, Maryland, USA,

⁵ School of Earth and Space Sciences, Peking University, Beijing, China

⁶ The Johns Hopkins University Applied Physics Laboratory, Laurel, Maryland, USA,

⁷ Lamont-Doherty Earth Observatory, Columbia University, Palisades, New York, USA,

⁸ Department of Terrestrial Magnetism, Carnegie Institution of Washington, Washington, District of Columbia, USA,

Abstract

This is the author manuscript accepted for publication and has undergone full peer review but has not been through the copyediting, typesetting, pagination and proofreading process, which may lead to differences between this version and the [Version of Record](#). Please cite this article as doi: [10.1002/2016JA022552](https://doi.org/10.1002/2016JA022552)

The MESSENGER spacecraft while in orbit about Mercury observed highly localized, ~3-s-long reductions in the dayside magnetospheric magnetic field, with amplitudes up to 90% of the ambient intensity. These magnetic field depressions are termed cusp filaments because they were observed from just poleward of the magnetospheric cusp to mid-latitudes, i.e., ~55° to 85° N. We analyzed 345 high- and low-altitude cusp filaments identified from MESSENGER magnetic field data to determine their physical properties. Minimum variance analysis indicates that most filaments resemble cylindrical flux tubes within which the magnetic field intensity decreases toward its central axis. If the filaments move over the spacecraft at an estimated magnetospheric convection speed of ~35 km/s, then they have a typical diameter of ~105 km or ~7 gyro-radii for 1 keV H⁺ ions in a 300 nT magnetic field. During these events, MESSENGER's Fast Imaging Plasma Spectrometer observed H⁺ ions with magnetosheath-like energies. MESSENGER observations during the spacecraft's final low-altitude campaign revealed that these cusp filaments likely extend down to Mercury's surface. We calculated an occurrence-rate-normalized integrated particle precipitation rate onto the surface from all filaments of $(2.70 \pm 0.09) \times 10^{25} \text{ s}^{-1}$. This precipitation rate is comparable to published estimates of the total precipitation rate in the larger-scale cusp. Overall, the MESSENGER observations analyzed here suggest that cusp filaments are the magnetospheric extensions of the flux transfer events that form at the magnetopause as a result of localized magnetic reconnection.

1. Introduction

Since the discovery by Mariner 10 that Mercury possesses an intrinsic dipolar magnetic field [Ness *et al.*, 1974], much interest has been focused on the interaction between the solar wind and Mercury's small magnetosphere. The MErcury Surface, Space ENvironment, GEochemistry, and Rangin (MESSENGER) spacecraft was the first to orbit Mercury. It provided magnetic field [Anderson *et al.*, 2007] and plasma ion [Andrews *et al.*, 2007] measurements to characterize magnetospheric structure and dynamics at Mercury [Anderson *et al.*, 2008; Slavin *et al.*, 2009; Raines *et al.*, 2014]. With these data, a number of discoveries have been made about Mercury's magnetosphere and its interaction with the solar wind. We now know that Mercury's dipole moment is offset in the northward direction by 484 ± 11 km [Alexeev *et al.*, 2010; Anderson *et al.*, 2011; Johnson *et al.*, 2012; Winslow *et al.*, 2014]. The planet's magnetosphere is small, with a standoff distance from Mercury's center that averages $1.45 R_M$ [Winslow *et al.*, 2013], where R_M is Mercury's radius (2440 km), and decreases to less than $1.1 R_M$ during coronal mass ejections (CMEs) [Slavin *et al.*, 2014]. Because of Mercury's close proximity to the Sun, the solar wind not only has higher dynamic pressure, but also has lower plasma β – the ratio of plasma thermal pressure to magnetic pressure – and Alfvénic Mach number than typically seen at Earth. These conditions produce a thick plasma depletion layer in the magnetosheath, adjacent to the dayside magnetopause [Gershman *et al.*, 2013] as well as high rates of magnetopause reconnection [Slavin and Holzer, 1979; Slavin *et al.*, 2009; DiBraccio *et al.*, 2013]. The solar wind interaction with Mercury also produces frequent, large flux transfer events (FTEs) observed from the subsolar region to the high-latitude magnetopause downstream of the cusp [Slavin *et al.*,

2009, 2010, 2012; *Imber et al.*, 2014]. Fully developed Kelvin-Helmholtz waves are observed along the low-latitude magnetopause, but only along the dusk flank [*Boardsen et al.*, 2010; *Sundberg et al.*, 2012; *Liljeblad et al.*, 2014; *Gershman et al.*, 2015].

The magnetospheric cusps separate the closed dayside magnetic flux at lower latitudes from the open flux tubes in the polar caps that map to the north and south lobes of the magnetotail. The cusp is characterized by newly opened magnetic flux that is created by magnetic reconnection at the dayside magnetopause and moves poleward to join the high latitude magnetotail. Along the flux tubes that transit the cusp, plasma flows from reconnection sites at the magnetopause toward the surface. A portion of this plasma mirrors at low altitude and moves back up the flux tube to form the plasma mantle, just inside the magnetopause tailward of the cusp [*Hill and Reiff*, 1977; *Newell and Meng*, 1987; *DiBraccio et al.*, 2015]. Planetary magnetospheric cusps are important because they are one of the sites for solar wind mass and energy transfer into the magnetosphere. Recent studies of Mercury's cusps [*Winslow et al.*, 2014; *Raines et al.*, 2014] suggest that such regions also play an important role in magnetosphere-surface interaction as sites for the upward escape of sputtered Na^+ .

Slavin et al. [2014] first reported observations of discrete diamagnetic field decreases, lasting only a few seconds in duration, on top of the average cusp diamagnetic depression during the CME event observed by MESSENGER on 23 November 2011. The structures corresponding to these short-term field changes were termed “cusp plasma filaments” to reflect their occurrence within and in the region surrounding Mercury's cusp. *Slavin et al.*, [2014] hypothesized that the

filaments were diamagnetic in origin and caused by the injection of magnetosheath plasma into discrete flux tubes by reconnection at the magnetopause. The maximum field decrease in these filaments was observed to be ~ 200 nT, equivalent to ~ 16 nPa of plasma pressure [Slavin *et al.*, 2014]. To date, such large-amplitude filamentary structures within a cusp region have not been observed at planets other than Mercury.

This paper aims to answer the following questions. What is the magnetic structure of cusp filaments? What are the spatial and temporal ranges of their physical properties? How frequently are they observed? What are the characteristics of the plasma responsible for the diamagnetic reduction in their core field? How are cusp filaments related to the FTEs observed at the magnetopause? Do these filaments extend to low altitudes, and do they reach the surface? What is the flux of ions precipitating to the surface from the filaments and what is their aggregate contribution to the solar wind flux to the surface? What aspects of the solar wind lead to cusp filament formation?

The paper is organized as follows. In the next section we summarize a survey of 3 years of MESSENGER magnetic field observations for the presence of cusp filaments conducted with a scale-free quantitative identification method. In section 3 we present the minimum variance analysis (MVA) applied to each filament event to infer mean orientation and magnetic structure. In section 4 we summarize an examination of the first 3 months of magnetic field data from MESSENGER's end-of-mission low-altitude campaign, i.e., August through October 2014, a period during which the spacecraft periapsis was within 50 km of Mercury's surface. In section 5

we summarize the outcome of statistical analyses performed to determine the physical properties and geographic distribution of the filaments inferred from combined high- and low-altitude data. In section 6 we provide an estimate of the flux of ions that precipitate onto Mercury's surface and an assessment of upstream solar wind conditions as a guide to the factors that influence filament formation. We conclude that the filaments are most likely the low-altitude extensions of FTEs occurring at the dayside magnetopause, and the plasma within each filament adds to the total plasma flux precipitating onto Mercury's surface.

2. MESSENGER Instrumentation and Cusp Filament Identification

In this study, we use the full-resolution measurements from MESSENGER's Magnetometer (MAG) (20 samples/s) and Fast Imaging Plasma Spectrometer (FIPS) (1 energy scan every 10 s), both data sets of which are available for all cusp crossings and the entire orbital mission. We surveyed the orbits during which the spacecraft traversed the average cusp location [Winslow *et al.*, 2012]. We selected orbits during which MESSENGER traversed the dayside magnetopause within 5.5–15.5 h of magnetic local time (MLT) to ensure that the magnetic signatures observed in the cusp are not related to other flank magnetopause dynamic phenomena such as Kelvin-Helmholtz waves.

An example of magnetic field data acquired along a MESSENGER orbit during an interval when no cusp plasma filaments were seen (on 26 August 2011) is shown in Figure 1. Figure 1a

shows the example orbit in an aberrated adjustment to the Mercury solar magnetospheric (MSM) coordinate system. In the MSM system, centered on Mercury's internal dipole, the X -axis and Z -axis are sunward and along the northern spin axis, respectively, and the Y -axis completes the right-handed system and is in a direction opposite to that of Mercury's orbital motion. Because of the orbital motion of Mercury with respect to the solar wind, we have accounted for the aberration effect by rotating the MSM coordinate system in the X - Y plane by an aberration angle into the aberrated MSM coordinate system (MSM'). Because of the highly eccentric shape of Mercury's orbit, the aberration angle was calculated on a daily basis under the assumption that the solar wind velocity is radial to the Sun at 400 km/s.

The full-resolution magnetic field measurements along the orbit depicted in Figure 1a are shown in Figure 1b. The magnetic field was relatively quiet during this orbital pass. The interval began with MESSENGER crossing Mercury's magnetotail current sheet (CS) as shown from the reversal in polarity of the X component of the magnetic field vector \mathbf{B} at 20:22 UTC. As MESSENGER moved closer to the planet, the magnetic field strength increased until the spacecraft reached closest approach (CA) where B was at its maximum. The magnetic field showed little fluctuation near this time, indicating that the spacecraft was deep within Mercury's magnetosphere. The spacecraft encountered the northern magnetospheric cusp about 3 min later as evidenced by the broad depression in the magnetic field magnitude. MESSENGER exited the dayside magnetosphere at ~ 21:25:00 UTC and remained in the magnetosheath until it crossed the bow shock into the solar wind at ~ 21:37:00 UTC.

An example of magnetic field data acquired along a MESSENGER orbit during an interval when plasma filaments were seen in the cusp (on 20 May 2011) is shown in Figure 2. Figure 2a displays full-resolution magnetic field measurements acquired from the spacecraft crossing of the magnetotail current sheet through the cusp region and outward thereafter. In addition to observing a magnetic field depression in the cusp similar to that shown in Figure 1b, MESSENGER also recorded short-duration cusp filaments as it flew into the cusp and moved to lower magnetic latitudes. The spacecraft crossed the magnetopause at 10:07:00 UTC and encountered the bow shock at 10:23:00 UTC. MESSENGER also observed large-amplitude fluctuations in B associated with FTEs near the dayside magnetopause in the magnetosheath region [Slavin *et al.*, 2012; Imber *et al.*, 2014]. Figure 2b shows a close-up of the magnetic field measurements in the cusp region. The background magnetic field displays 4-min-long fluctuations around a mean field of ~ 300 nT, behavior consistent with our understanding of plasma diamagnetism in Mercury's magnetospheric cusp [Winslow *et al.*, 2012; Raines *et al.*, 2014]. However, MESSENGER also clearly measured highly localized magnetic field decreases that we identify here as cusp filaments.

We visually identified a total of 63 cusp crossings from March 2011 to May 2015 that contained cusp filaments. For each cusp crossing, we identified the cusp filament events with a scale-free algorithm adapted from the scale-free approach developed by Stevens and Kasper [2007] (hereafter referred as SK07) to identify magnetic holes in the solar wind. The SK07 method is highly applicable to the study here because it uses the decrease of the magnetic field

magnitude B in the identification process, and such a decrease is also the main magnetic signature of cusp filaments. However, it must be made clear that, although the cusp filaments and solar wind magnetic holes possess similar magnetic signatures, their formation process is not believed to be similar.

For each filament, we first determined an amplitude δB and a time duration dt . δB is the decrease in B within the filament and is given by the relation $\delta B = B_0 - B_1$ where B_0 is the magnitude of the ambient magnetic field just outside the filament and B_1 is the minimum field magnitude inside the filament. Previous studies of magnetic holes in the solar wind used arbitrary event selection criteria to determine δB and dt [e.g., *Turner et al.*, 1977; *Winterhalter et al.*, 1994], a procedure that inevitably introduces scaling biases. The study of cusp filaments here faces the same challenge, i.e., accurately determining both parameters without introducing significant bias. For the cusp filaments, the low signal-to-noise ratio in the background magnetic field resulting from intense magnetospheric activity in the cusp introduces additional challenges. Hence, a scale-free identification method is needed to minimize scaling biases.

The process for identifying cusp filaments is illustrated schematically in Figure 3a. To begin the identification process, we divided each cusp-crossing interval into 1-min subintervals. For each 1-min subinterval, there is a time series of B observations at a cadence τ (0.05 s for MESSENGER). Consider a segment T centered on time t within that subinterval that contains n_T measurements and has a total duration dt , where $dt = n_T \tau$. Consider a longer neighborhood segment W also centered on time t and defined so that it contains $n_W = (2s + 1)n_T$

measurements, where s is the isolation factor, an integer representing how isolated each filament must be relative to the adjacent filament to be considered independent. In the SK07 method, a constant value of s is used for the study. In our filament study, the isolation factor is one of two free parameters in the identification process and is allowed to vary for each 1-min subinterval. The choice of s for each subinterval is discussed further below. We define the significance q of segment T relative to its neighborhood segment W as:

$$q(dt, t) = \frac{\langle B \rangle_{W-T} - \langle B \rangle_T}{\sigma_{W-T}} \quad (1)$$

where $\langle B \rangle_T$ is the mean value of B within time segment T , $\langle B \rangle_{W-T}$ is the mean value of B within the time segment w outside of the interval T (segment $W - T$), and σ_{W-T} is the standard deviation of B in that same segment ($W - T$). By varying the size of the time segment T , q is maximized when t and dt coincide with the center and duration of the filament, respectively. If segment T contains no filament, q fluctuates between 1 and -1.

From equation (1), we constructed maps of q as a function of dt and t as shown in Figure 3b for an example cusp crossing at 09:51 UTC on 20 May 2011, with q ranging from -4 to 10 as represented in the color bar. There are six pronounced maxima in q on the map, each corresponding to a sharp decrease in B , i.e. a plasma filament. We also defined a cutoff value q_0 such that only maximum in q less than q_0 is considered to be a “false detection” of a filament resulting from background noise or turbulence. Hence, q_0 is another free parameter. The use of the two free parameters, s and q_0 , optimizes the number of filament events that the algorithm

selects while minimizing the number of false positive detections. For each 1-min subinterval, we determined the best values of the free parameters by running the algorithm through that subinterval for different combinations of s and q_0 . The combination of s and q_0 with the most (least) number of true (false) positive was chosen for that subinterval. For the case in Figure 3b, a value of $s = 3$ and $q_0 = 3.9$ was determined. For such a value of q_0 , the random fluctuations between $t = 15$ s and $t = 28$ s are not detected by the algorithm as filaments. A search algorithm (see the appendix of SK07 for further details) was then applied to identify each maximum in q and its corresponding values of time t_{\max} and duration dt_{\max} as shown in Figure 3b for the example.

The procedure described to this point closely follows the SK07 method. However, because of high-frequency magnetic field fluctuations in Mercury's cusp, the value of dt corresponding to each maximum tends to underestimate the time duration of each filament (see the gray-shaded areas in the bottom panel of Figure 3b). Low-pass filtering of the data could avoid high-frequency magnetic field fluctuations that mask the filament signatures in the selection algorithm. However, we did not elect such an approach as the error associated with low-pass filtering increases with decreasing dt and increasing δB . Hence, instead of using dt_{\max} , we used a value for dt equal to the interval over which q equaled or exceeded half the maximum value of q at time t_{\max} . This estimate for duration $dt_{\text{half-max}}$ is illustrated by the yellow-shaded regions in Figure 3b (the yellow-shaded regions should be understood as also including the gray-shaded regions).

Our scale-free algorithm proved to be effective in identifying filaments for the entire dataset from Mercury. This method is not flawless, however, as it could identify “false positives” or fail to identify candidate filaments (e.g., the candidate filament event at $t = 58$ s in Figure 3b) as a result of the choice of free parameters or background fluctuations in segment $(w - T)$. The first possibility can be remedied by introducing a threshold value of $\delta B/B$. For high-altitude portions of MESSENGER’s orbit, a threshold value of $\delta B/B = 0.05$ was set to filter any false positives identified by the algorithm. As shown in Figure 2b, typical random magnetic field fluctuations are ~ 10 – 15 nT, or ~ 3 – 5% of the background magnetic field (~ 300 nT), so a threshold $\delta B/B$ value of 0.05 is appropriate. We also conducted a sensitivity test of our results on the threshold $\delta B/B$ value, which will be further discussed in Section 5. Although there is no easy fix to the second possibility, there is no loss in generality if some events are missed, given the large number of filaments identified. Since the statistical error is inversely proportional to \sqrt{N} , where N is the total number of events (i.e., 319), the percentage error in our results is no more than 10%. Nevertheless, our scale-free algorithm provides consistency in the selected time interval of each filament, whereas a non-quantifiable random bias would be introduced to our statistical analysis if the selection were done visually.

For most of MESSENGER’s orbital mission, the spacecraft traversed Mercury’s cusp at altitudes between ~ 300 and ~ 700 km, and for these cusp crossings we apply the term high-altitude observations. In late July 2014, MESSENGER’s periapsis altitude fell below 100 km for the first time, and between August and October that year the spacecraft completed multiple

traverses of Mercury's cusp at altitudes less than 100 km. For these cusp crossings we apply the term low-altitude observations. We describe the high-altitude and low-altitude observations of filaments separately in the sections that follow.

3. Analysis Results for High-altitude Filaments

From 62 high-altitude observations, a total of 301 filaments were identified using the algorithm described in the previous section. To understand their magnetic structure, MVA was performed on each filament event over the interval $dt_{\text{half-max}}$. MVA transforms magnetic field measurements from MSM' coordinates into a new orthogonal coordinate system based on the directions of minimum (min), intermediate (int), and maximum (max) variance in the magnetic field measurements [Sonnerup and Cahill, 1967]. The method has been used extensively at Mercury to analyze the orientation of current sheets and other structures [Slavin *et al.*, 2012; DiBraccio *et al.*, 2013; Imber *et al.*, 2014]. The three variance directions were computed by solving the covariance matrix as an eigenvalue problem. The results are three eigenvalues (λ_i) and their corresponding eigenvectors (\mathbf{x}_i), where the subscript i variously represents min, int, or max. The eigenvector with the largest eigenvalue corresponds to the direction with maximum magnetic variance, and so forth. To quantify the errors associated with the eigenvectors, we used the error estimation procedure developed by Sonnerup and Scheible [1998] whereby the angular

rotation uncertainty of eigenvector \mathbf{x}_i to or away from \mathbf{x}_j and the statistical uncertainty in the component of average magnetic field along each eigenvector are given by the following:

$$|\Delta\varphi_{ij}| = \sqrt{\frac{\lambda_3}{(M-1)} \frac{(\lambda_i + \lambda_j - \lambda_3)}{(\lambda_i - \lambda_j)^2}}, \quad i \neq j \quad (2a)$$

$$|\Delta\langle \mathbf{B} \cdot \mathbf{x}_i \rangle| = \sqrt{\frac{\lambda_i}{(M-1)} + \sum_{i \neq j} (\Delta\varphi_{ij} \langle \mathbf{B} \cdot \mathbf{x}_j \rangle)^2} \quad (2b)$$

Ratios of eigenvalues are often used as indicators of the quality of the determination of MVA principal axes. Degeneracy occurs if any two eigenvalues are approximately equal, i.e., when any two orthogonal vectors lying on the plane that contains the two eigenvectors are nearly equally valid as the basis for the MVA coordinate system [Sonnerup and Scheible, 1998]. For this reason, earlier studies that used this technique for magnetopause and flux rope analysis required a minimum eigenvalue ratio of 1.5–5 [Sonnerup and Cahill, 1967; DiBraccio et al., 2013]. Even though degeneracy can lead to large uncertainties in the eigenvectors, it can also be utilized to infer the magnetic structure of the filaments. In this study, we grouped filament events according to their ratios of intermediate to minimum (int/min) and maximum to intermediate (max/int) eigenvalues, and we chose a minimum eigenvalue ratio of 4 for any two eigenvectors to be considered well determined. On the basis of this definition, we identified four different populations of filaments:

1. Population I: $\frac{\lambda_{\text{int}}}{\lambda_{\text{min}}} < 4$ and $\frac{\lambda_{\text{max}}}{\lambda_{\text{int}}} > 4$

2. Population II: $\frac{\lambda_{\text{int}}}{\lambda_{\text{min}}} > 4$ and $\frac{\lambda_{\text{max}}}{\lambda_{\text{int}}} < 4$

3. Population III: $\frac{\lambda_{\text{int}}}{\lambda_{\text{min}}} \sim \frac{\lambda_{\text{max}}}{\lambda_{\text{int}}} > 4$

4. Population IV: $\frac{\lambda_{\text{int}}}{\lambda_{\text{min}}} \sim \frac{\lambda_{\text{max}}}{\lambda_{\text{int}}} < 4$

3.1. Population I

For Population I filaments, the minimum and intermediate eigenvectors are considered to be degenerate (i.e., $\frac{\lambda_{\text{int}}}{\lambda_{\text{min}}} < 4$) on the basis of our chosen threshold, whereas the maximum eigenvector is well determined (i.e., $\frac{\lambda_{\text{max}}}{\lambda_{\text{int}}} > 4$). A total of 130 filament events (~ 43% of the filaments identified) can be classified in this group. Figure 4 shows an example of a typical Population I filament identified on 23 April 2013. The top three panels of the figure show the magnetic field components for this example in MSM' coordinates. B_x and B_y show comparatively small variations and are mostly less than 0 nT, whereas B_z shows a large peak at ~ 16:30:29 UTC. The bottom 4 panels in the figure show the magnetic field in the MVA coordinate system and the total scalar field. The maximum, intermediate, and minimum eigenvectors in MSM' are (0.059, 0.116, 0.992), (-0.998, -0.015, 0.061), and (-0.022, 0.993, -0.115), and the max/int and int/min eigenvalue ratios are 9.70 and 2.11, respectively. The mean values for B_{min} and B_{int} are -1.69 ± 1.59 nT and 8.64 ± 3.50 nT, respectively. B_{min} and B_{int} show

only small variations, but there is a clear unipolar variation in B_{\max} . Figure 4b shows the corresponding max/min and max/int hodograms.

From the magnetic signatures in the MVA coordinate system, we can infer that this filament population is quasi-cylindrically shaped because the magnetic field varies primarily in the maximum direction. Such magnetic structure could be explained with magnetohydrodynamic (MHD) theory and an ideal cylindrical plasma-filled flux tube with the background magnetic field and its invariant axis in the axial direction. From the inverse Gaussian shape of the decrease in the magnetic field magnitude in the filaments, we may infer a Gaussian spatial distribution for the plasma pressure across the flux tube. MESSENGER should have measured regions of weaker field strength toward the center of flux tube because of diamagnetic effects as it traversed the flux tube. In this basic picture of a plasma filament, the direction of maximum variance will be parallel to the axis of the flux tube. Hence, we would expect the maximum eigenvector to have a strong Z-component and be approximately field-aligned. Given plasma homogeneity in the azimuthal and axial (i.e., Z) directions, diamagnetic effects will reduce the field only in the axial direction. Hence, there will be no variance of the field in the minimum and intermediate directions. This degeneracy produces a prolate variance ellipsoid [Sonnerup and Scheible, 1998], independent of the impact parameter, defined as the perpendicular distance between the path of the spacecraft and the center of the flux tube, and the inclination angle at which the spacecraft traverses the flux tube. In this ideal model of a plasma filament, the mean magnetic field along the intermediate and minimum eigenvectors is expected to be ~ 0 nT.

The example shown in Figure 4 has slight average offsets of 0.1 nT and 5.14 nT from 0 nT in the minimum and intermediate directions, respectively. To determine if these offsets are within the errors in the mean of the magnetic field in the direction of the eigenvector, we defined the fraction δ_i as

$$\delta_i = \frac{|\Delta\langle\mathbf{B} \cdot \mathbf{x}_i\rangle|}{|\langle\mathbf{B} \cdot \mathbf{x}_i\rangle|}, i = \min, \text{int}, \max \quad (3)$$

where $|\langle\mathbf{B} \cdot \mathbf{x}_i\rangle|$ is the average magnetic field along the eigenvector \mathbf{x}_i and $|\Delta\langle\mathbf{B} \cdot \mathbf{x}_i\rangle|$ is given by equation 2b. If $\delta_i > 1$, the offset is within the error uncertainty of the average magnetic field whereas $\delta_i < 1$ signifies that the offset is outside the range of the error uncertainty and is likely a real magnetic signature.

A plot of δ_{int} versus δ_{min} for all Population I filament events is shown in the bottom panel of Figure 4b, and the red dashed lines in the figure represents $\delta_i = 1$. The majority of the events have both δ_{int} and $\delta_{\text{min}} \ll 1$, and for only a fraction of events is either δ_{int} or $\delta_{\text{min}} > 1$. Thus for most filaments in this population the offset in the minimum and intermediate direction away from $\langle B_{\text{min}} \rangle = \langle B_{\text{int}} \rangle = 0$ is likely to be “real.” Such a deviation from the ideal cylindrical plasma filament model could be the result of a plasma density gradient in the axial direction arising from variability in magnetic reconnection and energy dispersion of the plasma flowing into the cusp region from the magnetopause, as observed at Earth [Lockwood and Smith, 1989]. Mercury’s cusp is known to be a region of high variability, both spatially and in the distribution of energies [Raines et al., 2014]. Particles with higher energies than the bulk plasma will flow into the cusp

first, followed by the lower-energy particles. Depending on the energy distribution of the accelerated particles from the dayside magnetopause, this difference in timing could result in inhomogeneity in the plasma density along the axis of the filament or sub-structures within the filament. Such an inhomogeneity might create an offset in either or both the minimum and intermediate directions, leading to these filaments departing from a quasi-cylindrical magnetic structure. The 10 s time resolution of FIPS, relative to the 1–2 s duration of these filaments, makes further investigation of this hypothesis difficult.

3.2. Population II

For filaments in Population II, the minimum and intermediate eigenvectors are well determined but the maximum eigenvectors are less well defined. A total of 80 filaments (~ 27% of the filament events) were classified as Population II. Figure 5 shows a typical example of a filament (on 26 July 2013) that satisfies these eigenvalue ratio conditions. The maximum, intermediate, and minimum eigenvectors for this event are (0.396, -0.105, 0.912), (0.331, -0.910, -0.249) and (-0.856, -0.400, 0.326), and the min/int and max/int eigenvalue ratios are 43.90 and 2.27 respectively. The mean values for B_{\min} and B_{int} are 75.66 ± 0.34 nT and 4.91 ± 1.83 nT, respectively.

In a manner similar to the Population I filaments, B_{\min} in Figure 5 shows little variation, but there is a clear unipolar variation in B_{\max} at ~ 17:00:35 UTC. However, there is also a weak

bipolar rotation in B_{int} , and the center of this rotation corresponds to the peak in B_{max} . The bipolar rotation in B_{int} indicates weak magnetic helicity in the flux tube, which we term as “residual twist.” This MVA result is different from that expected for a flux rope, for which B_{max} would show a bipolar signature with a corresponding peak in the intermediate direction because of the presence of a core field [Elphic and Russell, 1983; Xiao et al., 2004]. Since the bipolar rotation is in the intermediate direction, this pattern suggests that Population II filaments are weakly helical structures without a core field.

A plot of δ_{int} versus δ_{min} for all Population II filament events is shown in the bottom panel of Figure 5b. This plot shows that for this population, too, the majority of the events have a significant offset in the mean magnetic field in the intermediate and minimum directions. However, because of the two-dimensional nature of the structure, this offset could be caused by the spacecraft trajectory across the filament, from which we could determine the impact parameter from the center of the filament by solving the MHD pressure balance equation $J \times B = \nabla P$ if the plasma pressure were known.

3.3. Populations III and IV

For Population III and IV filaments, the two eigenvalue ratios are both greater or less than 4, respectively. This means that for the former group the eigenvector basis is well determined, whereas for the latter group it is not. Population III filaments make up 13% of the events

identified in this study, and Population IV filaments make up 17%; therefore, each of these groups is less likely to be observed than Populations I or II. Figures 6 and 7 show, respectively, typical examples of Population III (on 27 July 2013) and Population IV (on 23 April 2013) filaments. For the Population III example, the maximum, intermediate, and minimum eigenvectors are (0.500, -0.179, 0.847), (0.407, -0.814, -0.413), and (0.764, 0.552, -0.334), the corresponding min/int and max/int eigenvalue ratios are 12.20 and 11.60, and B_{\min} and B_{int} are $\sim 23.75 \pm 2.05$ nT and -0.26 ± 0.970 nT, respectively. For the Population IV example, the maximum, intermediate, and minimum eigenvectors are (-0.374, 0.603, 0.705), (0.418, 0.788, -0.453), and (0.828, -0.125, 0.546), the corresponding min/int and max/int eigenvalue ratios are 2.72 and 2.79, and B_{\min} and B_{int} are $\sim -108.40 \pm 3.58$ nT and 24.38 ± 2.22 nT, respectively.

In the examples for these two populations, B_{\max} shows unipolar rotation with respect to the minimum direction. However, although B_{int} for the Population III filament in Figure 6a shows little variance in the intermediate direction, B_{int} for the Population IV filament in Figure 6b shows a weak rotation with respect to the maximum direction. Analysis of the max-int hodograms for Population III (not shown here) indicates that the MVA results for Population III are similar to those for Population I. This result begs the question of why the MVA magnetic field results are reproducible for these two populations of filaments but the qualities of their eigenvector bases are different. Furthermore, the δ_i plot in Figure 6b shows that the Population III filaments have similar constant offset from near-zero values of $\langle B_{\min} \rangle$ and $\langle B_{\text{int}} \rangle$.

A survey of Population IV filaments shows that there could either be a rotation or no variation in the intermediate direction with respect to the maximum direction. Such an outcome is expected since all the eigenvectors are ill-defined and have high uncertainties. The δ_i plot in Figure 7b is also consistent with the results for Population I and II filaments in that a majority of the events have a significant offset in either the mean intermediate or minimum field. However, this offset might also be an artifact of the high level of uncertainties in the MVA results for these near-degenerate cases of filament events. Care is thus warranted in any inferences on the magnetic structure of these events from the MVA results.

3.4. Flux Ropes

In addition to the 301 filaments, the search algorithm identified 32 flux ropes in the cusp regions. Flux ropes are helical flux tubes with a strong core field formed as a result of multiple X-line reconnection. When MVA is performed on these events, we expect to see the characteristic rotation of the magnetic field in the int-max hodogram with a reverse in polarity of B_{\max} (i.e. bipolar rotation in B_{\max}) [Xiao *et al.*, 2004]. Figure 8 shows the MVA results of a flux rope example identified on 27 April 2013. The max-int hodogram (middle panel) shows a distinct bipolar rotation in the maximum variance direction and a peak in the intermediate variance direction. These MVA signatures are indicative of a flux rope with a core field in the direction of intermediate variance. We calculated the maximum, intermediate, and minimum

eigenvectors to be (0.397, 0.917, -0.026), (0.262, -0.087, 0.961), and (0.879, -0.389, -0.275), and the max/int and int/min eigenvalue ratios to be ~ 4.5 and 18.9, respectively, which indicates that the eigenvectors are well determined. Since the calculated intermediate eigenvector is predominantly in the Z-direction, the axis of the flux rope is field-aligned and occurrences of these flux ropes are likely related to the filaments. This finding has important implications for the formation mechanism for cusp filaments, a topic that will be discussed further below.

3.5. FIPS plasma measurements

Because the duration of each filament, $\sim 1\text{--}2$ s, is less than the ~ 10 s energy scan time for FIPS measurements, we are unable to measure the plasma properties for individual filaments. However, we performed a superposed epoch analysis, which utilizes the portion of the energy spectrum and pitch angle distribution sampled for each filament and adds them together to build the energy-resolved pitch angle distribution of a typical filament. A total of 16 high-altitude filaments were selected for their phasing relative to the start time of a FIPS energy scan, with a ~ 1 s uncertainty in that start time. Figure 9a shows the field-of-view-normalized aggregate energy-resolved pitch angle distribution for the 16 selected filaments, with color representing phase space density (PSD). Note that each pitch angle bin in Figure 9a is sampled by at least one of the 16 filament events selected for this analysis; the white color bins in the energy-resolved pitch angle distribution are energy and pitch angles sampled for which FIPS saw no counts in any of

16 filaments. There is an enhancement in the PSD in the energy range $\sim 0.4\text{--}1$ keV and the pitch angle range $\sim 0\text{--}90^\circ$. Additional analysis indicates that most of the filaments have similar-looking pitch angle distributions, as shown in Figure 9b of PSD versus pitch angle for 11 filament events observed in the energy range $0.5\text{--}1$ keV. Figure 9b shows evidence of systematic pitch angle isotropy for energy between 0.5 and 1 keV. This result is in agreement with the proton reflectometry work of *Winslow et al.* [2014], who observed a near-isotropic proton count between 0° and 90° pitch angle at high latitudes in the cusp. This outcome is consistent with our understanding of filaments filled with plasma of magnetosheath-like energies and pitch-angle-independent flow. This result also supports our idea of filaments as diamagnetic effects of precipitating magnetosheath particles in the cusp region with a non-zero perpendicular fluid velocity.

4. Analysis Results for Low-altitude Filaments

From August to October 2014, MESSENGER completed the first phase of a low-altitude campaign during which the spacecraft's periapsis was less than 100 km above Mercury's surface. The magnetic field measurements during this interval provide us with the opportunity to determine if cusp filaments are found near the surface. During these 3 months, MESSENGER was in its "warm season" orbital configuration during which the trajectory was near the noon-

midnight meridian but periapsis occurred on Mercury's nightside. We identified 18 low-altitude cusp observations with filament activity.

As an example, Figure 10 shows two consecutive cusp crossings on 31 August 2014 in MSM' coordinates. The first orbit showed no filament activity in the cusp region, but filaments were observed in the cusp during the second orbit (Figure 10a). For both orbits, the magnetic field strength increased as the spacecraft flew deeper into the magnetosphere. Because of the low-altitude periapsis, the peak in B was ~ 575 nT compared with the typical value of ~ 300 nT seen during orbits with high-altitude periapses. Under "quiet" conditions when no filaments were observed in the cusp (top panel of Figure 10a), the field strength at lower altitudes was so strong that low-energy ions would have magnetically mirrored at higher altitudes, so the diamagnetic effect of gyrating ions was not observed. In contrast, during "active" conditions (bottom panel of Figure 10a), MESSENGER observed filaments near closest approach. Figure 10b shows a close-up of magnetic field measurements around closest approach. For each filament identified by the algorithm, every decrease in B corresponds to a decrease in the magnitude of B_Z with little variation in B_X or B_Y . Observations of structures with similar magnetic signature as the high-altitude filaments support our idea that we are indeed observing cusp filaments at altitudes as low as 50 km, and most likely the filaments deliver plasma directly to the surface.

As with the analysis of high-altitude cusp crossings, for each low-altitude cusp crossing, we employed the scale-free algorithm to identify cusp filaments. A total of 45 filaments were identified among the 18 low-altitude cusp crossings by the algorithm after applying a threshold

value of $\delta B/B = 0.01$ to filter out false positives. We elected to use a lower threshold value for $\delta B/B$ for low-altitude crossings because the spacecraft was deeper into the cusp region where the diamagnetic effects of ions in the filaments are weaker as a result of the stronger background field and more particles are magnetically mirrored in the deep cusp region. A lower threshold value for low-altitude filaments accounts for this spatial variability. MVA was performed on all filament events, and each event was classified into the populations described in section 3. 27% of the low-altitude filaments were classified as Population I, 40% as Population II, and 33% as Population III filaments. No Population IV filaments, for which the eigenvalues ratios are less than 4, were observed at low altitudes. This last result is not unexpected since the planetary field strength is stronger and filaments with poorly defined magnetic variance directions are less likely to occur at low altitudes.

An example of a Population III filament identified on 15 August 2014 during the low-altitude campaign is shown in Figure 11. For this event, the maximum, intermediate, and minimum eigenvectors are (0.299,0.289,0.910), (-0.156,-0.974,0.161), and (-0.873,-0.303,0.383), and the corresponding eigenvalues are 36.41, 1.76, and 0.13, respectively.

As with the high-altitude filaments, B_{\min} and B_{int} show little or no variation relative to the variation in B_{\max} , and the maximum eigenvalue is predominantly in the Z -direction with the peak in B_{\max} corresponding to the maximum dip in B (Figure 11a). The bottom panel of Figure 11b shows an error analysis plot for all low-altitude Population III filaments similar to those for the high-altitude filaments. All except one of the low-altitude Population III filaments have

Author Manuscript

significant offsets from 0 in $\langle B_{\min} \rangle$ and $\langle B_{\text{int}} \rangle$. This result is again consistent with that for the high-altitude filaments and suggests inhomogeneity in the plasma density distributions at the sites of the low-altitude filaments. The low-altitude filaments in other population groups show MVA results that are similar to those for their high-altitude counterparts, reinforcing the idea that we were observing the same phenomenology at low altitudes. For these energetic ions to be observed deep in the cusp regions, they must have sufficient energy parallel to the local magnetic field to overcome the mirroring effect of the converging field lines deep in the cusp. Observations of filaments at such low altitudes suggest that the energetic ions inside each low-altitude filament have a high probability of precipitating onto Mercury's surface.

We also identified six flux ropes in the low-altitude cusp passes. Not shown here, the hodograms of the low-altitude flux ropes show MVA signatures consistent with the high-altitude flux ropes, with the intermediate eigenvector, corresponding to the central axis of the flux rope, having a large Z-component. The high percentage occurrence of Population II filaments and flux ropes at low altitudes suggests that most of these filaments still possess “residual twist” with or without a core field. This finding challenges our understanding of near-surface magnetic field topology in the cusp region, where the magnetic field vector is expected to be predominantly normal to the surface, particularly at Mercury where the conducting core occupies most of the planet's volume [Smith *et al.*, 2012] and the normal component of the magnetic field has to be continuous across the boundary between the core and the mantle.

5. Physical Properties and Spatial Distribution

For the high- and low-altitude filaments identified, histograms of the parameters δB , $\delta B/B$, and dt , defined by the scale-free algorithm, are displayed in Figure 12a–f. The high-altitude filaments have a mean δB of ~ 56 nT and a mean dt of 3 s, whereas the low-altitude filaments have a mean δB of ~ 20 nT and a mean dt of 2 s. Plasma diamagnetism locally reduces the field intensity inside a filament by an average of $\sim 22\%$ (Figure 12c) and 4% (Figure 12d) for high- and low-altitude observations, respectively. We emphasize that a 4% decrease in field intensity at 50 km above the planet’s surface, where background field fluctuations should be minimal, shows the intensity of the magnetospheric dynamics at Mercury’s northern cusp.

As discussed above, we cannot accurately determine the plasma properties of these several-second-long cusp filaments with FIPS, because of the 10 s cycle time for the instrument. Without plasma measurements, we cannot determine the plasma velocity and hence the size of each filament. However, we can estimate the size of each filament with a simple convection speed model. Under the assumption of conservation of magnetic flux at the polar caps, we can derive an equation for the magnetospheric convection speed at which each filament is drifting across the cusp:

$$v_{\text{filament}} = \frac{\varphi}{L_0 \left(\frac{r}{r_0}\right)^{\frac{3}{2}} B} \quad (3)$$

where r_0 is a reference distance from the center of the dipole magnetic field, L_0 is the diameter of the polar cap at $r = r_0$, φ is the cross polar cap electric potential, and B is the background magnetic field magnitude. The quantities r_0 , L_0 , and φ are calculated to be $\sim 1.3 R_M$, $2 R_M$ [Jia *et al.*, 2015] and 30 kV [Slavin *et al.*, 2009]. This model yields a mean filament velocity of ~ 36 km/s with distribution from ~ 25 to 55 km/s. The estimated velocity is consistent with the convection velocity observed in MHD simulations [Jia *et al.*, 2015]. The observed spatial size of the filaments can be determined by multiplying the velocity for each filament by its corresponding time duration under the assumption that the spacecraft velocity is much smaller than the filament velocity. This assumption is a good one, as the spacecraft velocity across the cusp at apoapsis is typically less than 1–2 km/s ($\sim 0.03\%$ of the mean filament velocity). The statistical results for low- and high-altitude filaments are shown in Figures 12e and 12f normalized to the gyro-radius of a 1 keV proton r_L calculated from the local background magnetic field. The mean gyro-radii for high and low-altitude filaments are ~ 12 km and 6 km, respectively. Figures 12e and 12f show that the high-altitude filaments have a mean size of $\sim 8.5 r_L$ with a maximum of $\sim 35 r_L$, whereas the low-altitude filaments have a somewhat smaller mean size of $\sim 7.1 r_L$ with a maximum of $\sim 30 r_L$. This outcome is consistent with the canonical view that magnetic field lines converge closer to the surface in the cusp region. We also note that this approximation provides only a lower limit on the size of the filaments since we are unable to characterize the impact parameter. Even though this model is a simple one, it nonetheless provides a useful estimate for filament size.

We also calculated the magnetic flux Φ within each filament. Without knowledge of the impact parameter and cross-sectional shape of the filament, we assumed a circular cross-section and that MESSENGER traversed the center of the filament. We then multiplied the mean magnetic field inside each filament by the area of a circle of diameter equal to the size of the filament to estimate the total magnetic flux. Figures 12g and 12h show histograms of the magnetic flux for the high- and low-altitude filaments, respectively. The high-altitude filaments have a mean flux of ~ 3.4 kWb, and the low-altitude filaments have a mean flux of ~ 1.2 kWb. Both histograms also show that the number of filaments identified decays approximately exponentially with respect to magnetic flux. The assumptions that go into our calculation of the magnetic flux impart a large uncertainty to the flux values. Similar to our calculation of the filament size, this method provides only a lower limit on the magnetic flux inside the filaments.

To test the sensitivity of our statistical results in Figure 12 with respect to the threshold $\delta B/B$ value, we increased the threshold $\delta B/B$ value for the high-altitude filaments to 0.1 and calculated the new mean values for the time duration, filament size, and magnetic flux to be ~ 3.03 s, $8.67 R_L$ and 3.57 kWb, respectively. Comparing with the means of the distributions in Figure 12, the new mean values for the time duration, filament size, and magnetic flux are larger by ~ 0.07 s, $0.2 R_L$ and 0.19 kWb, respectively. Since the fractional error in the means for the distributions in Figure 12 is ~ 0.1 – 0.4 , the increase in the mean is, to first order, insensitive to the changes in the threshold $\delta B/B$ value. This result provides further justification for our choice of the threshold $\delta B/B$ values.

Given pressure balance between the total pressure inside a filament and the ambient magnetic pressure, the thermal pressure perpendicular to magnetic field lines inside the filament $P_{\text{th},\perp}$ is given by the equation:

$$P_{\text{th},\perp} = \frac{1}{2\mu_0} (2B_0\delta B - \delta B^2) \quad (4)$$

where B_0 is the ambient magnetic field intensity. For each filament, we calculated $P_{\text{th},\perp}$ from the highest magnetic field intensity before or after the diamagnetic decrease in B as a proxy for B_0 and δB from Figures 12a and 12b. $P_{\text{th},\perp}$ is a good indicator of the strength of a filament (i.e., the amount of plasma within each filament) since it is linearly proportional to the density and perpendicular temperature of the plasma in the filament. Sampling at different altitudes gives us a “three-dimensional” view of the longitudinal and latitudinal variation of the cusp filaments.

The distribution of perpendicular thermal pressure $P_{\text{th},\perp}$ with filament location is illustrated in Figure 13a. The locations of filaments identified in this study shown in Figure 13a are in the aberrated cylindrical coordinates X' and $\rho = [Y'^2 + Z'^2]^{0.5}$. The color plot shows the mean $P_{\text{th},\perp}$ for each position binned every $0.01 R_M \times 0.01 R_M$ with values represented by the color bar displayed. The black dashed lines represent the magnetic latitudinal extent of all filaments identified in this study, a range that agrees well with the latitudinal boundaries of the northern cusp calculated by *Winslow et al.* [2012]. The latitudinal extent of the filaments also decreases with decreasing altitude. This “funneling shape” in the occurrence of cusp filaments is consistent with the downward convergence of magnetic field lines in the cusp.

To explore the variation of $P_{\text{th},\perp}$ with altitude, we averaged the data points over bins of 50 km width (Figure 13b). There is a data gap between 150 km to 250 km altitude because MESSENGER did not sample the cusp at those altitudes on the orbits selected for this study. We then fit a least squares linear relation to the binned data points and calculated the linear correlation coefficient to be ~ -0.55 . The poor linear correlation suggests that $P_{\text{th},\perp}$ does not vary linearly with altitude, although the fact that altitudes within the cusp are not equally sampled by our selected orbits may have contributed. To investigate further this nonlinear dependence of $P_{\text{th},\perp}$ with altitude, we calculated the invariant latitude of each $P_{\text{th},\perp}$ measurement using a simple dipole field, which is a good approximation for altitudes less than 700 km. We then binned the data points into 5° -wide bins of invariant latitude bins between 55° and 80° . Not shown here, the results show that the correlation between $P_{\text{th},\perp}$ and altitude remains poor. This result suggests that the nonlinear dependence of $P_{\text{th},\perp}$ with invariant altitude is not statistical. If the straight line is nonetheless extrapolated to the surface, the average perpendicular thermal pressure of the surface filaments would be ~ 11.5 nPa.

To explore the variation of $P_{\text{th},\perp}$ with magnetic latitude, we divided the points into three altitude ranges; 0–250, 250–500, and 500–750 km (Figure 13c). We then binned the points in 5° -wide latitudinal bins and determined the mean $P_{\text{th},\perp}$ value and its standard error for each bin. Figure 13c shows that the perpendicular thermal pressure increases nonlinearly with latitude at all altitudes. Since $P_{\text{th},\perp}$ is proportional to the plasma density within filaments, the plasma density also increases with latitude, which suggests temporal growth in diamagnetism within the

filaments if we take latitudinal variations as proxies for temporal evolution and assume that temperature is constant with latitude. This result is consistent with the energy dispersion of ions injected into the cusp. The more energetic ions with higher velocities parallel to the background magnetic field will be injected into the polar region first. These “faster” ions, with lower perpendicular energy and higher parallel energy, have a weaker diamagnetic effect on the background field than their “slower” counterparts. Ions with smaller velocities are injected at a later time, which also corresponds to higher latitude as the flux tube convects poleward.

The variation of $P_{th,\perp}$ in the aberrated X - Y plane, and effectively in MLT, is shown in Figure 14, separately at altitude ranges of 0–250, 250–500, and 500–750 km and for all altitudes. The dashed concentric circles represent magnetic latitude (MLAT) at 10° intervals from 55° to 85° , and the solid radial lines represent MLT at steps of 1 h local time (LT) from 06:00 to 18:00. The color plot also shows the mean $P_{th,\perp}$ for each position binned at $0.01 R_M \times 0.01 R_M$ with values represented by the color bar displayed. Just as Figure 13 showed that the latitudinal extent of observed filaments increases with altitude, with the third-dimension view shown in Figure 14, we also see distinct local-time dependence for the strength of the filaments. This dependence is not an aberration effect, since we have already corrected the filament positions with the aberration angle for each orbit. Figure 14a clearly shows that events with larger amplitude are mostly observed at the dawn side of the magnetosphere at altitudes below 250 km. We note, however, that there are few observations on the dusk side of the magnetosphere at these low altitudes. At higher altitudes (i.e., 250–500 km), the dependence of amplitude on amplitude is

still evident and remains a distinctive feature in Figure 14b, exhibited by the larger number of red points on the dawn side. At 500–750 km, the dependence of amplitude on local time is weaker. This pattern is partly the result of a lack of observations near the dawn side of the magnetopause at 500–750 km altitude. However, this result suggests that there might be a general relation between local time and $P_{th,\perp}$.

To further explore this idea, we plotted the normalized distribution of filament occurrences by MLT and $P_{th,\perp}$ in Figure 15. The distributions indicate that filaments have a high probability to occur near local noon and at $P_{th,\perp}$ values of $\sim 6\text{--}9$ nPa with significant occurrence rates at higher values of $P_{th,\perp}$. To remove orbital selection bias, we also took into consideration the total spacecraft dwell time for each 0.5 h bin in MLT. Figure 15c, which shows the distribution of total dwell time, indicates that MESSENGER did spend much of the time around local noon for our selected orbits. The quasi-Gaussian distribution is also consistent with our understanding of the elliptically shaped cusp and the expectation that the spacecraft spent less time in the cusp near dawn and dusk. Figure 15d shows the rate of occurrence by MLT normalized by dwell time of the spacecraft at that MLT (i.e., total time duration of filaments divided by the total dwell time for each MLT window), which indicates that there is an equal rate of occurrence (~ 0.08) of filaments between MLT 9.5 and 14.5 h. The lower and higher occurrence rates from 8.5 to 9.5 h MLT and 14.5 to 15.5 h MLT, respectively, are statistical effects from the normalization by dwell times less than 5 min. Hence, we do not consider these two MLT ranges further in our analysis. Figure 15e shows the dwell-time-normalized rate of occurrence by MLT for different

$P_{th,\perp}$ ranges. For filaments with $P_{th,\perp}$ between 6 and 12 nPa, the rate of occurrence fluctuates around 0.04, and there is no clear dependence of $P_{th,\perp}$ on MLT. However, there is a higher rate of occurrence for stronger filaments (i.e., 12–18 nPa) near dawn than dusk. This dawn-dusk asymmetry in filament occurrence is also observed for a $P_{th,\perp}$ range of 18–24 nPa (grey line) but is weaker as $P_{th,\perp}$ increases further. Future studies of the dependence of filament occurrence on MLT and $P_{th,\perp}$ should extend the range of local times and increase the number of filaments observed for each local time to reduce the statistical errors from limited sampling.

6. Discussion

MESSENGER observations of cusp filaments during 3 years of high-altitude and, later, 3 months of low-altitude observations were examined with minimum variance analysis and statistical methods. The analyses presented here strongly suggest that cusp filaments are diamagnetic in nature. Hot plasma ions with energies similar to those of magnetosheath ions [Gershman *et al.*, 2013] gyrate around the magnetic field lines to create a net diamagnetic current. This current then produces a magnetic field that opposes the background field, decreasing the total field magnitude, forming a diamagnetic filament. Statistical analysis at different altitudes shows that these ~2–3-s-long filamentary structures are highly localized with a mean size of 7–8 magnetosheath proton gyro-radii.

Our MVA results show that the high- and low-altitude filaments can be divided into four populations. The magnetic signatures and MVA results of Population I filaments are consistent with the basic picture of a quasi-cylindrical flux tube, i.e., a filament that is filled with hot ions having peak energy of ~ 1 keV. Population II filaments show the presence of “residual twist” to their magnetic structure. The implication of the “residual twist” structure for Population II filaments is discussed below. Population III filaments have MVA signatures similar to those of Population I filaments with a nearly constant magnetic field component in the intermediate direction, whereas Population IV filaments have MVA signatures that are poorly defined.

The total particle precipitation rate onto Mercury’s surface from cusp plasma filament may be determined from our analysis of low-altitude filaments. The distribution of MESSENGER’s dwell time with magnetic latitude and magnetic local time for the time period of this study is shown in Figure 16a. The figure shows that MESSENGER spent more time in the dawn-dusk sector than the noon sector during the orbits analyzed in this study. The spacecraft also spent ~ 10 h less time at higher latitudes than lower latitudes. The distribution of identified filaments is shown in the same projection in Figure 16b. The figure shows that majority of the filaments were observed near local noon and near $\sim 70^\circ$ in magnetic latitude. Another interesting feature of this figure is that filaments were seen at lower latitudes near local noon. This observation has implications for the formation and evolution of filaments, a point on which we elaborate below.

By extrapolating from the best-fit linear relation between $P_{\text{th},\perp}$ and altitude determined in Figure 12b and under the assumption $P_{\text{surface}} \sim P_{\text{th},\perp}$, we can estimate a lower limit on the proton precipitation flux onto Mercury's surface with each plasma filament:

$$\Phi = \frac{P_{\text{surface}}}{\sqrt{2\pi mk_B T}} \quad (5)$$

where k_B is the Boltzmann constant, and m and T are the mass and temperature of a proton, respectively [e.g., *Winslow et al.*, 2012]. The average number of ions $\langle N \rangle$ precipitating onto Mercury's surface for each pixel in Figure 16 is then given by the relation $\langle N \rangle = \langle \Phi \pi \left(\frac{d}{2}\right)^2 \rangle$ where d is the diameter of a cylindrical filament estimated earlier. Figure 16c shows the distribution of the mean particle precipitation rate $\langle N \rangle$. The figure shows that the region with the highest filament occurrence has an approximately uniform mean precipitation rate, and filaments with the highest precipitation rate occur at lower latitudes. This result suggests that magnetic field lines that map to lower latitudes were reconnected as magnetic reconnection (i.e., magnetic erosion) at the dayside magnetopause intensified and the cusp boundary “migrated” to lower latitudes as a result of magnetic flux transfer into the tail.

We can sum up the mean particle precipitation rate in each pixel and estimate the integrated particle precipitation rate to be $2.7 \times 10^{25} \text{ s}^{-1}$ with a standard mean error of $\pm 0.9 \times 10^{24} \text{ s}^{-1}$. This result is an order of magnitude larger than the rate of $(1.1 \pm 0.6) \times 10^{24} \text{ s}^{-1}$ derived in earlier studies of the average cusp [*Winslow et al.*, 2012; 2014; *Raines et al.*, 2014]. This difference suggests that the average particle precipitation rate in the cusp is an aggregate of the flux

delivered by individual filaments, and the filament events identified in this study contribute the most intense injections of magnetosheath plasma. This result is also consistent with findings at Earth, where the large-scale cusp is considered to be the aggregation of individual plasma injections from magnetic reconnection at the magnetopause [Burch *et al.*, 1982; Smith and Lockwood, 1990]. Interestingly, the individual cusp filaments at Mercury appear to be more easily identified than at Earth. This outcome is likely due to the high solar wind densities in the inner solar system and the weaker intrinsic magnetic field at Mercury.

Slavin et al. [2014] suggested that the formation of cusp filaments is related to the occurrence of FTEs at the dayside magnetopause. Our analysis results strongly suggest that the filaments observed in Mercury's cusp are indeed low-altitude extensions of the FTEs occurring at the dayside magnetopause. The simultaneous observation of FTEs and discrete series of cusp filaments at Mercury can also be explained with the "pulsating cusp" model first proposed by *Lockwood and Smith* [1990] for the terrestrial cusp. FTEs were first observed at Earth by *Russell and Elphic* [1978] and attributed to transient reconnection occurring on the dayside magnetopause. The prevailing theories for the formation of FTEs are based on the multiple X-line model [Lee and Fu, 1985] by which FTEs are formed by simultaneous reconnection at multiple locations or the sequential model [Raeder, 2006] with reconnection taking place at multiple X-lines but at different times on the dayside magnetopause. High rates of magnetic reconnection at Mercury's dayside magnetopause [*Slavin et al.*, 2009; *DiBraccio et al.*, 2013] result in the formation of FTEs in rapid succession, which has been observed at Mercury as

“FTE showers” [Slavin *et al.*, 2012]. Each FTE is a flux-rope-type structure with one end connected to the solar wind and the other to the planetary surface at the cusp. When the flux rope is first formed, the newly opened magnetic field lines will create a bulge equatorward of the polar cap boundary, separating the open and closed field lines, as has been proposed for Earth [Cowley, 1984; Southwood, 1987]. As more FTEs form at the magnetopause, the polar cap boundary also undergoes variations on the time scale of the FTE recurrence rate. More recently, cusp filaments have been documented in the polar cap boundary layer at the boundary between open and closed field lines [Gershman *et al.*, 2016]. Such a temporal variation in the terrestrial cusp formed the basis for the pulsating cusp model [Lockwood and Smith, 1990] in which the cusp is an aggregation of multiple FTE ionospheric footprints during bursts of reconnection at the dayside magnetopause.

Magnetosheath plasma, originally “tied” to the interplanetary magnetic field (IMF), becomes connected to the planetary field through the FTE. Force imbalance along the axis of the FTE and thermal gradients between the magnetosheath and planetary plasma will accelerate the plasma inside the FTE along the newly opened field lines into the cusp [Ma *et al.*, 1994]. At the same time, the flux tube convects poleward in order to release magnetic tension from the kink between the end of the flux tube connected to the IMF and the FTE. The observation of Population II filaments with “residual twist,” as evidenced by the MVA hodograms, and flux ropes with a core field quasi-parallel to the background field further support our idea that filaments are low-altitude extensions of FTEs. Moreover, the presence of Population III and IV filaments suggest

dynamic temporal and spatial variability in the evolution of these FTEs and plasma transport within each filament. This inference begs the question of why a large fraction of the filaments exhibit the magnetic structure of a quasi-cylindrical flux tube (i.e., Population I) whereas others exhibit weak helicity (Population II) or variability (Populations III and IV) in their magnetic structure. Are the different populations reflective of the temporal and spatial evolution of FTEs?

To understand the relation between FTEs and filaments, we compared our results with those of previous FTEs studies. *Slavin et al.* [2010] identified 6 FTEs with durations of ~1 to 6 s and axial magnetic fluxes of ~1–200 kWb during MESSENGER’s first two flybys of Mercury. *Imber et al.* [2014] identified 58 large-amplitude FTEs with a mean duration of ~2.48 s. Out of the 58 FTEs *Imber et al.* [2014] identified, a force-free model was fit to 17 FTEs and their mean axial magnetic flux was calculated to be ~60 kWb. For the frozen-in condition to hold, magnetic flux must be conserved. Our calculated mean magnetic flux of ~ 3 kWb is comparable to those of the smaller FTEs identified by *Slavin et al.* [2010], and the maximum magnetic flux of ~ 25 kWb is comparable to the mean flux of the FTEs identified by *Imber et al.* [2014]. Even though our statistical results are consistent with previous studies of FTEs, the histograms in Figure 12g and 12h show that ~78% of the filaments have magnetic flux less than 5 kWb, a figure that corresponds to the smaller (i.e., shorter duration) FTEs in the study by *Slavin et al.* [2010]. Hence, it is important to understand the limitations in our comparisons of magnetic flux.

To date, there has been no extensive study of the occurrence and evolution of FTEs at Mercury. Understanding the evolution of FTEs with respect to the filaments is essential to the

accurate comparison of magnetic flux and, most importantly, the connectivity between FTEs and filaments. Simulations and FTE studies at Earth [Ma *et al.*, 1994; Zhang *et al.*, 2010] have shown that as the plasma inside an FTE is transported into the cusp because of force imbalance along the FTE, the reduction in thermal pressure inside the FTE can cause an enhancement in the core field and a reduction in the size of the flux rope. Subsequently, the plasma transported into the filament will reduce the local magnetic field and lead to an expansion of the flux tube. Hence, observations of diamagnetic decreases in filaments serve as a tracer for plasma flow from the FTEs into the cusp in discrete flux tubes. However, this argument also implies that without understanding the temporal and spatial variation of plasma transport in FTEs, it is difficult to distinguish between the observed and actual size of the filament that maps to the size of the corresponding FTE. Therefore, our estimate of filament size and magnetic flux serve only as lower limits to the actual quantities. It is very difficult to establish a clear relationship between FTEs and filaments, given the limited information on mid- to high-latitude FTEs and time variability of FTE-filament interaction. Further study on the FTEs and their relation to cusp filaments at Mercury is warranted.

At Earth, the downward flow of magnetosheath plasma in FTEs, travelling into the polar cap, has been observed in situ as discrete injection of ions and electrons [Lockwood and Smith, 1989] and by ground-based observations as regions of high-density plasma “patches” in the F-layer [Lockwood and Carlson, 1992]. Most recently, Walsh *et al.* [2014] also showed simultaneous indirect ground-based and in situ space-based observations of FTEs at the magnetopause and

ionospheric injection of ions in the polar cap. The filaments observed at Mercury appear to be the same phenomenon as observed at Earth. Despite the lack of sufficient plasma data, MESSENGER was able to observe the magnetic effects of these high-density plasma injections into Mercury's cusp due to the formation of FTEs at the magnetopause. The similarity between Mercury's filaments and Earth's ionospheric FTE footprints raise the question of whether we could also observe localized decreases of magnetic field strength in the terrestrial cusp.

Our study of cusp filaments is not complete without understanding the solar wind conditions that drive their formation. Since our results strongly suggest that filaments are the low-altitude extensions of FTEs forming at the dayside magnetopause and the rate at which FTEs were formed is primarily driven by magnetic reconnection, we have looked for any correlation between the magnetosheath plasma β (the ratio of thermal pressure to magnetic pressure), the shear angle θ between magnetosheath and planetary magnetic field, and the occurrence of filaments. Figure 17 shows a plot of magnetosheath plasma β , calculated using the method of *DiBraccio et al.* [2013] under the assumption of pressure balance, and shear angle θ for the orbits of this study. The magnetosheath plasma β and shear angle θ for each orbit are calculated by averaging 10 s of magnetic field measurements immediately before and after the magnetopause crossing. The dashed gray line represents the condition for diamagnetic suppression of magnetic reconnection [*Swisdak et al.*, 2010] with $L = d_i$ given by the relation:

$$\Delta\beta > \frac{2L}{d_i} \tan\left(\frac{\theta}{2}\right) \quad (7)$$

where $\Delta\beta$ is the difference in plasma β across the magnetopause. Under the assumption that β inside the magnetosphere is negligible, $\Delta\beta \approx \beta_{\text{MSH}}$, where β_{MSH} is the plasma β in the magnetosheath. The curve for diamagnetic suppression of reconnection separates Figure 17 into two regions; the regions to the right and left of the curve suppress and favor magnetic reconnection at the magnetopause, respectively. Figure 17 shows that $\sim 85\%$ of the orbits with cusp filaments lie to the left of the *Swisdak et al.* [2010] relation, indicating that most of the filaments occur under conditions when magnetic reconnection is favored. This high fraction supports a causal relationship between magnetic reconnection and the occurrence of filaments. Moreover, Figure 17 shows that cusp filaments appear to form preferentially under low β , i.e., $\beta < 1$, and high shear angle. This result agrees with experience at Earth, where magnetic reconnection is more likely to occur under high shear and low- β conditions [*Paschmann et al.*, 1986; *Trenchi et al.*, 2008; *Phan et al.*, 2010]. On the other hand, there are also a number of orbits in our study with low θ , and on some of those orbits high numbers of filaments were observed, but only for $\beta < 0.1-1$. This finding is in agreement with the studies by *DiBraccio et al.* [2013] and *Slavin et al.* [2014], which concluded that the reconnection rate at Mercury's magnetopause is independent of the shear angle at low β . Therefore, the results in Figure 17 suggest that the strong dependence of filament occurrence on solar wind parameters is similar to those governing magnetic reconnection at the magnetopause and, therefore, further strengthen the concept that filaments are the high-latitude extensions of FTEs.

7. Conclusions

This study has shown that the brief, ~ 2 – 3 -s-long, deep ($\langle \frac{\delta B}{B} \rangle \sim 22\%$) decreases in magnetic field intensity observed in and around Mercury's magnetospheric cusp by MESSENGER are diamagnetic in nature and most likely due to plasma being injected down the flux tubes at the magnetopause by localized reconnection. We have employed a scale-free algorithm to identify the filaments. MVA results have shown that the majority of the filaments are quasi-cylindrical or slightly flattened cylindrical magnetic flux tubes aligned with the ambient dayside magnetic field. The FIPS plasma measurements indicate that the plasma in the filaments has energy levels similar to those of magnetosheath plasma.

Analysis of measurements from MESSENGER's low-altitude campaign indicates that these filaments extend down to very low altitudes, < 50 km, and probably are observable on the surface. This result strongly suggests that most of the plasma in each filament eventually precipitates onto Mercury's surface in the vicinity of the cusp by the time the flux tubes are swept into the magnetotail. The same impulsive reconnection at the magnetopause that produces FTEs increases the velocity parallel to the magnetic field and injects plasma down the flux tubes and into the cusp. As the magnetic field magnitude increases with decreasing altitude, the particles gain more perpendicular energy and produce the diamagnetism we observed in these filaments. Observations of filaments with "residual twist" similar to the helical structure of

magnetic flux ropes, but without the core field, support our hypothesis that cusp filaments map to FTEs at the magnetopause.

We estimated the occurrence-rate-normalized integrated particle precipitation rate from the filaments to be $\sim (2.70 \pm 0.09) \times 10^{25} \text{ s}^{-1}$. This rate is larger than estimates determined in previous studies of the average cusp magnetic field depression [Winslow *et al.*, 2012, 2014]. This result has important implications for surface sputtering and space weathering in the cusp region at Mercury [Kallen and Ip, 1999; Domingue *et al.*, 2014]. Our estimation provides an upper limit on flux precipitation by cusp filaments at Mercury. During extreme solar wind conditions, the total flux of precipitating particle contributed by the filaments could be the dominant source of energetic particles for sputtering neutral atoms off the surface [Sarantos *et al.*, 2001; Massetti *et al.*, 2007; Mangano *et al.*, 2015] and related space weathering effects [Domingue *et al.*, 2014]. Future work should investigate the plasma properties of these filaments with the help of simulations to reconstruct their internal structure. Such studies would further our understanding of the microphysics surrounding magnetopause reconnection, FTE formation, and the injection of plasma into the cusp at Mercury and other planets.

Acknowledgments

Conversations with J. C. Kasper on the identification method used here are appreciated. We also thank two anonymous reviewers for constructive comments on an earlier draft. The MESSENGER project is supported by the NASA Discovery Program under contracts NASW-

00002 to the Carnegie Institution of Washington and NAS5-97271 to The Johns Hopkins University Applied Physics Laboratory. All data analyzed in this paper are archived with the NASA Planetary Data System. Further support was provided by NASA Discovery Data Analysis Program grants NNX15K88G and NNX15AL01G, Living With a Star program grant NNX16AJ67G and Solar System Workings Program grant NNX15AH28G to the University of Michigan.

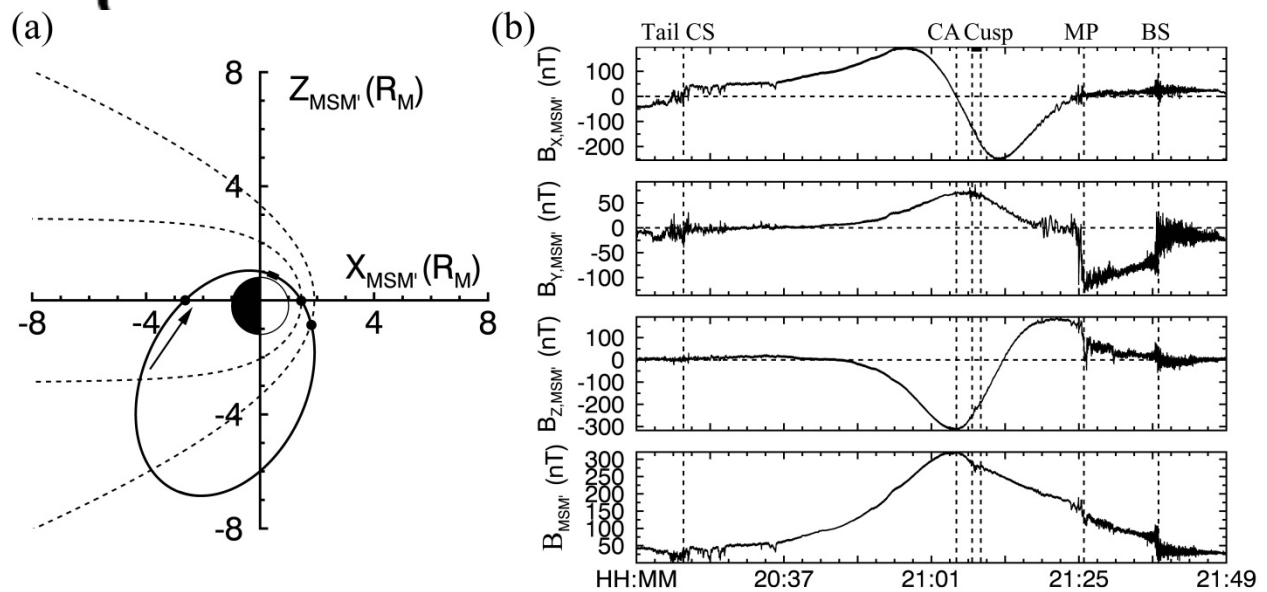


Figure 1. (a) An example MESSENGER orbit (black solid line) on 26 August 2011 projected onto the X - Z plane in aberrated Mercury solar magnetic (MSM') coordinates during a period without filamentary activities in the cusp. The aberration angle is -7.31° . The model bow shock (BS) and magnetopause (MP) from *Winslow et al.* [2013], scaled to fit observed boundary crossings (marked by the two dots at the dayside magnetosphere), are shown in dotted lines; the Sun is to the right. The thick portion of the orbit represents the cusp region, and the dot at the nightside magnetosphere represents the magnetotail current sheet (CS) crossing. The arrow denotes the spacecraft trajectory. (b) Full-resolution magnetic field measurements (top to bottom, X , Y , and Z components and field magnitude) acquired along the orbit shown in (a). The vertical dashed lines mark the boundary crossings shown in (a). CA denotes closest approach, and all times are in UTC.

Author Manuscript

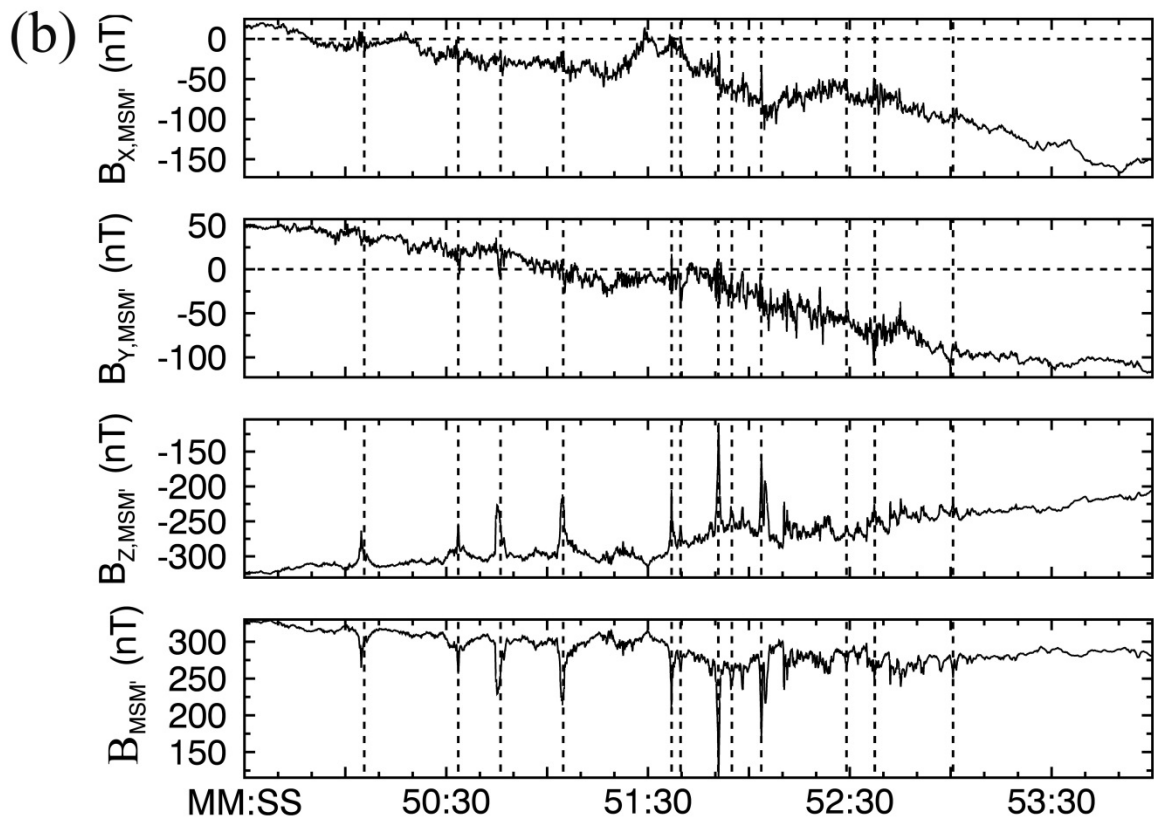
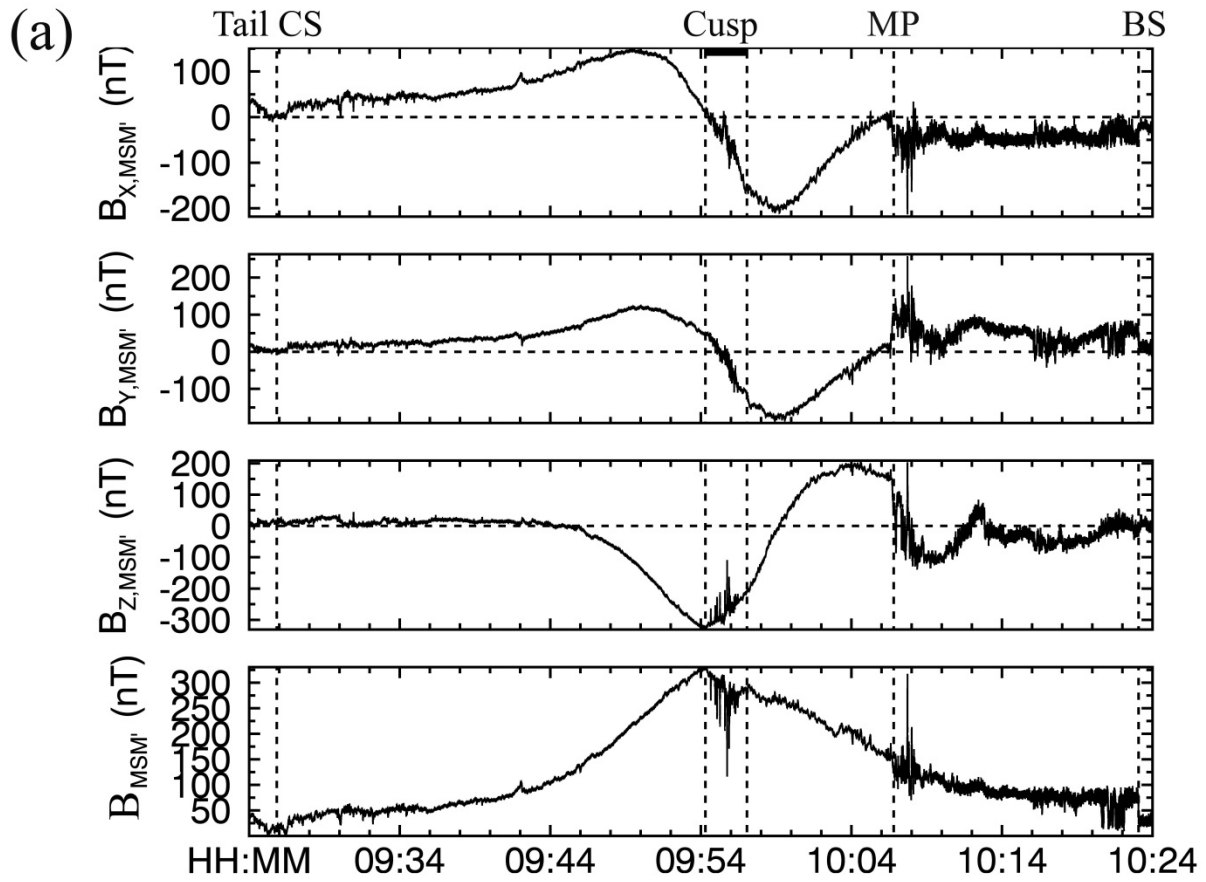


Figure 2. (a) Magnetic field measurements during an example orbit on 20 May 2011 during which plasma filaments were observed in the cusp. Magnetic field components are in aberrated MSM' coordinates for an aberration angle of -6.31° . The format is similar to that of Figure 1b. (b) Close-up of magnetic field measurements in the cusp region for the time interval delimited by the dashed lines in (a) labeled cusp. Each cusp filament identified by the automated algorithm is denoted by a vertical dashed line.

Author Manuscript

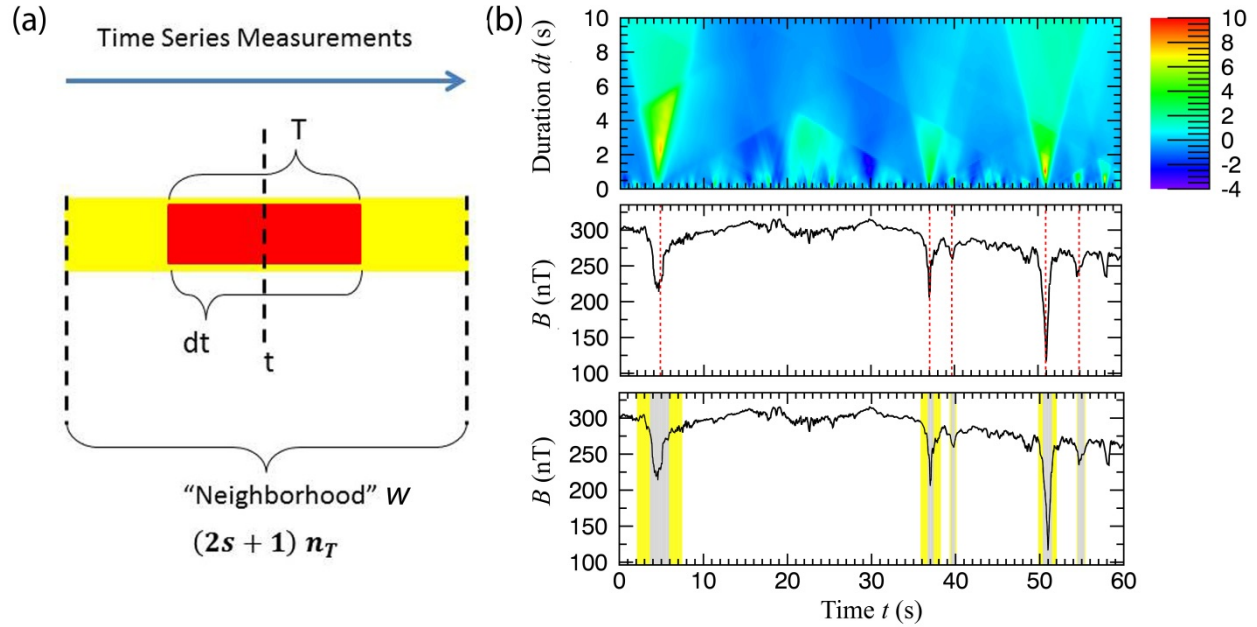
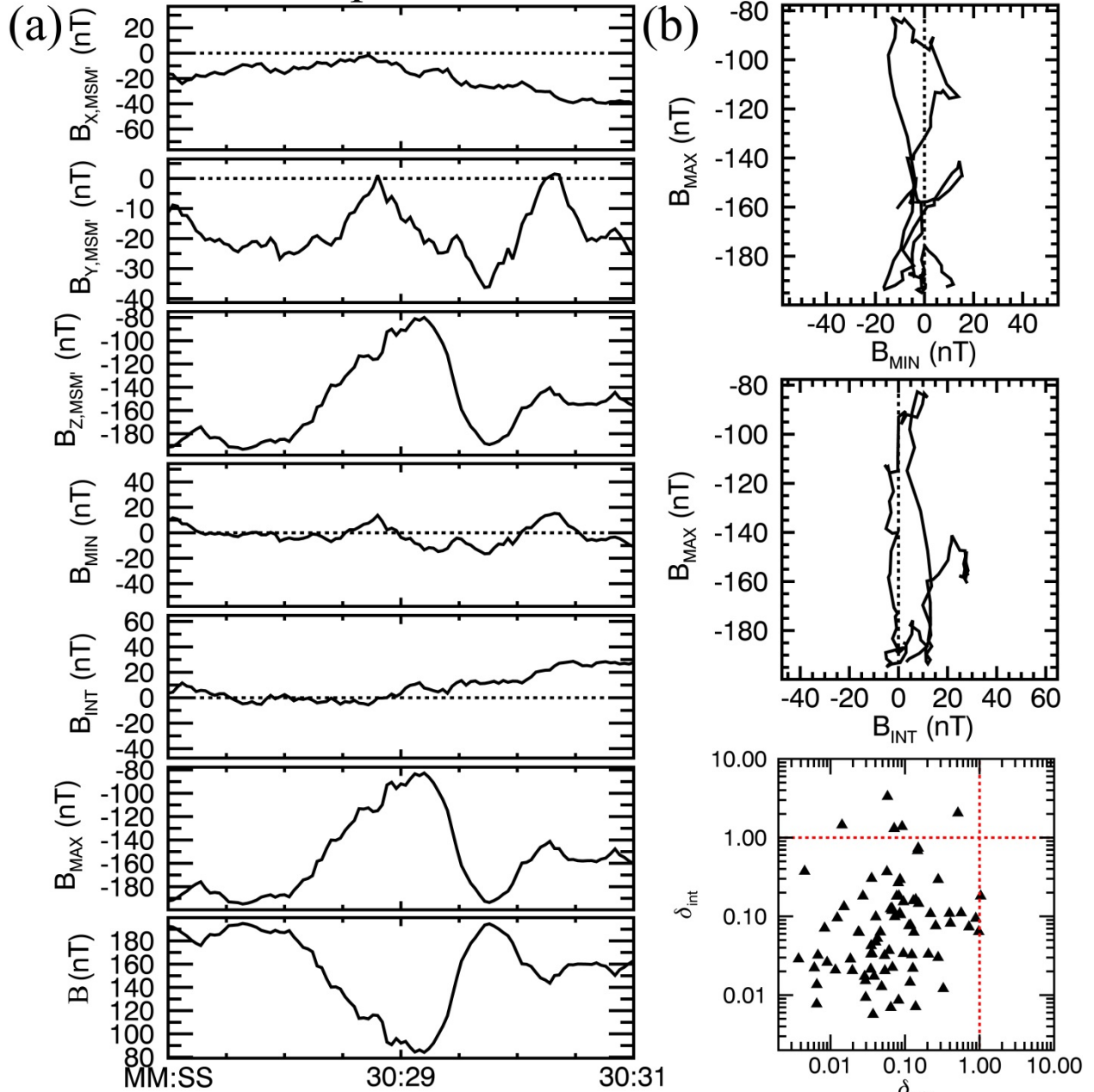


Figure 5. (a) Schematic illustration of the different time segments used in the quasi-automatic, scale-free identification algorithm. The red and yellow boxes represent a time segment T and “neighborhood” W , respectively; both are centered at time t . (b) Top: map of q values (color bar) for a 1-min interval at 09:51 UTC on 20 May 2011 for optimum values of $q_0 = 3.9$ and $s = 3$; the ordinate is duration dt , and the abscissa is time t within that interval. Middle: B for the same time interval; vertical red dashed lines indicate the times of filaments identified by the automated method. Bottom: B for the same time interval with gray shaded areas representing dt_{\max} values that correspond to q_{\max} and yellow shaded areas spanning dt values that correspond to half maximum values of q_{\max} at times t_{\max} .

23 April 2013 16:30:29 UTC

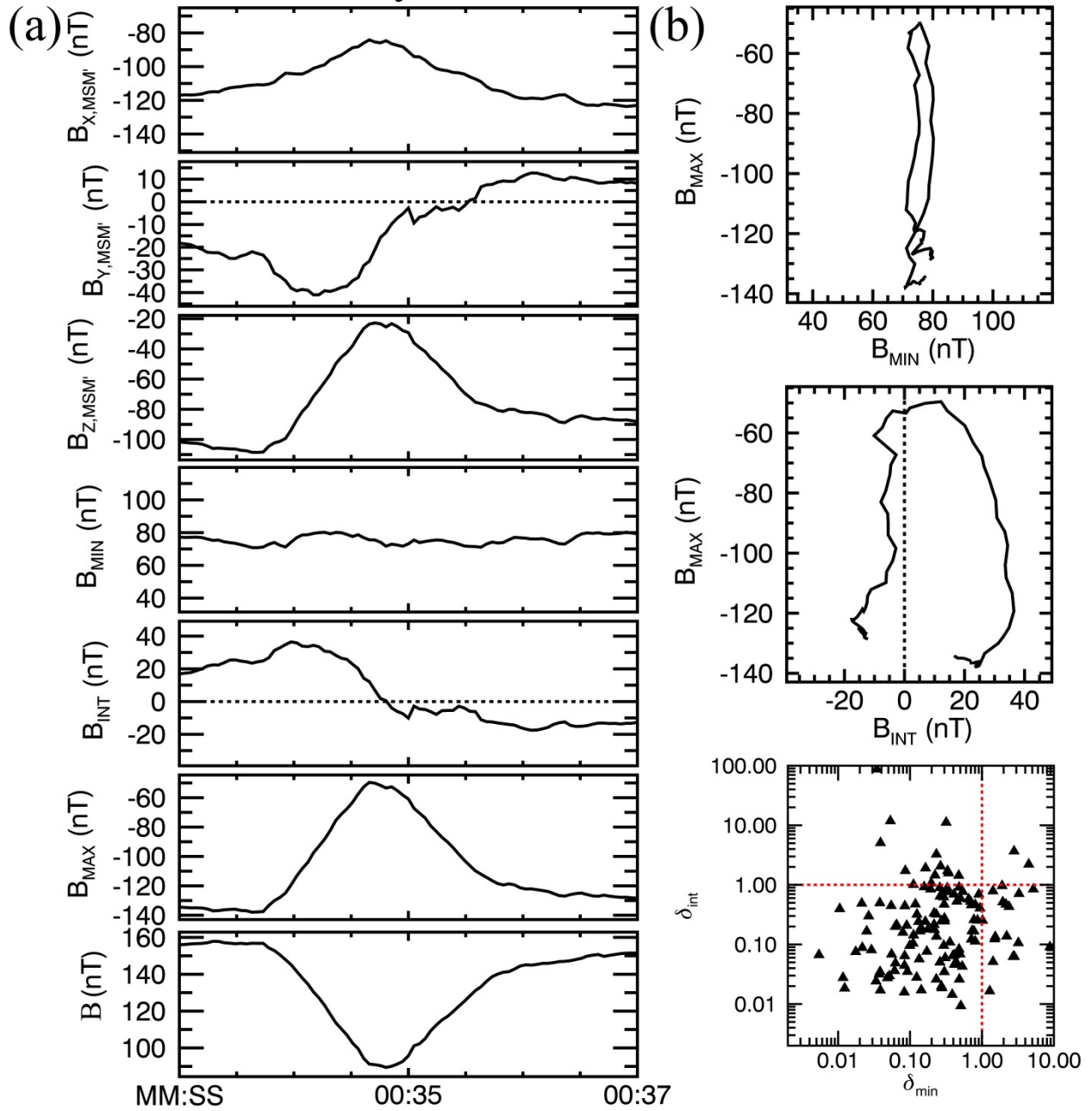


AU

Figure 4. Magnetic field variations during a Population I cusp plasma filament observed on 23 April 2013 at approximately 16:30:29 UTC. (a) Panels 1–3 (top to bottom) show the full-resolution magnetic field measurements in aberrated MSM' coordinates, panels 4–6 show the magnetic field measurements in MVA coordinates, and panel 7 shows the total magnetic field. (b) The top and middle panels show the MVA hodograms for the filament in Figure 4a. The bottom panel shows δ_{\min} versus δ_{int} for all Population I filaments identified in this study. The red lines represent the $\delta_i = 1$ condition.

Author Manuscript

26 July 2013 17:00:36 UTC

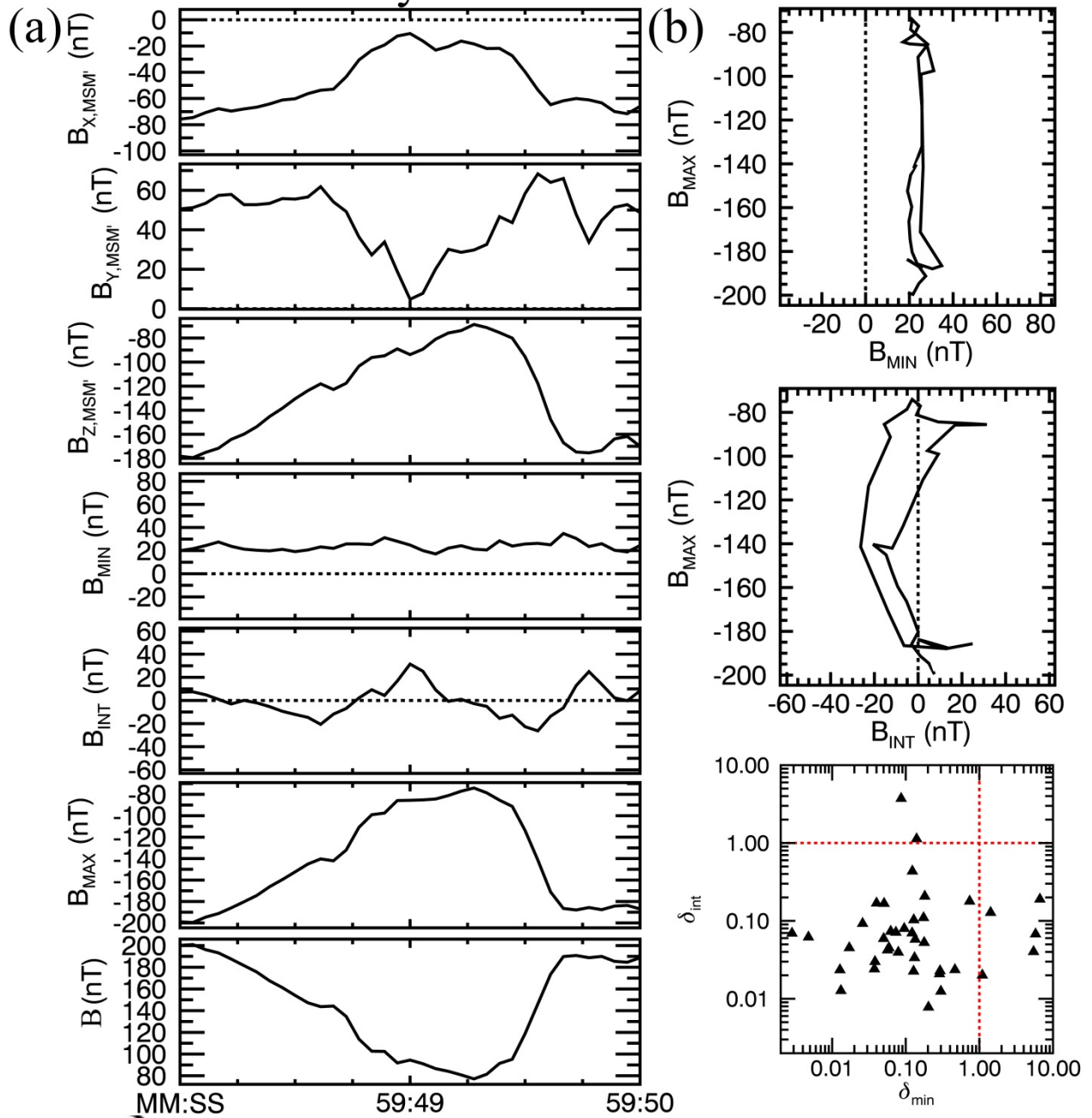


AL

Figure 5. Magnetic field variations during a Population II cusp filament observed on 26 July 2013 at approximately 17:00:36 UTC. (a) Magnetic field measurements in aberrated MSM' and MVA coordinates; the format follows that of Figure 4a. (b) MVA hodograms for the same time interval as in (a) and a plot of δ_{\min} versus δ_{int} for all Population II events.

Author Manuscript

27 July 2013 08:59:49 UTC

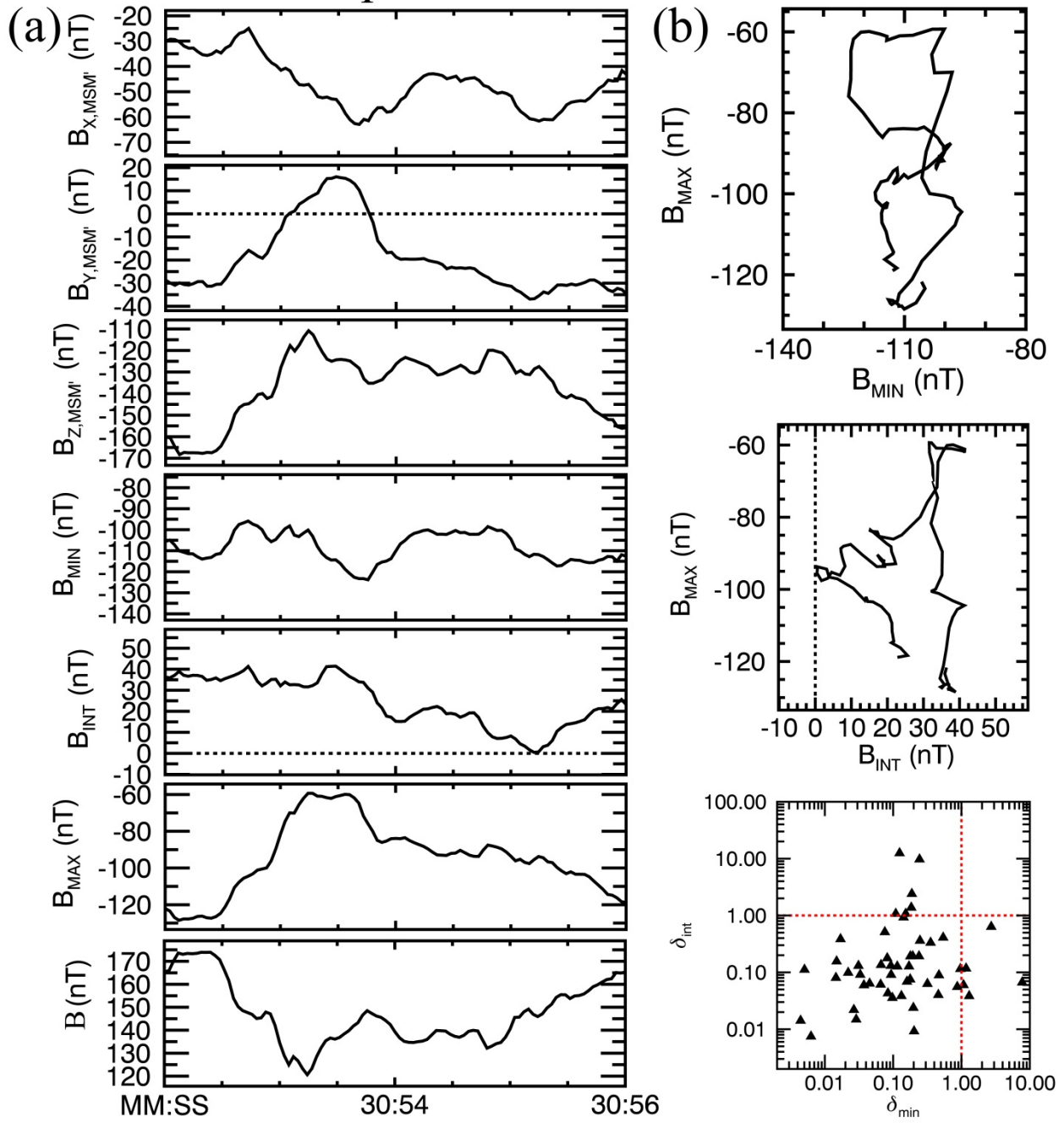


AL

Figure 6. Magnetic field variations during a Population III cusp plasma filament observed on 27 July 2013 at approximately 08:59:49 UTC (a) Magnetic field measurements in aberrated MSM' and MVA coordinates; the format follows that of Figure 4a. (b) MVA hodograms for the same interval as in (a) and a plot of δ_{\min} versus δ_{int} for all Population III events.

Author Manuscript

23 April 2013 16:30:54 UTC



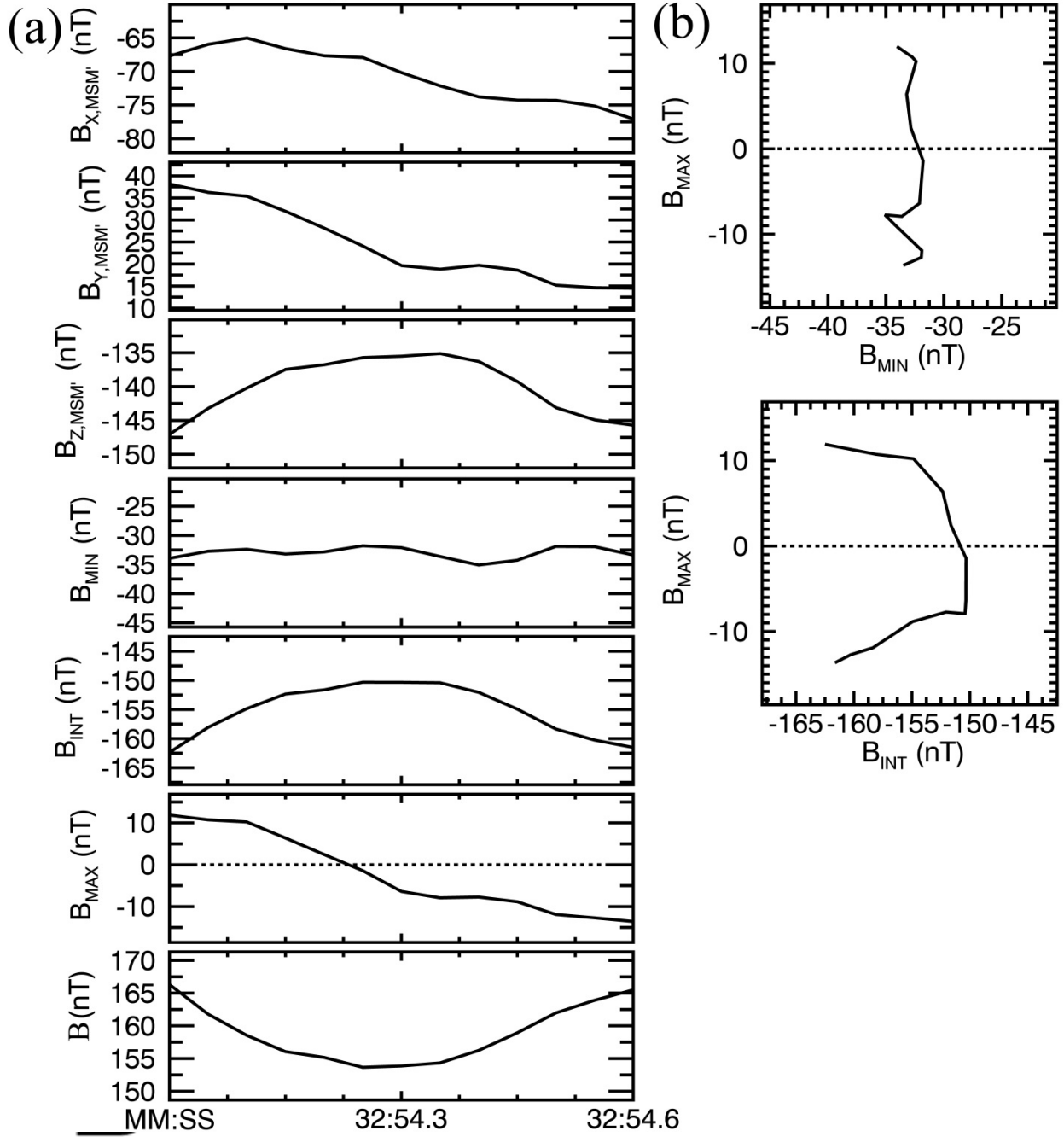
A

Figure 7. Magnetic field variations during a Population IV cusp plasma filament observed on 23 April 2013 at approximately 16:30:54 UTC. (a) Magnetic field measurements in aberrated MSM' and MVA coordinates; the format follows that of Figure 4a. (b) MVA hodograms for the same interval as in (a) and a plot of δ_{\min} versus δ_{int} for all Population IV events.

Author Manuscript

Author Manuscript

27 April 2013 16:32:54 UTC



A

Figure 8. Magnetic field variations during a flux rope observed on 27 April 2013 at approximately 16:32:54 UTC. (a) Magnetic field measurements in aberrated MSM' and MVA coordinates; the format follows that of Figure 4a. (b) MVA hodograms for the same interval as in (a).

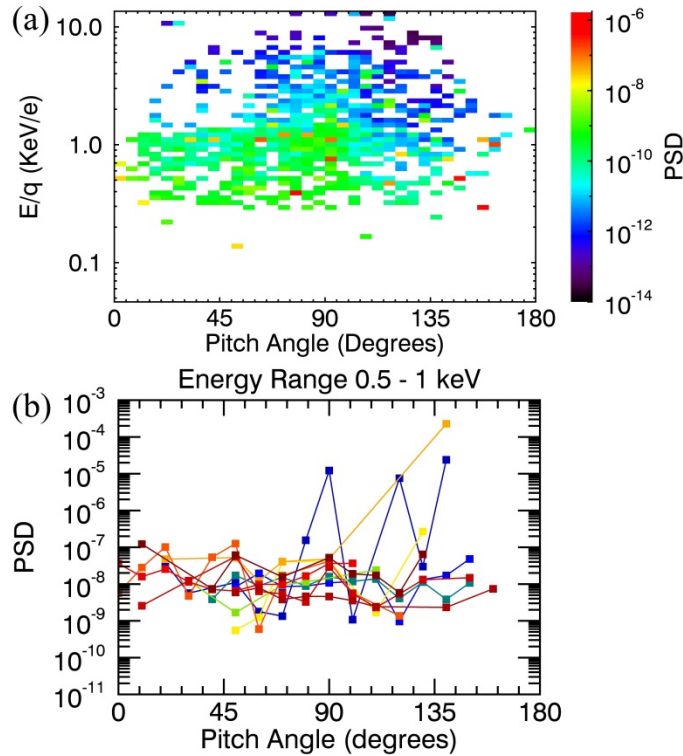


Figure 9. (a) Energy-resolved pitch angle distribution of 16 filaments. The filaments were selected to ensure coverage of the entire FIPS energy range and look angle. Each pixel represents a pitch angle bin size of 5° ; phase space density (PSD) is represented by color. (b) Plot of PSD versus pitch angle for 11 filaments observed in the energy range 0.5–1 keV. Each filament event is represented by a different color.

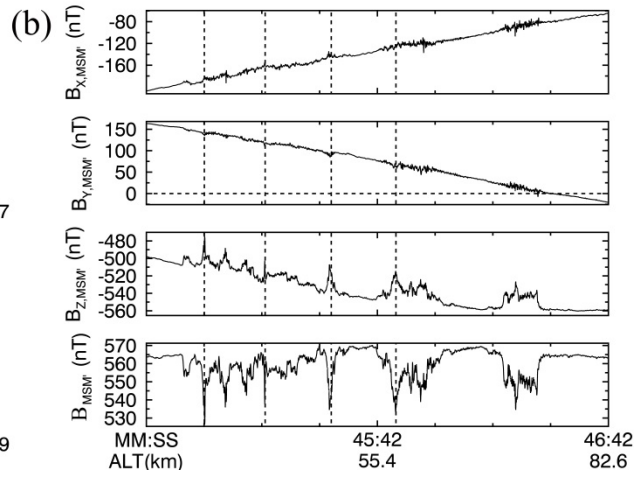
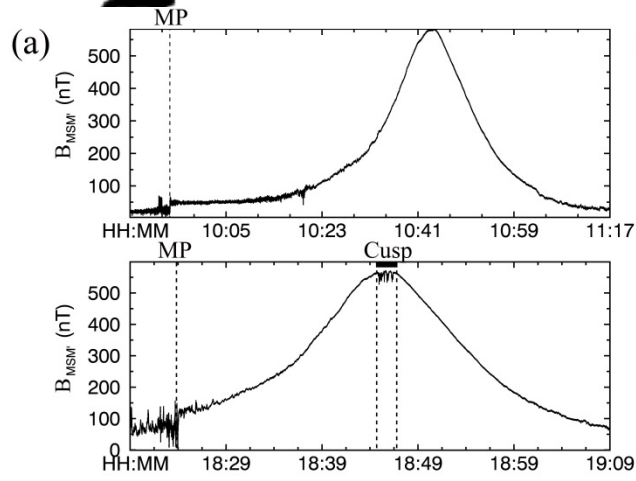


Figure 10. (a) Magnetic field measurements in aberrated MSM' coordinates during two successive orbits on 31 August 2014. (Top) A cusp crossing with no filaments detected. The aberration angle is -5.79° , and the vertical dashed line represents the magnetopause crossing. (Bottom) A cusp crossing 8 h later during which filaments were detected. Two vertical dashed lines delimit the cusp region. (b) Close up of magnetic field measurements within the cusp for the orbit in the bottom panel of (a). Each cusp filament identified by the automated algorithm is marked by a vertical dashed line.

Author Manuscript

15 August 2014 17:05:18 UTC

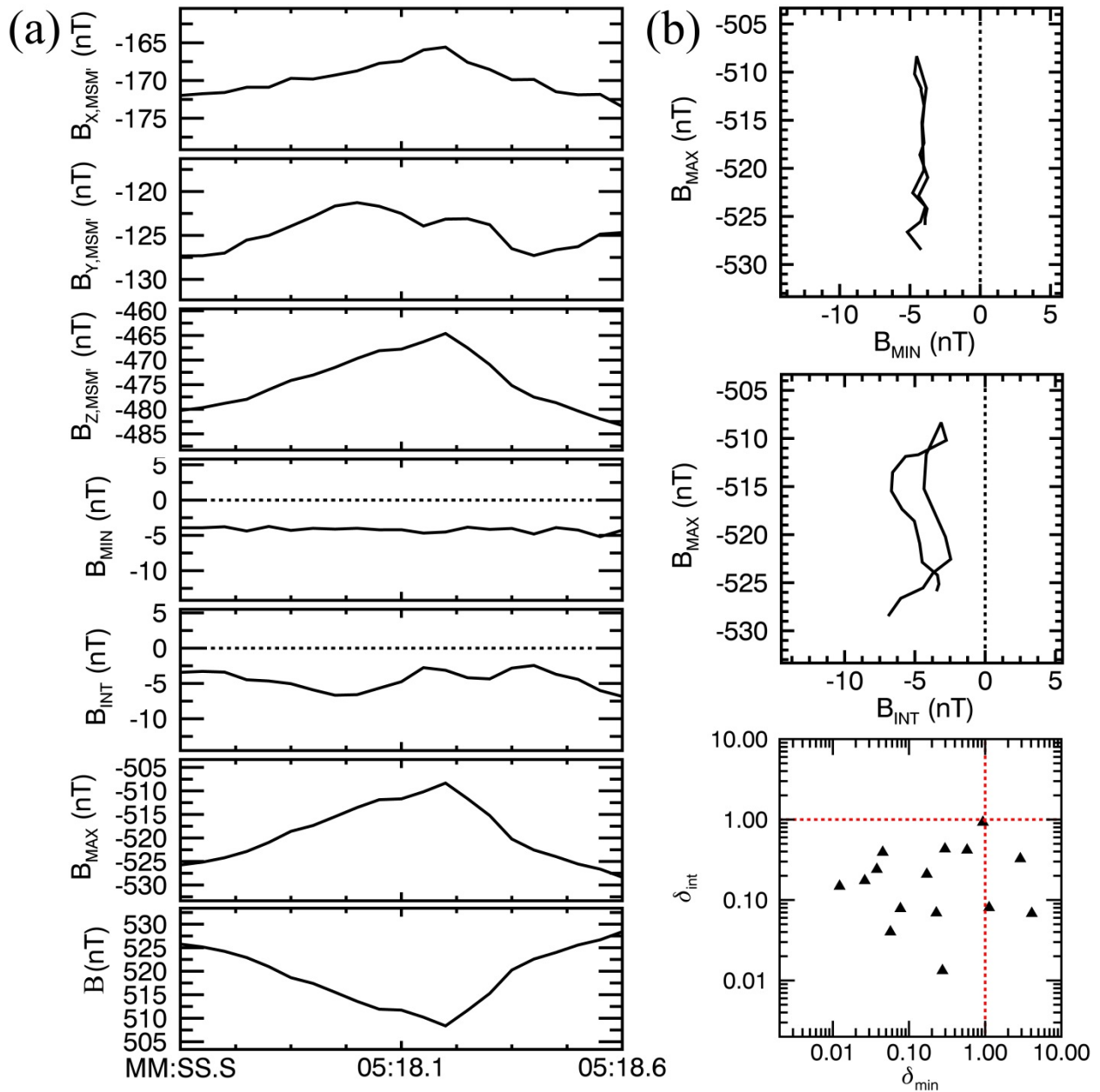
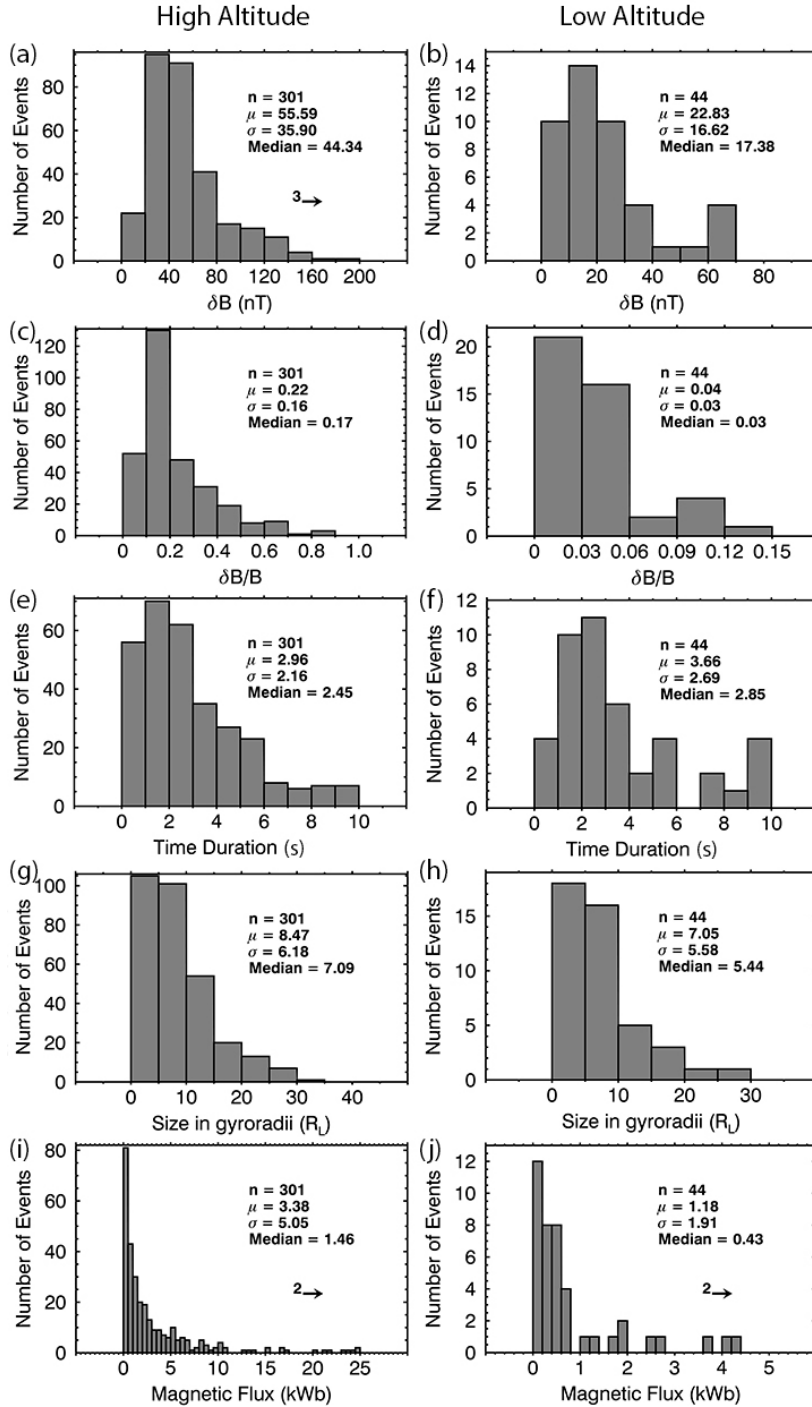


Figure 11. Magnetic field variations during a low-altitude Population III cusp plasma filament observed on 15 August 2014 at approximately 17:05:18 UTC. (a) Magnetic field measurements

in aberrated MSM' and MVA coordinates; the format follows that of Figure 4a. (b) MVA hodograms for the same interval as in (a) and a plot of δ_{\min} versus δ_{int} for all low-altitude Population III events.

Author Manuscript



A

Figure 12. Histograms of the filament parameters (a,b) δB , (c,d) $\delta B/B$, (e,f) time duration, (g,h) size in proton gyroradii r_L , and (i,j) magnetic flux. Left and right columns show results for high- and low-altitude filaments, respectively.

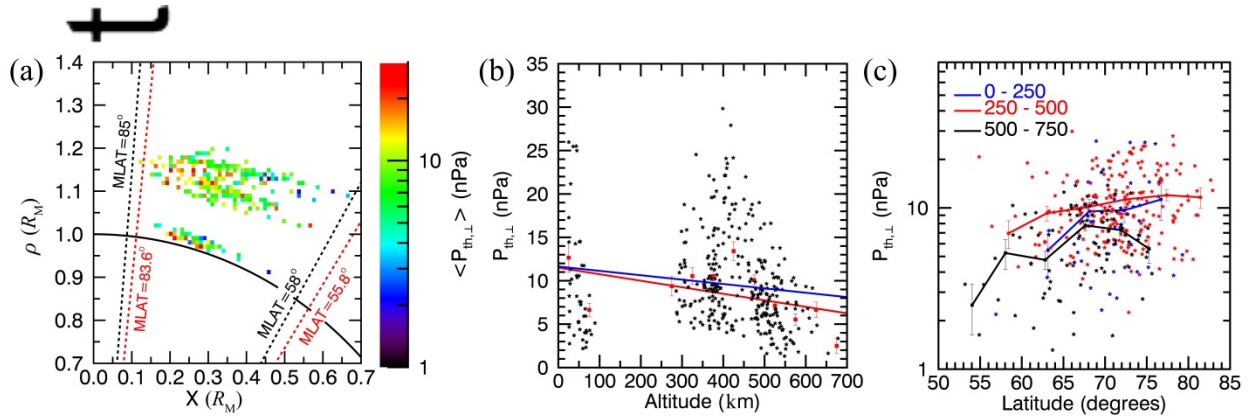


Figure 13. (a) Locations of cusp plasma filaments identified in this study, binned in $0.01-R_M$ -wide bins in the cylindrical coordinates ρ and X and color coded by perpendicular thermal pressure $P_{th,\perp}$. The black and red dashed lines show the extent in magnetic latitude (MLAT) of filament observations and the mean cusp boundaries of Winslow et al. [2012], respectively. (b) Plot of perpendicular thermal pressure versus altitude. Red squares represent mean values of $P_{th,\perp}$ averaged in 50-km-wide altitude bins, and the error bars show the standard errors for each “binned” value of $P_{th,\perp}$. The blue and red lines represent linear fits to the “un-binned” and “binned” data, respectively. The corresponding correlation coefficient (r) is -0.14 and -0.55, respectively. (c) Plot of perpendicular thermal pressure versus magnetic latitude at three different ranges of altitude, 0–250 (blue), 250–500 (red), and 500–750 (black) km. Each square

represents mean $P_{\text{th},\perp}$ values averaged over 5° -wide latitude bins, and the error bars show the standard errors.

Author Manuscript

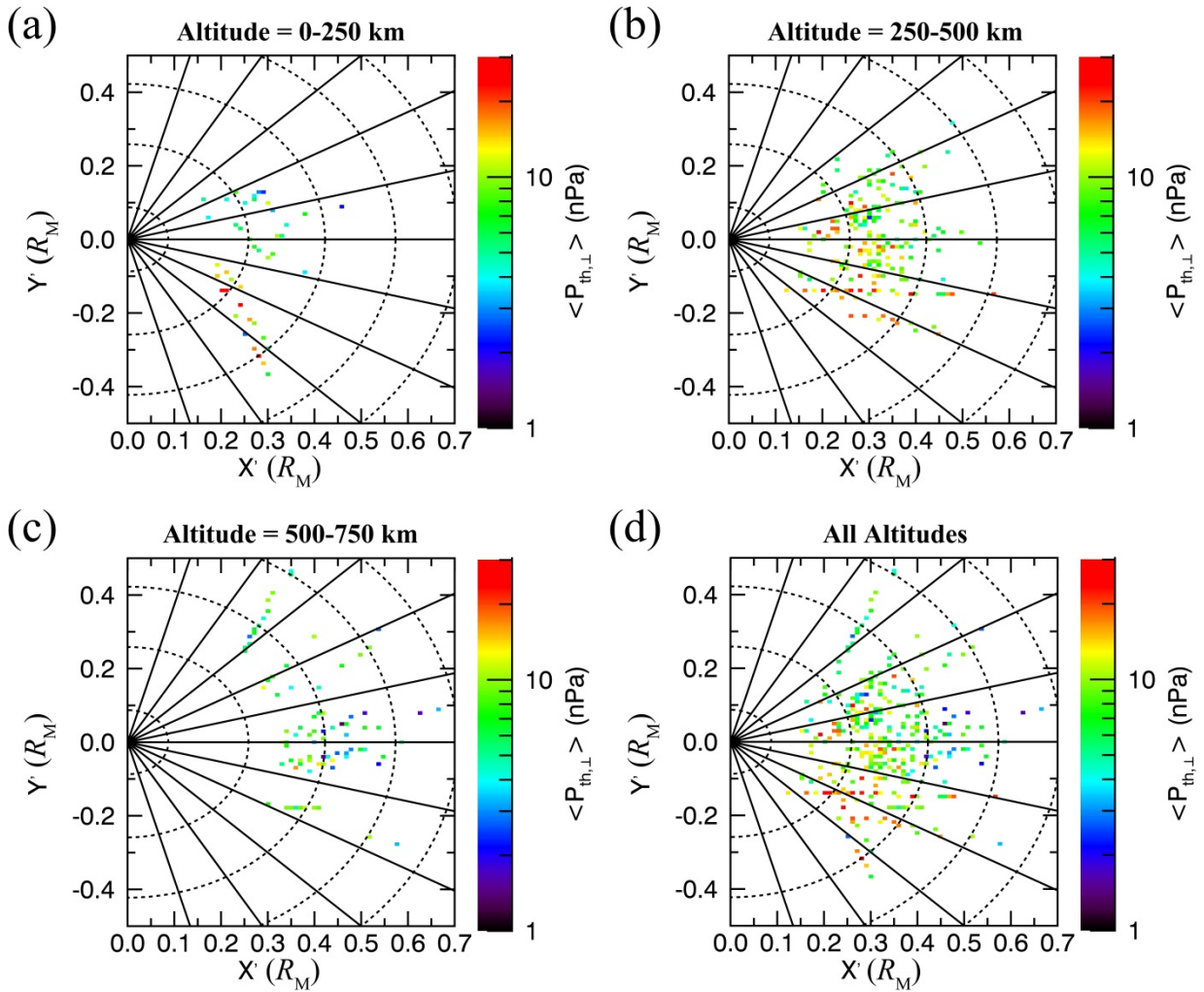


Figure 14. (a-c) Binned plot of $P_{th,\perp}$ in the aberrated X' - Y' plane for different altitudes ranges: (a) 0–250 km altitude; (b) 250–500 km altitude; (c) 500–750 km altitude; (d) all altitudes. Colors denotes mean $P_{th,\perp}$ values in $0.01 R_M \times 0.01 R_M$ bins. Dashed concentric circles depict magnetic latitude from 45° to 85° N at 10° intervals. Radial solid lines depict magnetic local time at 1 h intervals.

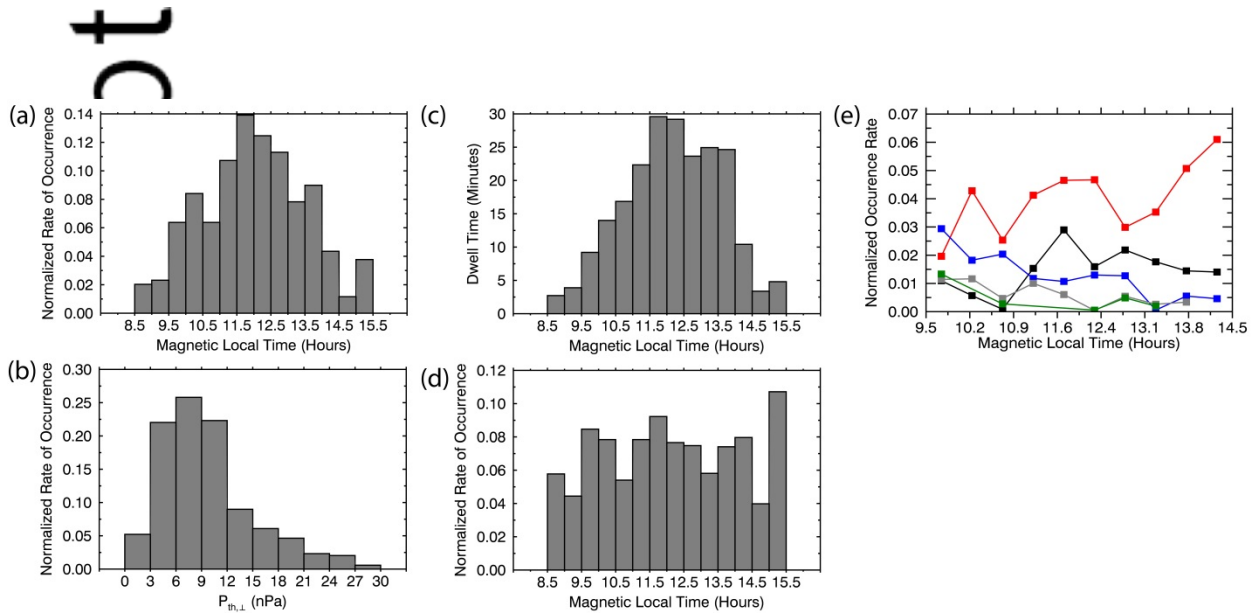


Figure 15. (a) Normalized rate of occurrence of filaments as a function of magnetic local time and (b) perpendicular thermal pressure $P_{th,\perp}$. (c) Histogram of MESSENGER dwell time as a function of magnetic local time. (d) Dwell-time-normalized rate of occurrence of filaments as a function of magnetic local time and (e) as a function of magnetic local time at different $P_{th,\perp}$ ranges. The $P_{th,\perp}$ ranges are 0–6 nPa (black), 6–12 nPa (red), 12–18 nPa (blue), 18–24 nPa (grey), and 24–30 nPa (green).

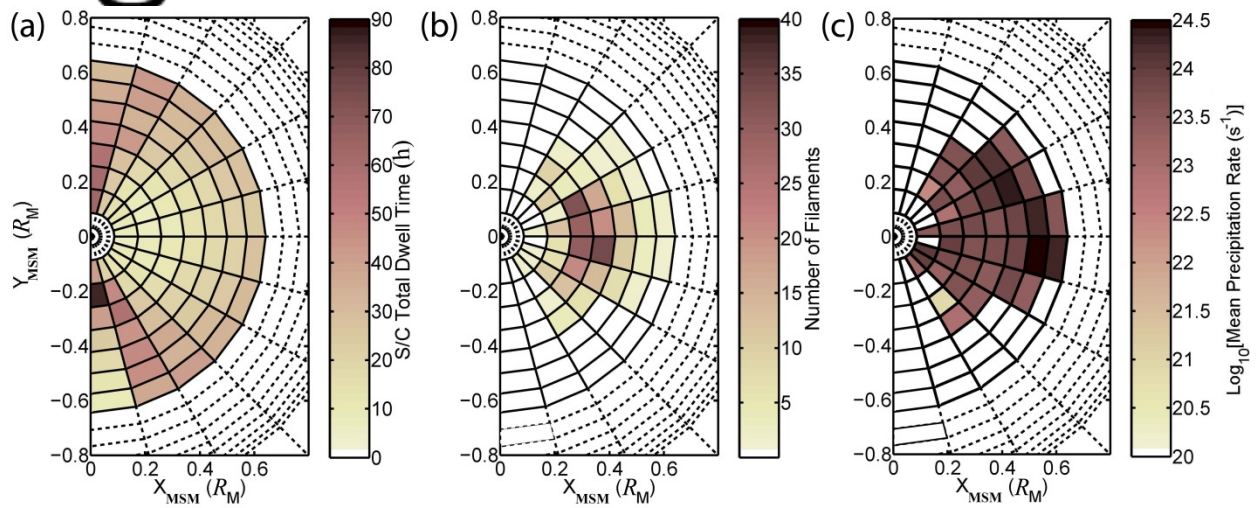


Figure 16. (a) Distribution of total MESSANGER dwell time for the time period of this study. Each pixel spans 5° in MLAT, from 50° to 85°N , and 1 h in MLT, from 6 h to 18 h, with values represented by the color bar displayed. (b) Distribution of number of filaments in the same format. (c) Distribution of mean particle precipitation rate in the same format (\log_{10} scale).

Author Manuscript

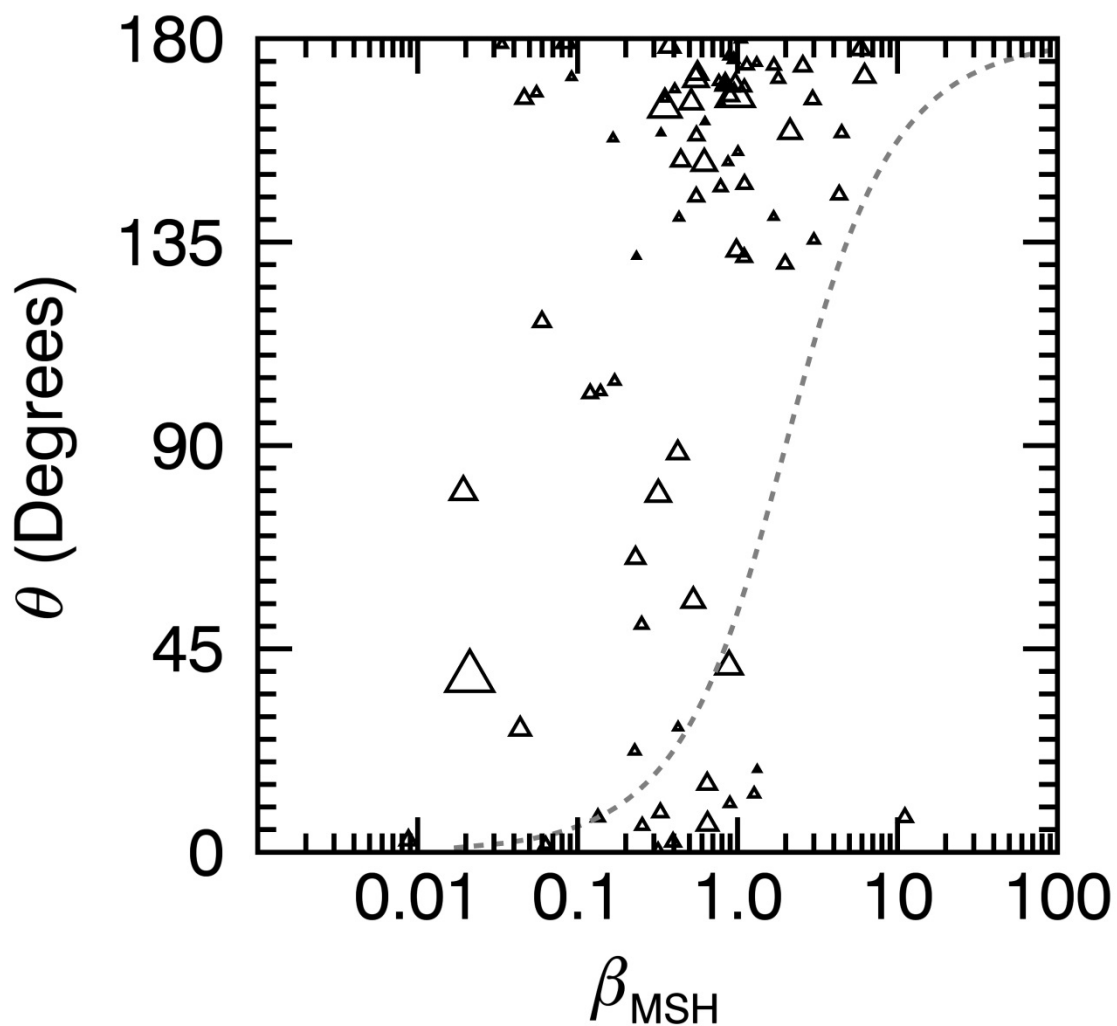


Figure 17. Magnetosheath plasma β_{MSH} versus IMF shear angle θ for the orbits of this study. The size of each symbol is proportional to the number of filaments identified on that orbit. β_{MSH} is computed under the assumption of pressure balance between the solar wind and the planetary

Auti

magnetic field at the magnetopause, given that plasma pressure in the magnetosphere is approximately zero. θ is defined as the angle between the IMF and planetary field inside the dayside magnetosphere. The components and magnitude of the magnetic field in the solar wind and Mercury's magnetosphere are obtained by averaging 10 s of magnetic field measurements immediately inbound and outbound of the magnetopause crossing. The dashed gray line shows the *Swisdak et al.* [2010] condition for diamagnetic suppression of magnetic reconnection at the dayside magnetopause $\Delta\beta > \frac{2L}{d_i} \tan\left(\frac{\theta}{2}\right)$ with $L = d_i$.

Author Manuscript

References

- Alexeev, I. I., et al. (2010), Mercury's magnetospheric magnetic field after the first two MESSENGER flybys, *Icarus*, *209*, 23–39, doi:10.1016/j.icarus.2010.01.024.
- Anderson, B. J., M. H. Acuña, D. A. Lohr, J. Scheifele, A. Raval, H. Korth, and J. A. Slavin (2007), The Magnetometer instrument on MESSENGER, *Space Sci. Rev.*, *131*, 417–450, doi:10.1007/s11214-007-9246-7.
- Anderson, B. J., J. A. Slavin, H. Korth, S. A. Boardsen, T. H. Zurbuchen, J. M. Raines, G. Gloeckler, R. L. McNutt Jr., and S. C. Solomon (2011), The dayside magnetospheric boundary layer at Mercury, *Planet. Space Sci.*, *59*, 2037–2050.
- Anderson, B. J., C. L. Johnson, H. Korth, J. A. Slavin, R. M. Winslow, R. J. Phillips, R. L. McNutt Jr., and S. C. Solomon (2014), Steady-state field-aligned currents at Mercury, *Geophys. Res. Lett.*, *41*, 7444–7452, doi:10.1002/2014GL061677.
- Andrews, G. B., et al. (2007), The Energetic Particle and Plasma Spectrometer instrument on the MESSENGER spacecraft, *Space Sci. Rev.*, *131*, 523–556, doi:10.1007/s11214-007-9272-5.
- Balikhin, M. A., R. Z. Sagdeev, S. N. Walker, O. A. Pokhotelov, D. G. Sibeck, N. Beloff, and G. Dudnikova (2009), THEMIS observations of mirror structures: Magnetic holes and instability threshold, *Geophys. Res. Lett.*, *36*, L03105, doi:10.1029/2008GL036923.
- Baumjirtel, K., K. Sauer, and E. Dubinin (2003), Towards understanding magnetic holes: Hybrid simulations, *Geophys. Res. Lett.*, *30*(14), 1761, doi:10.1029/2003GL017373.
- Boardsen, S. A., B. J. Anderson, M. H. Acuña, J. A. Slavin, H. Korth, and S. C. Solomon (2009), Narrow-band ultra-low-frequency wave observations by MESSENGER during its January

2008 flyby through Mercury's magnetosphere, *Geophys. Res. Lett.*, *36*, L01104, doi:10.1029/2008GL036034.

Burch, J. L., P. H. Reiff, R. A. Heelis, J. D. Winningham, W. B. Hanson, C. Gurgiolo, J. D. Menietti, R. A. Hoffman, and J. N. Barfield (1982), Plasma injection and transport in the midlatitude polar cusp, *Geophys. Res. Lett.*, *9*, 921–924.

Cowley, S. W. H. (1984), Solar wind control of magnetospheric convection, in *Achievements of the International Magnetospheric Study, (IMS), Spec. Pub. 217*, pp. 483–494, European Space Agency, Noordwijk, The Netherlands.

DiBraccio, G. A., J. A. Slavin, S. A. Boardsen, B. J. Anderson, H. Korth, T. H. Zurbuchen, J. M. Raines, D. N. Baker, R. L. McNutt Jr., and S. C. Solomon (2013), MESSENGER observations of magnetopause structure and dynamics at Mercury, *J. Geophys. Res. Space Physics*, *118*, 997–1008, doi:10.1002/jgra.50123.

DiBraccio, G. A., J. A. Slavin, J. M. Raines, D. J. Gershman, P. J. Tracy, S. A. Boardsen, T. H. Zurbuchen, B. J. Anderson, H. Korth, R. L. McNutt Jr., and S. C. Solomon (2015), First observations of Mercury's plasma mantle by MESSENGER, *Geophys. Res. Lett.*, *42*, 9666–9675, doi:10.1002/2015GL065805.

Domingue D. L., et al. (2014), Mercury's weather-beaten surface: Understanding Mercury in the context of lunar and asteroidal space weathering studies, *Space Sci. Rev.*, *181*, 121–214.

Elphic, R. C., and C. T. Russell (1983), Magnetic flux ropes in the Venus ionosphere: Observations and models, *J. Geophys. Res.*, *88*, 58–72, doi:10.1029/JA088iA01p00058.

Gershman, D. J., J. A. Slavin, J. M. Raines, T. H. Zurbuchen, B. J. Anderson, H. Korth, D. N. Baker, and S. C. Solomon (2013), Magnetic flux pileup and plasma depletion in Mercury's subsolar magnetosheath. *J. Geophys. Res. Space Physics*, *118*, 7181–7199, doi:10.1002/2013JA019244.

Gershman, D. J., J. M. Raines, J. A. Slavin, T. H. Zurbuchen, T. Sundberg, S. A. Boardsen, B. J. Anderson, H. Korth, and S. C. Solomon (2015), MESSENGER observations of multiscale Kelvin-Helmholtz vortices at Mercury. *J. Geophys. Res. Space Physics*, *120*, 4354–4368, doi:10.1002/2014JA020903.

Gershman, D. J., J. C. Dorelli, G. A. DiBraccio, J. M. Raines, J. A. Slavin, G. Poh, and T. H. Zurbuchen (2016), Ion-scale structure in Mercury's magnetopause reconnection diffusion region, *Geophys. Res. Lett.*, *43*, in press, doi:[10.1002/2016GL069163](https://doi.org/10.1002/2016GL069163).

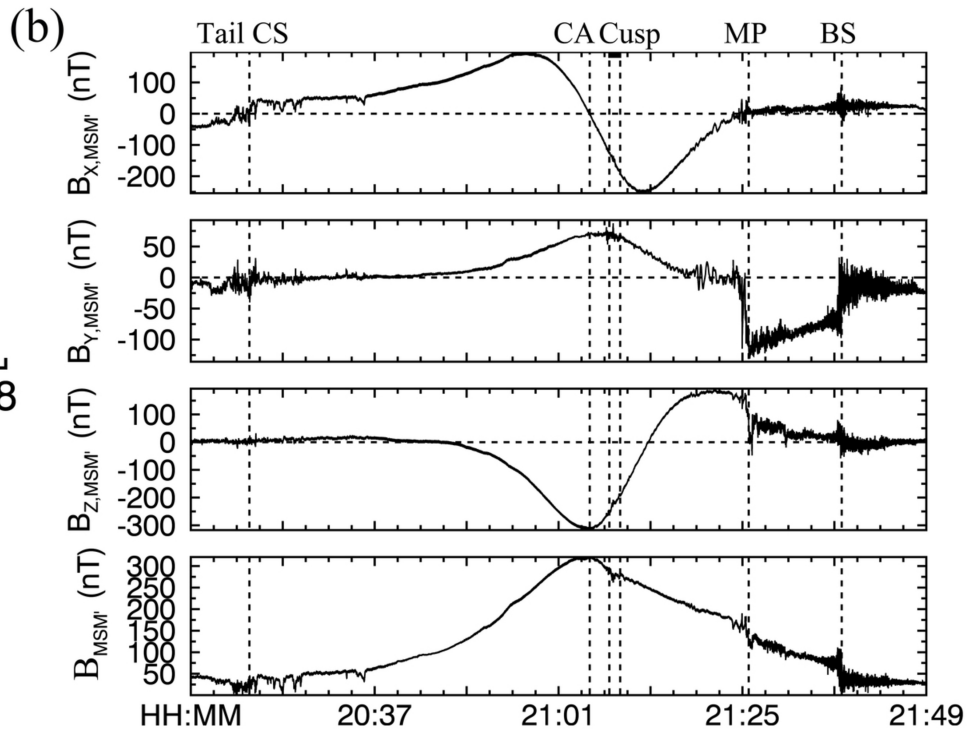
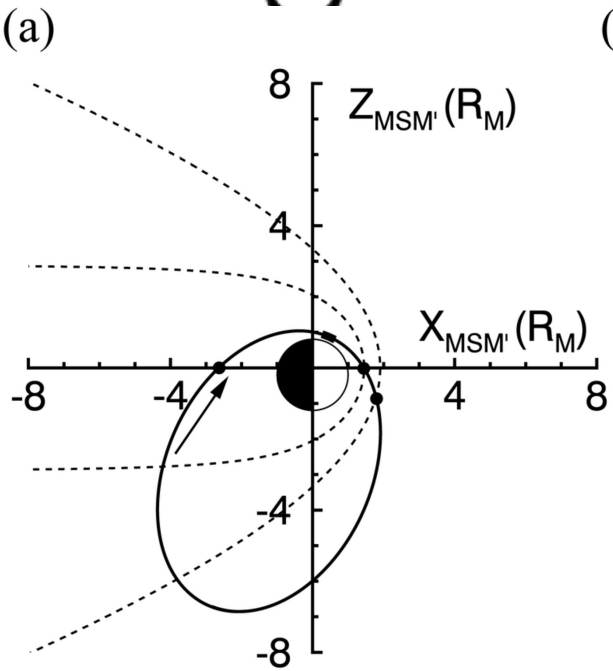
- Hasegawa, A. (1969), Drift mirror instability in the magnetosphere, *Phys. Fluids*, *12*, 2642–2650.
- Hill, T. W., and P. H. Reiff (1977), Evidence of magnetospheric cusp proton acceleration by magnetic merging at the dayside magnetopause, *J. Geophys. Res.*, *82*, 3623–3628, doi:10.1029/JA082i025p03623.
- Imber, S. M., J. A. Slavin, S. A. Boardsen, B. J. Anderson, H. Korth, R. L. McNutt Jr., and S. C. Solomon (2014), MESSENGER observations of large dayside flux transfer events: Do they drive Mercury's substorm cycle?, *J. Geophys. Res. Space Physics*, *119*, 5613–5623, doi:10.1002/2014JA019884.
- Jia, X., J. A. Slavin, T. I. Gombosi, L. K. S. Daldorff, G. Toth, and B. van der Holst (2015), Global MHD simulations of Mercury's magnetosphere with coupled planetary interior: Induction effect of the planetary conducting core on the global interaction. *J. Geophys. Res. Space Physics*, *120*, 4763–4775. doi:10.1002/2015JA021143.
- Johnson, C. L., M. E. Purucker, H. Korth, B. J. Anderson, R. M. Winslow, M. M. H. Al Asad, J. A. Slavin, I. I. Alexeev, R. J. Phillips, M. T. Zuber and S. C. Solomon (2012), MESSENGER observations of Mercury's magnetic field structure. *J. Geophys. Res.*, *117*, E00L14, doi:10.1029/2012JE004217.
- Killen, R. M., and W.-H. Ip (1999), The surface-bounded atmospheres of Mercury and the Moon, *Rev. Geophys.*, *37*, 361–406, doi:10.1029/1999RG900001.
- Lee, L. C., and Z. F. Fu (1985), A theory of magnetic flux transfer at the Earth's magnetopause, *Geophys. Res. Lett.*, *12*, 105–108.
- Liljeblad, E., T. Sundberg, T. Karlsson, and A. Kullen (2014), Statistical investigation of Kelvin-Helmholtz waves at the magnetopause of Mercury, *J. Geophys. Res. Space Physics*, *119*, 9670–9683.
- Lockwood, M., and H. Carlson (1992), Production of polar cap electron density patches by transient magnetopause reconnection, *Geophys. Res. Lett.*, *19*, 1731–1734, doi:10.1029/92GL01993.
- Lockwood, M., and M. F. Smith (1989), Low-altitude signatures of the cusp and flux transfer events. *Geophys. Res. Lett.*, *16*, 879–882.

- Masseti, S., S. Orsini, A. Milillo, and A. Mura (2007), Modelling Mercury's magnetosphere and plasma entry through the dayside magnetopause, *Planet. Space Sci.*, *55*, 1557–1568.
- Ness, N. F., K. W. Behannon, R. P. Lepping, Y. C. Wang, and K. H. Schatten (1974), Observations of magnetic field near Mercury: Preliminary results from Mariner 10, *Science*, *185*, 151–159.
- Newell, P. T., and C.-I. Meng (1987), Cusp width and B_z : Observations and a conceptual model, *J. Geophys. Res.*, *92*, 13,673–13,678.
- Paschmann, G., I. Papamastorakis, W. Baumjohann, N. Sckopke, C. W. Carlson, B. U. Ö. Sommerup, and H. Lühr (1986), The magnetopause for large magnetic shear: AMPTE/IRM observations, *J. Geophys. Res.*, *91*, 11,099–11,115, doi:10.1029/JA091iA10p11099.
- Phan, T. D., J. T. Gosling, G. Paschmann, C. Pasma, J. F. Drake, M. Oieroset, D. Larson, R. P. Lin, and M. S. Davis (2010), The dependence of magnetic reconnection on plasma β and magnetic shear: Evidence from solar wind observations, *Astrophys. J.*, *719*, L199–L203.
- Pokhotelov, O. A., R. Z. Sagdeev, M. A. Balikhin, O. G. Onishchenko, and V. N. Fedun (2008), Nonlinear mirror waves in non-Maxwellian space plasmas, *J. Geophys. Res.*, *113*, A04225, doi:10.1029/2007JA012642.
- Raeder, J. (2006), Flux transfer events: 1. Generation mechanism for strong southward IMF, *Annals Geophys.*, *24*, 381–392, doi:10.5194/angeo-24-381-2006.
- Raines, J. M., D. J. Gershman, J. A. Slavin, T. H. Zurbuchen, H. Korth, B. J. Anderson, G. Gloeckler, and S. C. Solomon (2014), Structure and dynamics of Mercury's magnetospheric cusp: MESSENGER measurements of protons and planetary ions, *J. Geophys. Res. Space Physics*, *119*, 6587–6602, doi:10.1002/2014JA020120.
- Russell, C. T., and R. C. Elphic (1978), Initial ISEE magnetometer results: Magnetopause observations, *Space Sci. Res.*, *22*, 681–715.
- Scurry, P., C. T. Russell, and J. T. Gosling (1994), Geomagnetic activity and the beta dependence of the dayside reconnection rate, *J. Geophys. Res.*, *99*, 14,811–14,814, doi:10.1029/94JA00794.
- Shi, Q. Q., et al. (2009), Spatial structures of magnetic depression in the Earth's high-altitude cusp: Cluster multipoint observations, *J. Geophys. Res.*, *114*, A10202, doi:10.1029/2009JA014283.

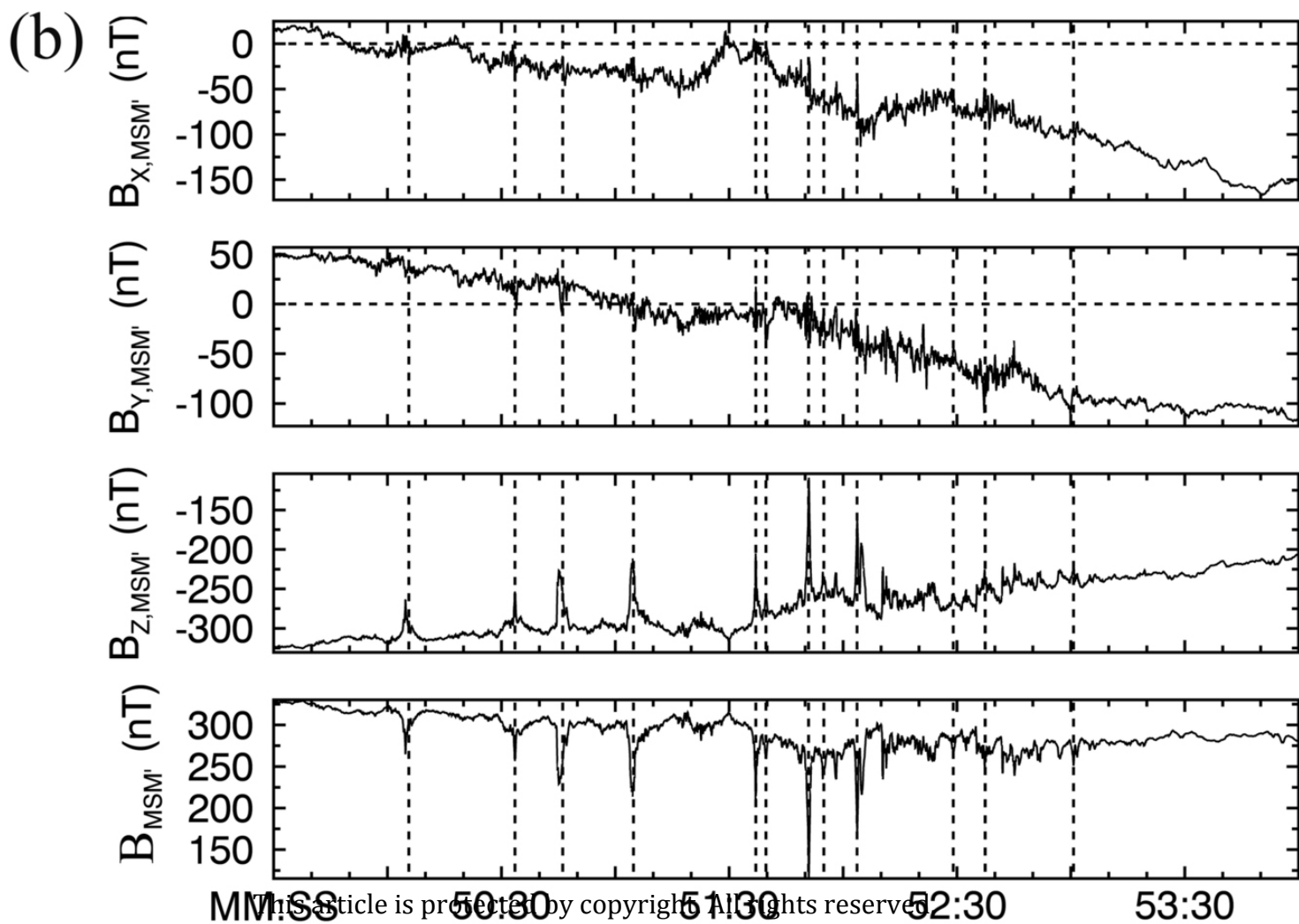
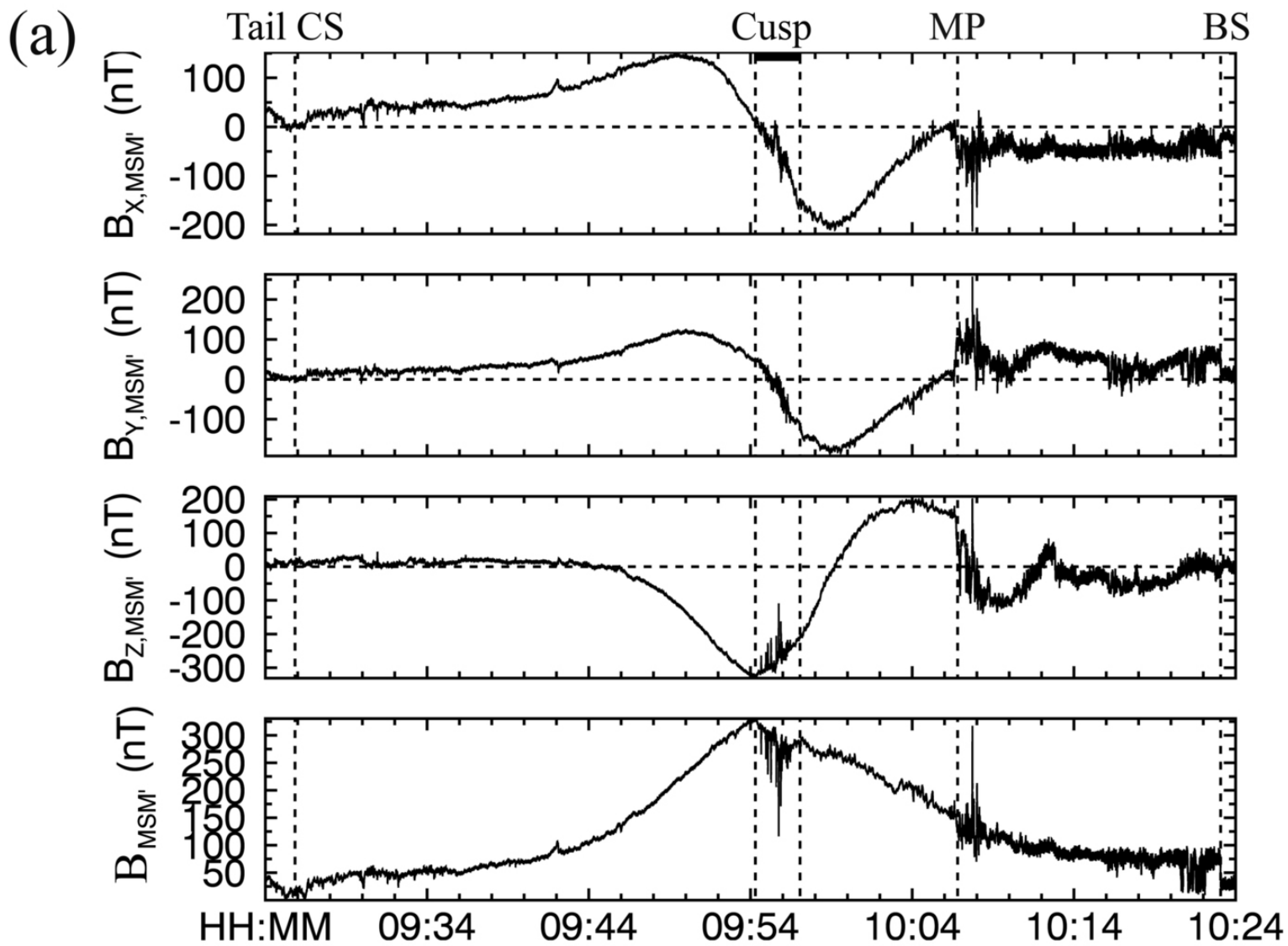
- Shue, J.-H., et al. (1998), Magnetopause location under extreme solar wind conditions, *J. Geophys. Res.*, *103*, 17,691–17,700, doi:10.1029/98JA01103.
- Slavin, J. A., and R. E. Holzer (1979), The effect of erosion on the solar wind stand-off distance at Mercury, *J. Geophys. Res.*, *84*, 2076–2082, doi:10.1029/JA084iA05p02076.
- Slavin, J. A., et al. (2008), Mercury's magnetosphere after MESSENGER's first flyby, *Science*, *321*, 85–89.
- Slavin, J. A., et al. (2009), MESSENGER observations of magnetic reconnection in Mercury's magnetosphere, *Science*, *324*, 606–610.
- Slavin, J. A., et al. (2010), MESSENGER observations of large flux transfer events at Mercury, *Geophys. Res. Lett.*, *37*, L02105, doi:10.1029/2009GL041485.
- Slavin, J. A., et al. (2014), MESSENGER observations of Mercury's dayside magnetosphere under extreme solar wind conditions, *J. Geophys. Res. Space Physics*, *119*, 8087–8116, doi:10.1002/2014JA020319.
- Smith, M. E., and M. Lockwood (1990), The pulsating cusp, *Geophys. Res. Lett.*, *17*, 1069–1072.
- Smith, D. E., et al. (2012), Gravity field and internal structure of Mercury from MESSENGER, *Science*, *336*, 214–217.
- Sonnerup, B. U. Ö., and L. J. Cahill Jr. (1967), Magnetopause structure and attitude from Explorer 12 observations, *J. Geophys. Res.*, *72*, 171–183.
- Sonnerup, B. U. Ö., and M. Scheible (1998), Minimum and maximum variance analysis, in *Analysis Methods for Multi-Spacecraft Data*, edited by G. Paschmann and P. W. Daly, ISSI Scientific Report SR-001, pp. 185–220, European Space Agency, Noordwijk, The Netherlands.
- Sonnerup, B. U. Ö., G. Paschmann, I. Papamastorakis, N. Sckopke, G. Haerendel, S. J. Bame, J. R. Asbridge, J. T. Gosling, and C. T. Russell (1981), Evidence for magnetic field reconnection at the Earth's magnetopause, *J. Geophys. Res.*, *86*, 10,049–10,067, doi:10.1029/JA086iA12p10049.

- Soucek, J., E. Lucek, and I. Dandouras (2008), Properties of magnetosheath mirror modes observed by Cluster and their response to changes in plasma parameters, *J. Geophys. Res.*, *113*, A04203, doi:10.1029/2007JA012649.
- Southwood, D. J. (1987), The ionospheric signature of flux transfer events, *J. Geophys. Res.*, *92*, 3207–3213.
- Southwood, D. J., W. J. Hughes (1983), Theory of hydromagnetic waves in the magnetosphere, *Space Sci. Rev.*, *35*, 301–366.
- Southwood, D. J., and M. G. Kivelson (1993), Mirror instability: 1. Physical mechanism of linear instability, *J. Geophys. Res.*, *98*, 9181–9187.
- Stevens, M. L., and J. C. Kasper (2007), A scale-free analysis of magnetic holes at 1 AU, *J. Geophys. Res.*, *112*, A05109, doi:10.1029/2006JA012116.
- Sundberg, T., S. A. Boardsen, J. A. Slavin, B. J. Anderson, H. Korth, T. H. Zurbuchen, J. M. Raines, and S. C. Solomon (2012), MESSENGER orbital observations of large-amplitude Kelvin-Helmholtz waves at Mercury's magnetopause, *J. Geophys. Res.*, *117*, A04216, doi:10.1029/2011JA017268.
- Swisdak, M., B. N. Rogers, J. F. Drake, and M. A. Shay (2003), Diamagnetic suppression of component magnetic reconnection at the magnetopause, *J. Geophys. Res.*, *108*(A5), 1218, doi:10.1029/2002JA009726.
- Trenchi, L., M. F. Marcucci, G. Pallochia, G. Consolini, M. B. Bavassano Cattaneo, A. M. Di Lellis, H. Rème, L. Kistler, C. M. Carr, and J. B. Cao (2008), Occurrence of reconnection jets at the dayside magnetopause: Double star observations, *J. Geophys. Res.*, *113*, A07S10, doi:10.1029/2007JA012774.
- Tsurutani, R. T., E. J. Smith, R. R. Anderson, K. W. Ogilvie, J. D. Scudder, D. N. Baker, S. J. Barne (1982), Lion roars and nonoscillatory drift mirror waves in the magnetosheath, *J. Geophys. Res.*, *87*, 6060–6072.
- Turner, J. M., L. F. Burlaga, N. F. Ness, and J. F. Lemaire (1977), Magnetic holes in the solar wind, *J. Geophys. Res.*, *82*, 1921–1924.
- Walsh, B. M., J. C. Foster, P. J. Erickson, and D. G. Sibeck (2014), Simultaneous ground- and space-based observations of the plasmaspheric plume and reconnection, *Science*, *343*, 1122–1125, doi:10.1126/science.1247212.

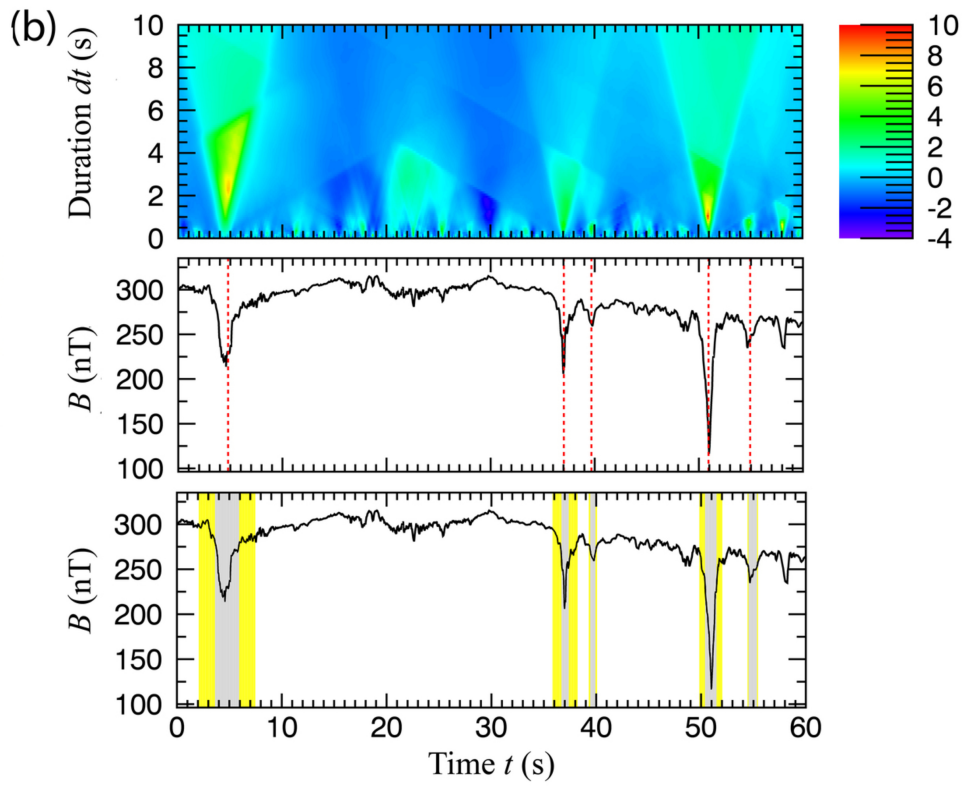
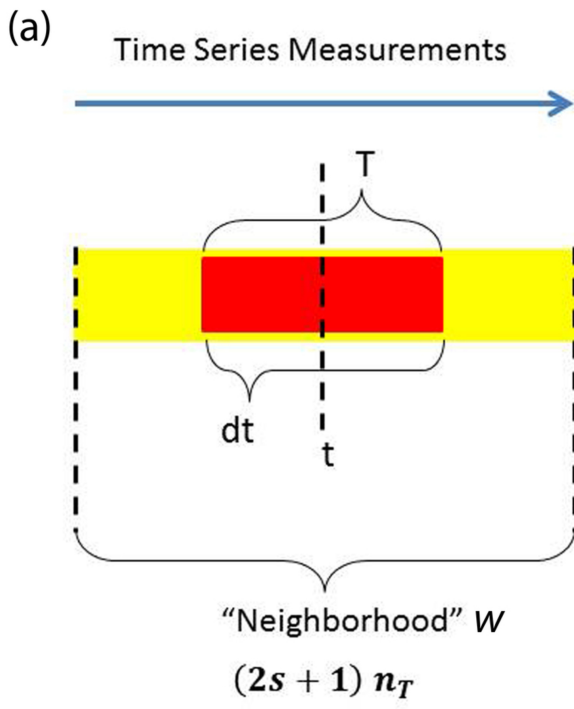
- Winslow, R. M., C. L. Johnson, B. J. Anderson, H. Korth, J. A. Slavin, M. E. Purucker, and S. C. Solomon (2012), Observations of Mercury's northern cusp with MESSENGER's Magnetometer, *Geophys. Res. Lett.*, *39*, L08112, doi:10.1029/2012GL051472.
- Winslow, R. M., B. J. Anderson, C. L. Johnson, J. A. Slavin, H. Korth, M. E. Purucker, D. N. Baker, and S. C. Solomon (2013), Mercury's magnetopause and bow shock from MESSENGER Magnetometer observations, *J. Geophys. Res. Space Physics*, *118*, 2213–2227, doi:10.1002/jgra.50237.
- Winslow, R. M., et al. (2014), Mercury's surface magnetic field determined from proton-reflection magnetometry, *Geophys. Res. Lett.*, *41*, 4463–4470, doi:10.1002/2014GL060258.
- Winterhalter, D. M., M. Neugebauer, B. E. Goldstein, E. J. Smith, S. J. Bame, and A. Balogh (1994), Ulysses field and plasma observations of magnetic holes in the solar wind and their relation to mirror-mode structures, *J. Geophys. Res.*, *99*, 23,371–23,281.
- Xiao, C. J., Z. Y. Pu, Z. W. Ma, S. Y. Fu, Z. Y. Huang, and Q. G. Zong (2004), Inferring of flux rope orientation with the minimum variance analysis technique, *J. Geophys. Res.*, *109*, A11216, doi:10.1029/2004JA010594.



2016JA022552-f01-z-.jpg



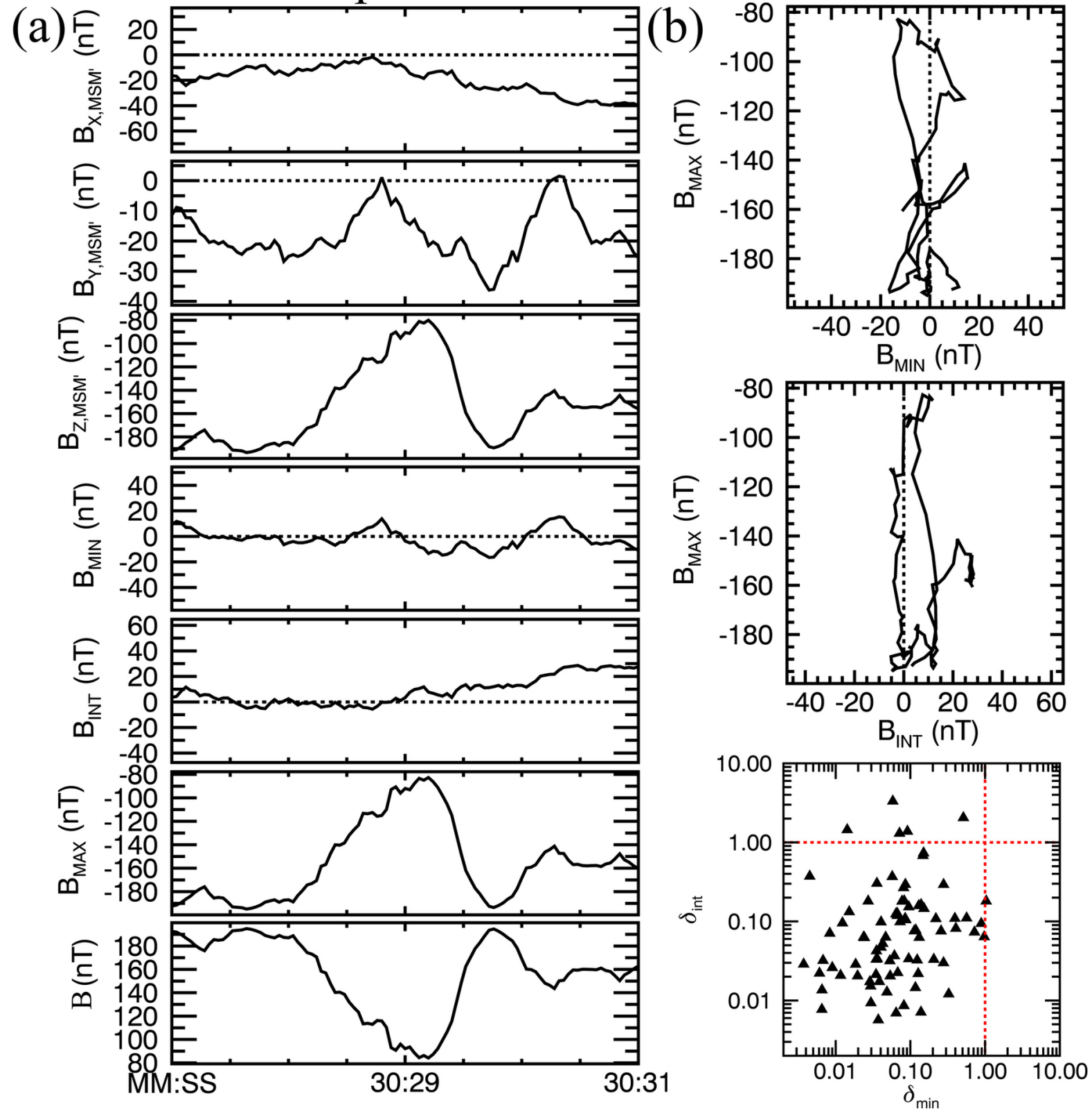
cript



Autl

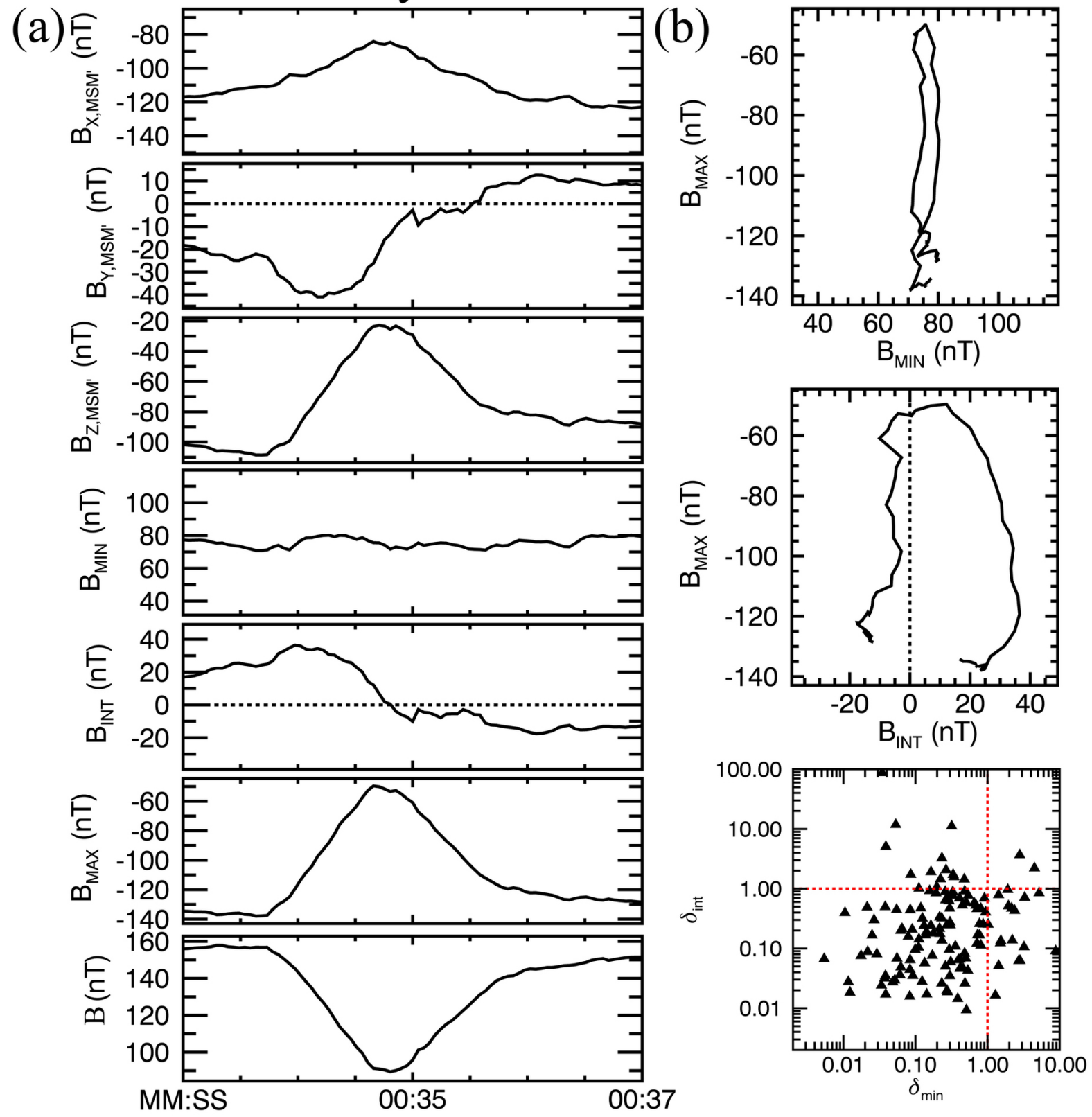
2016JA022552-f03-z-.jpg

23 April 2013 16:30:29 UTC

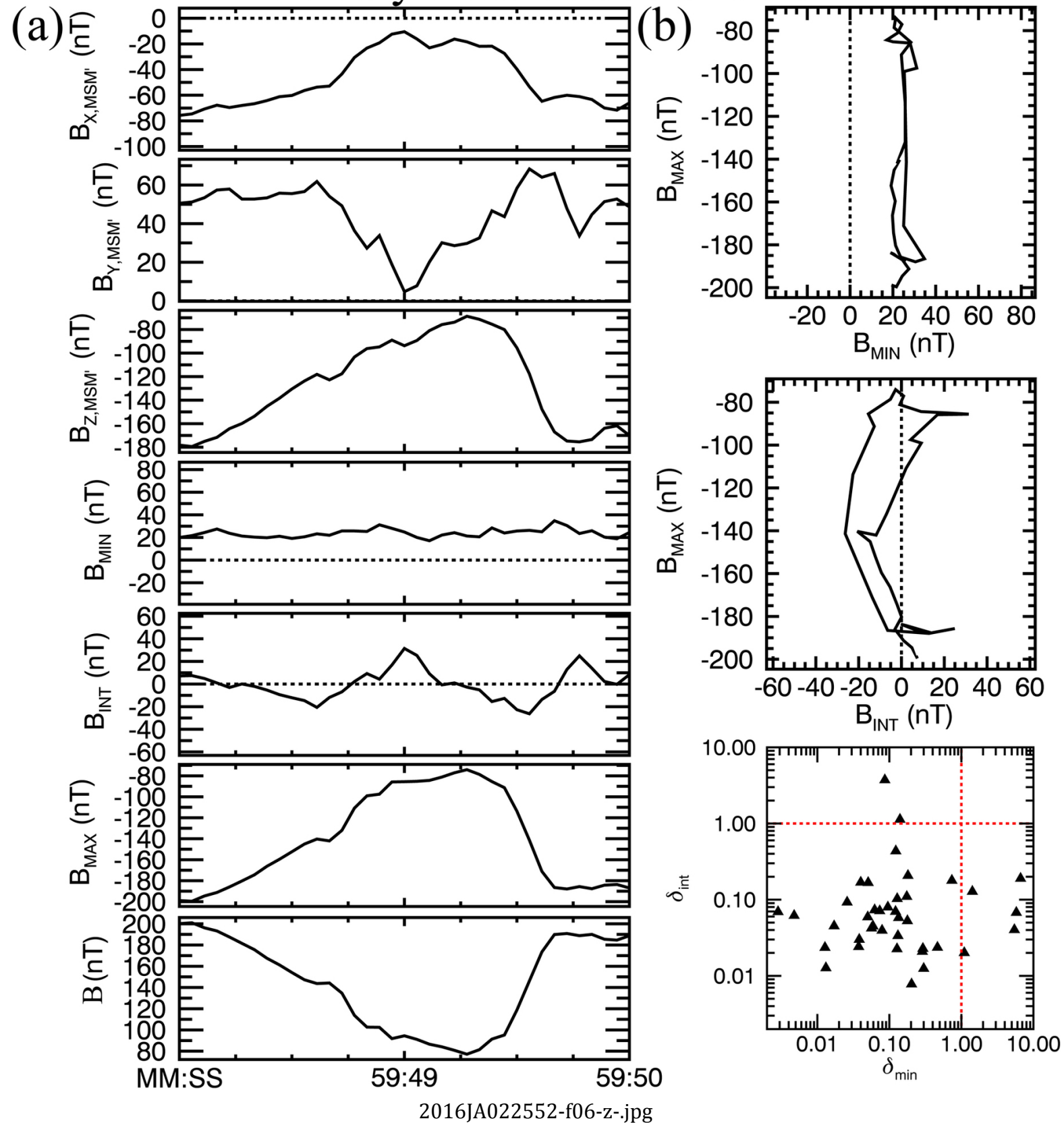


2016JA022552-f04-z-.jpg

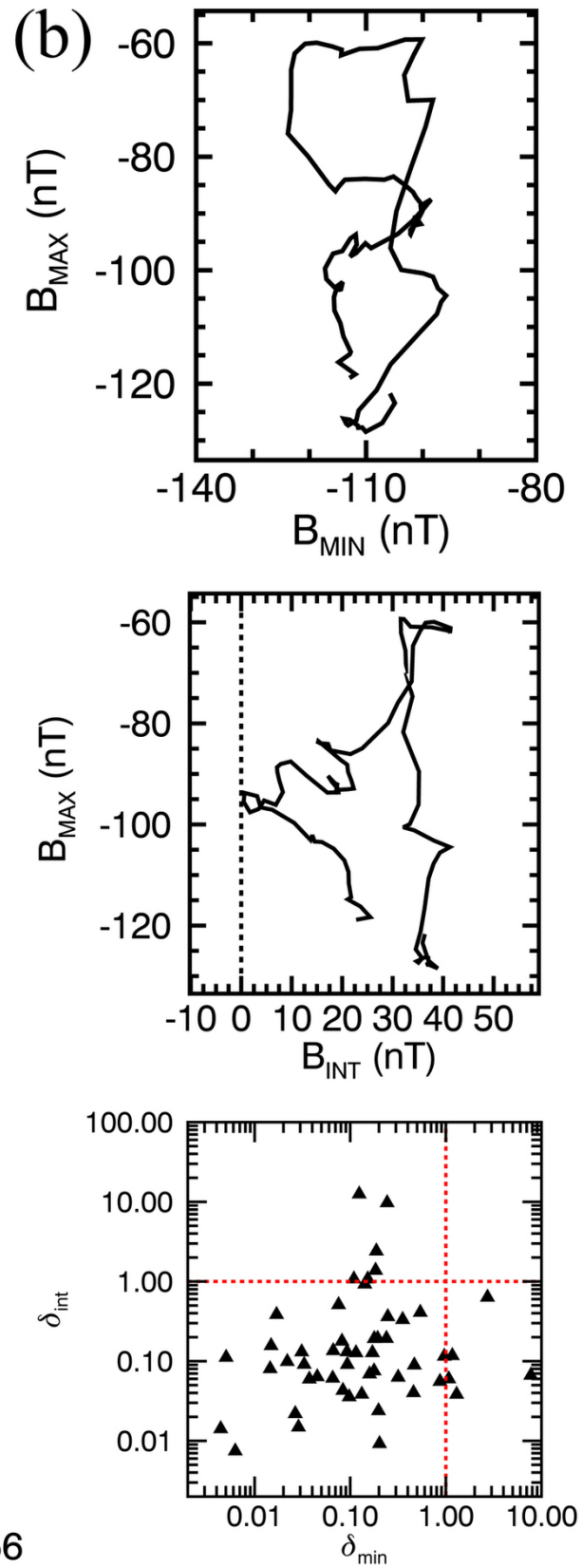
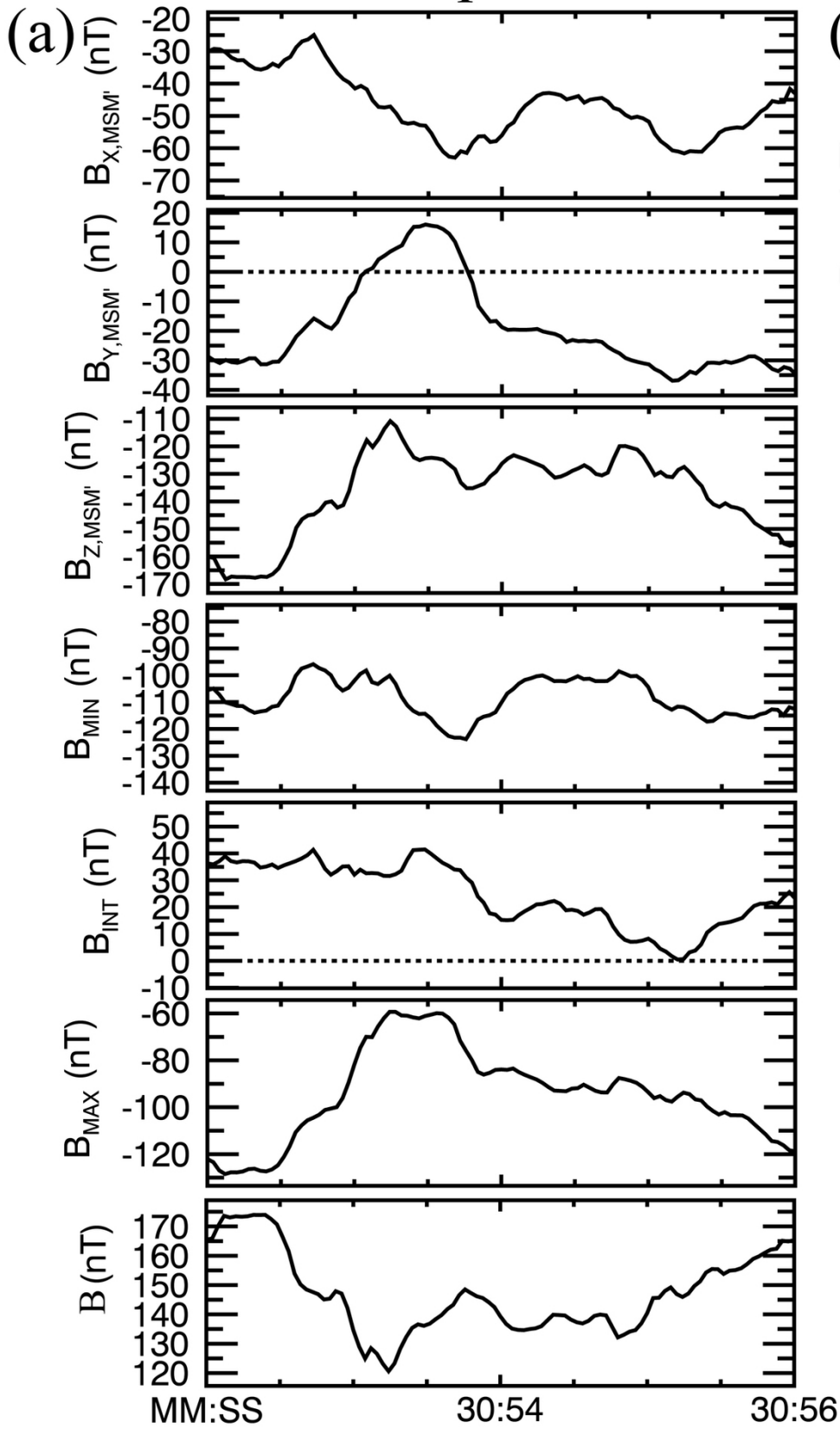
26 July 2013 17:00:36 UTC



27 July 2013 08:59:49 UTC

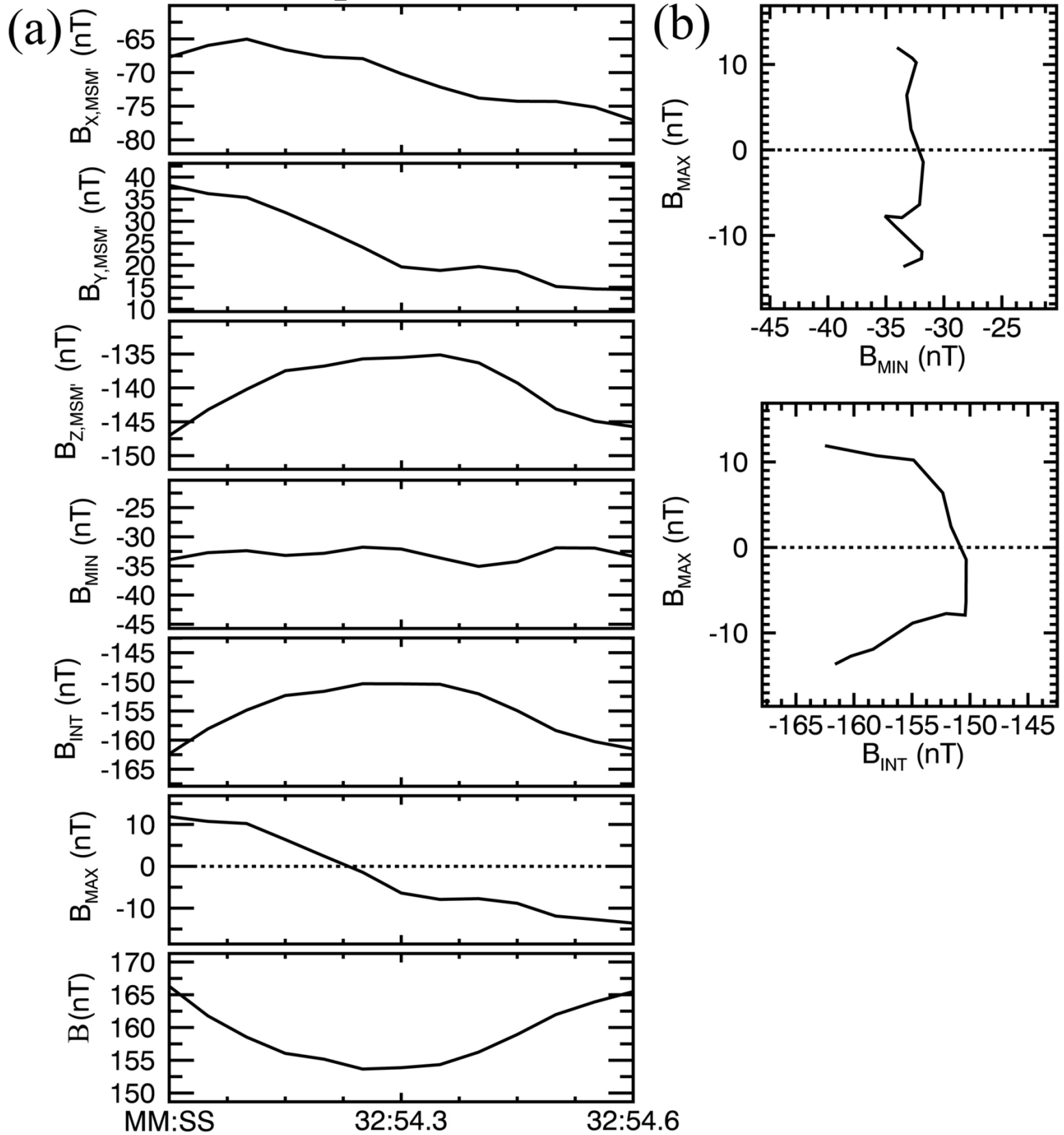


23 April 2013 16:30:54 UTC

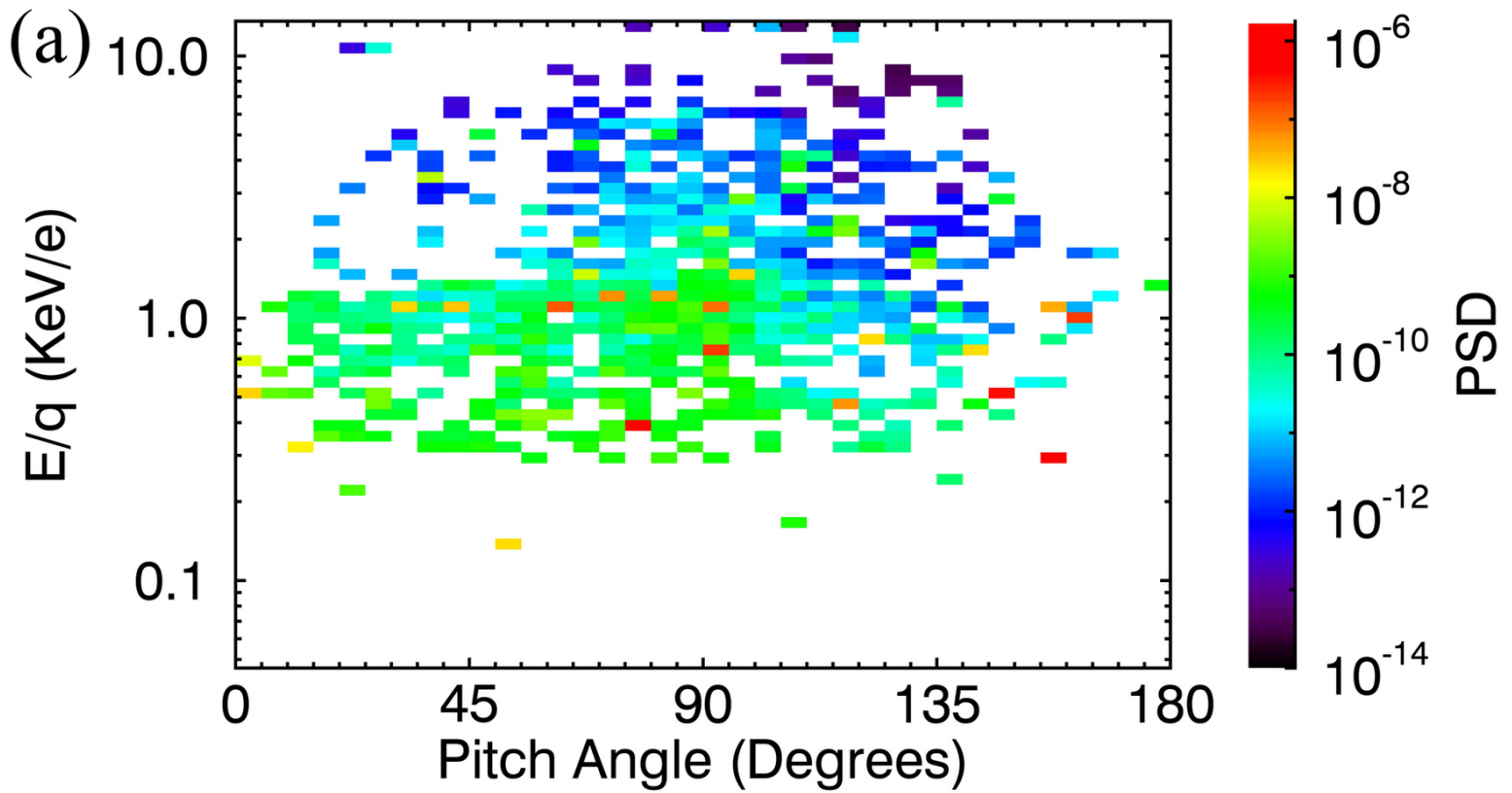


2016JA022552-f07-z-jpg

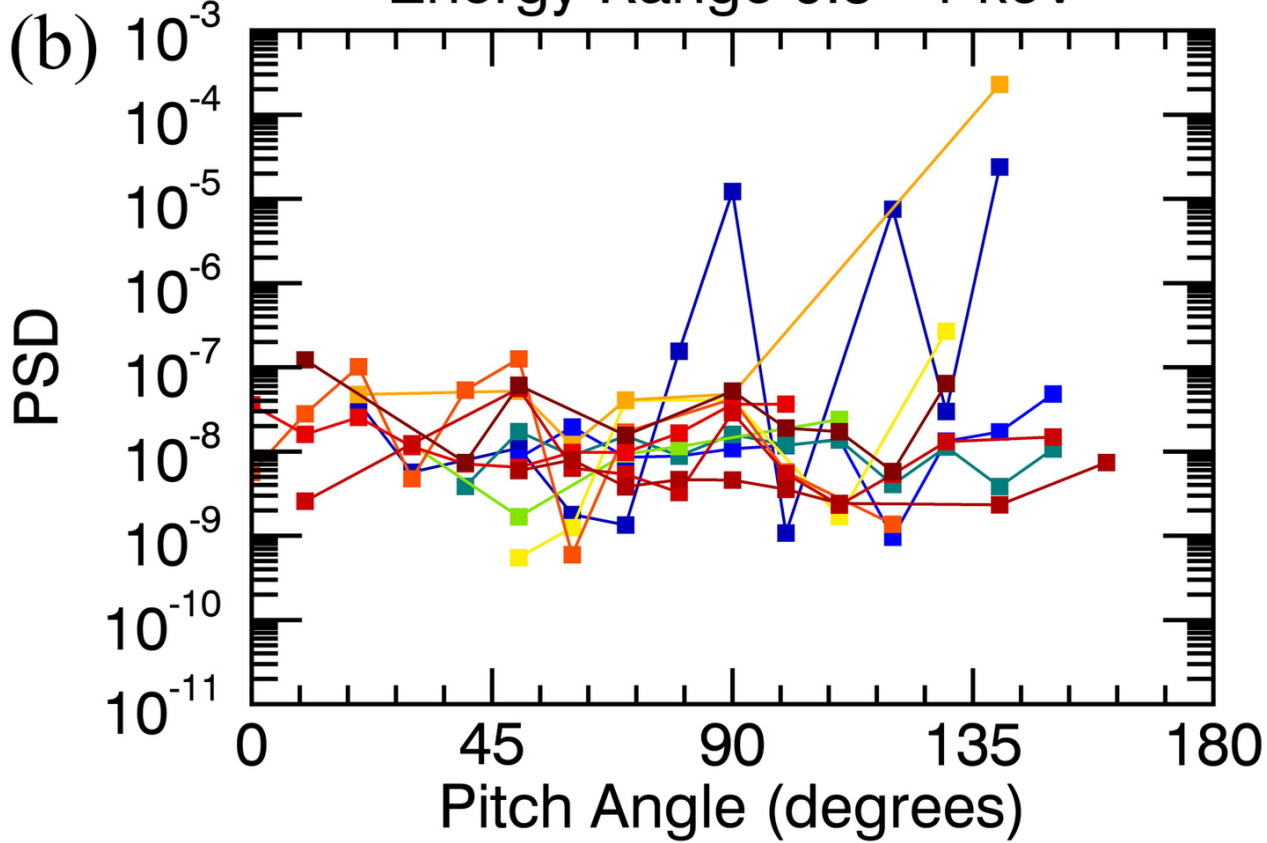
27 April 2013 16:32:54 UTC



2016JA022552-f08-z-jpg



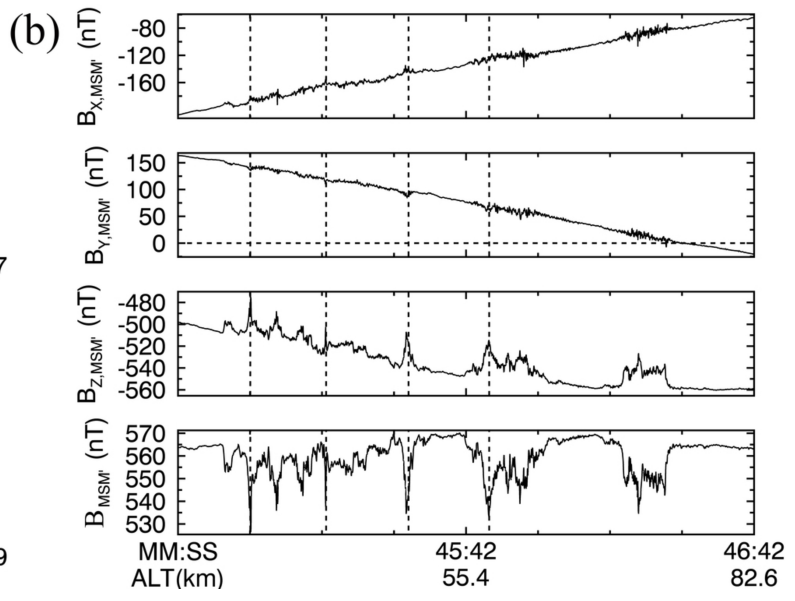
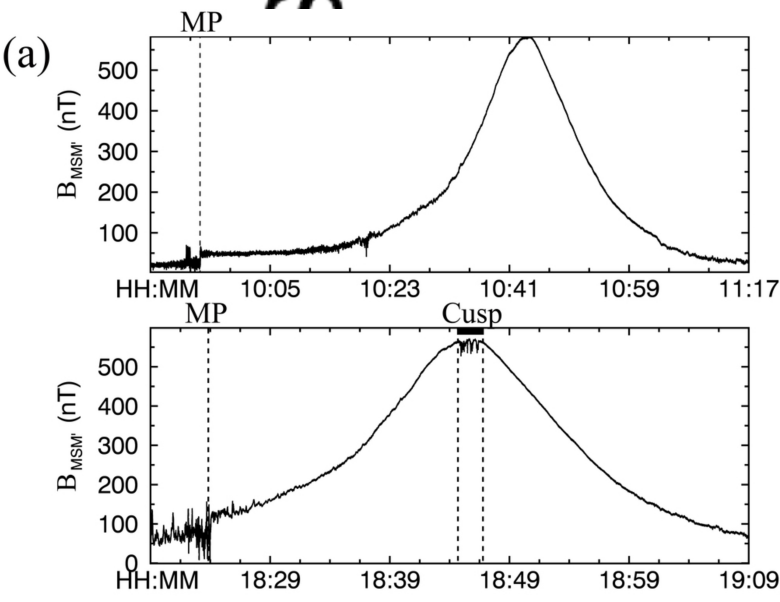
Energy Range 0.5 - 1 keV



2016JA022552-f09-z-.jpg

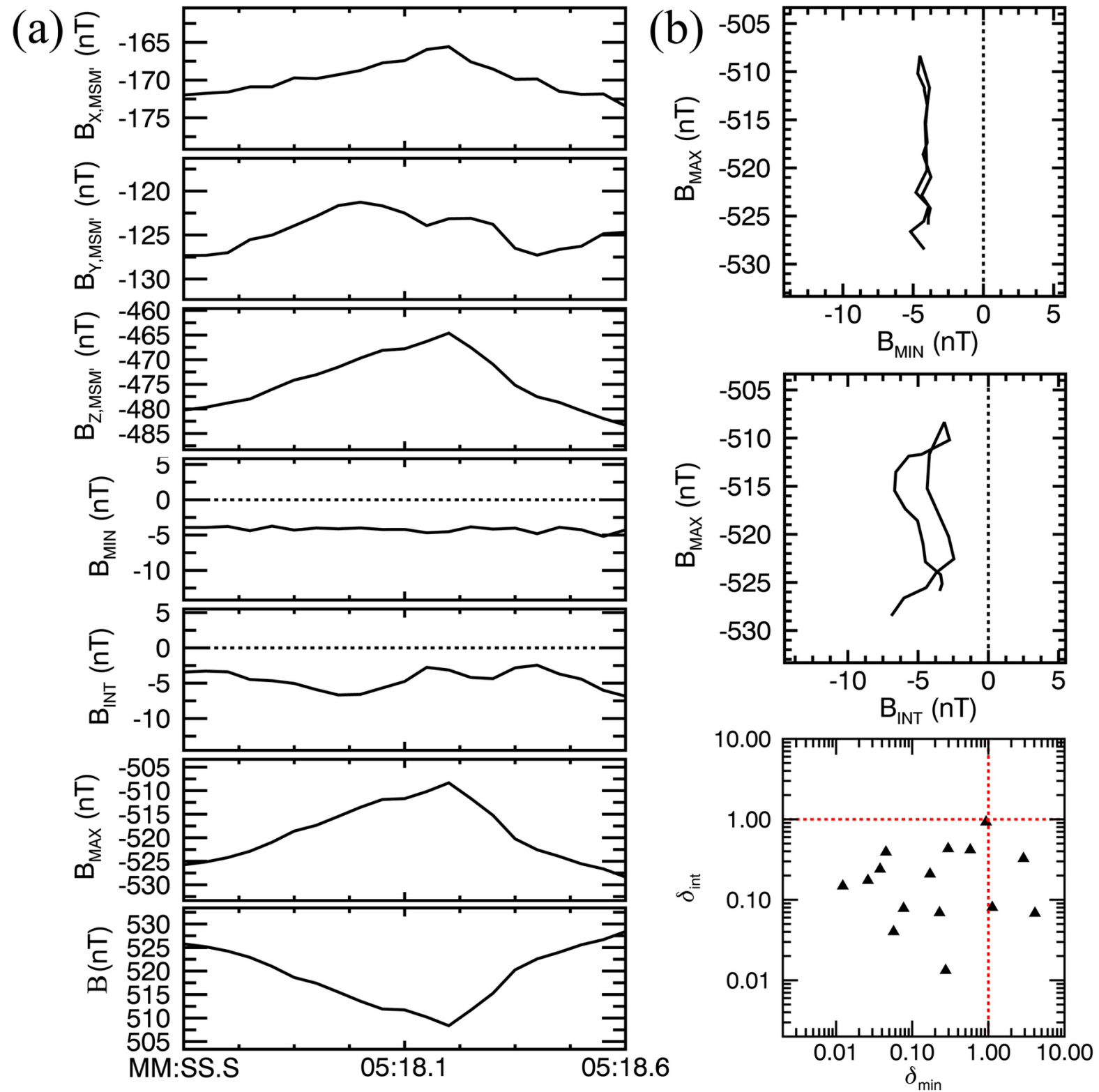
script

Authc



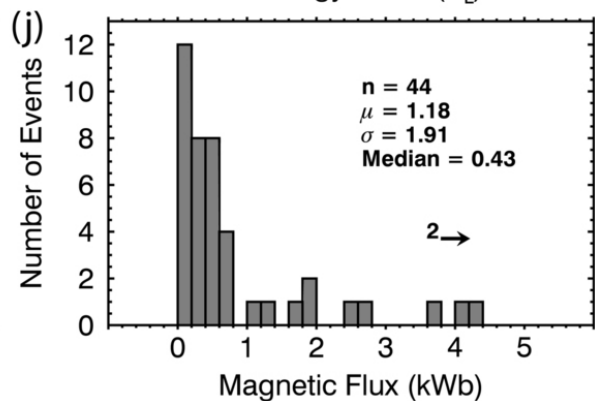
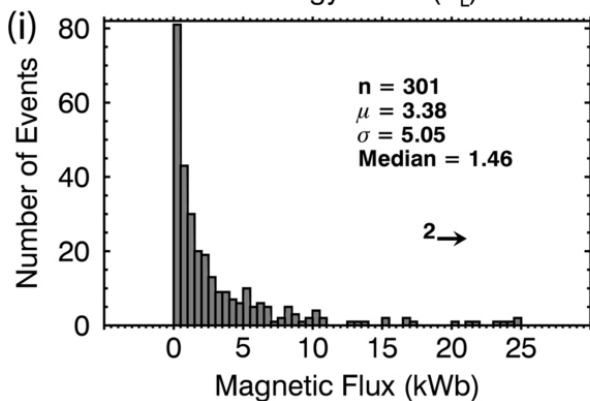
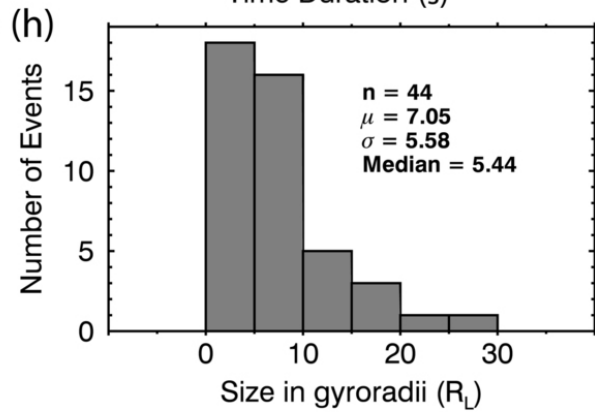
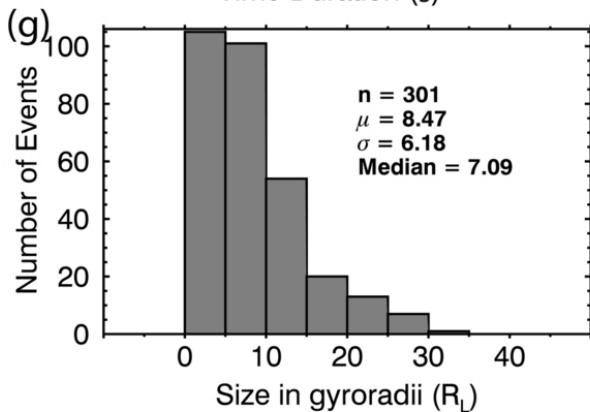
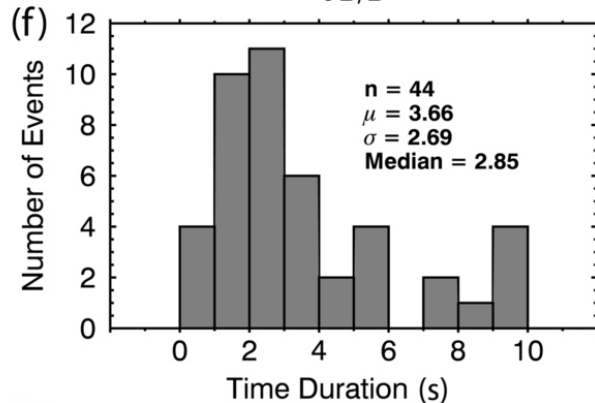
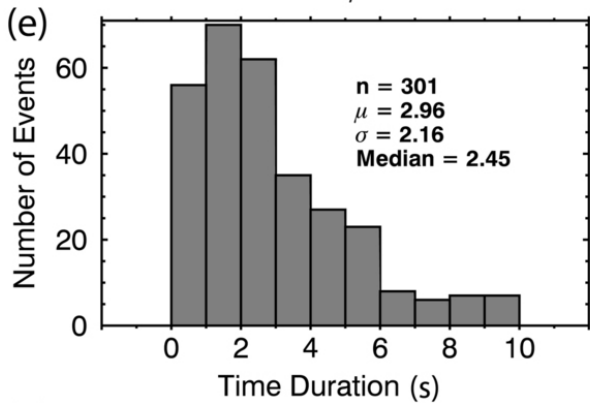
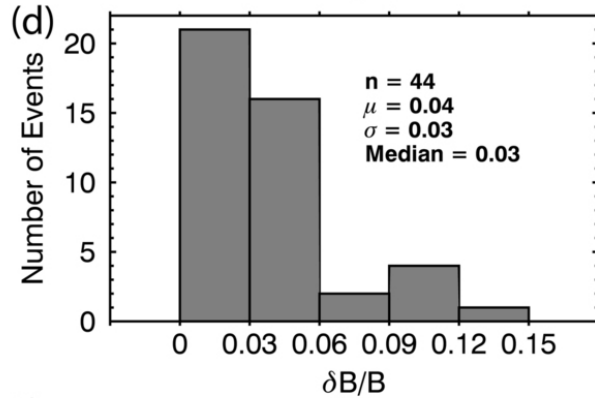
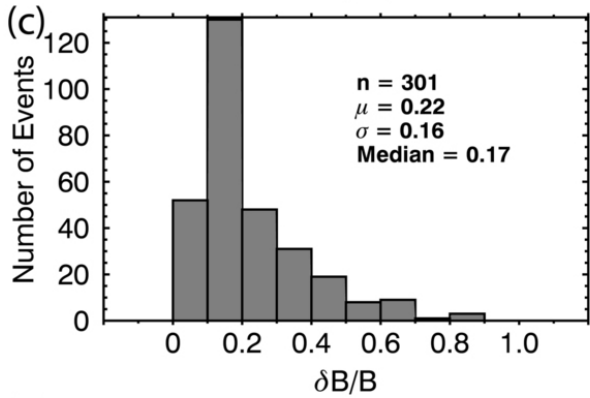
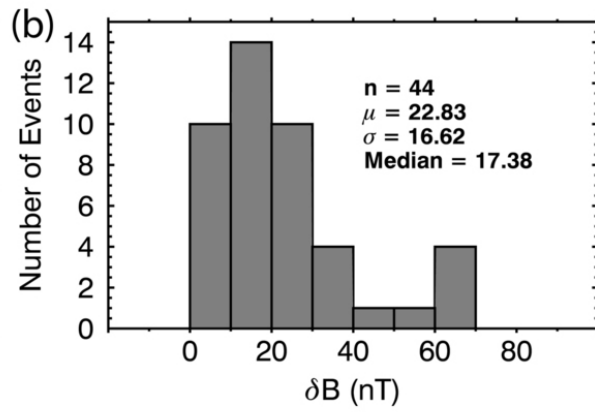
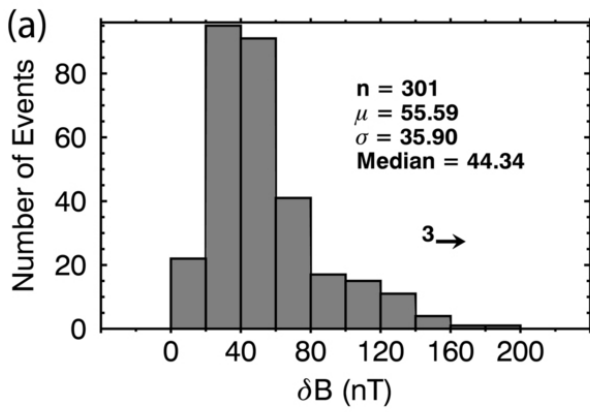
2016JA022552-f10-z.jpg

15 August 2014 17:05:18 UTC



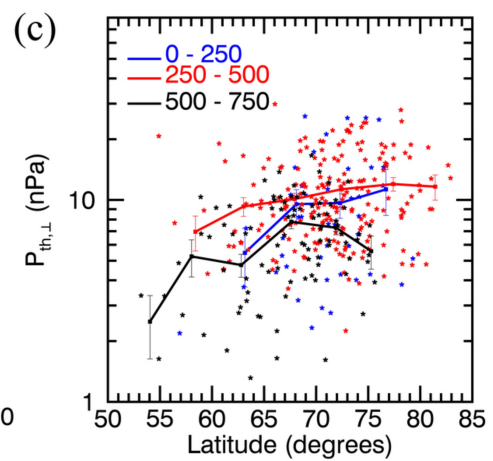
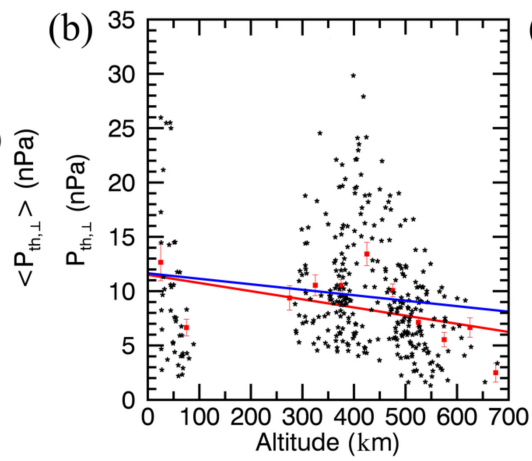
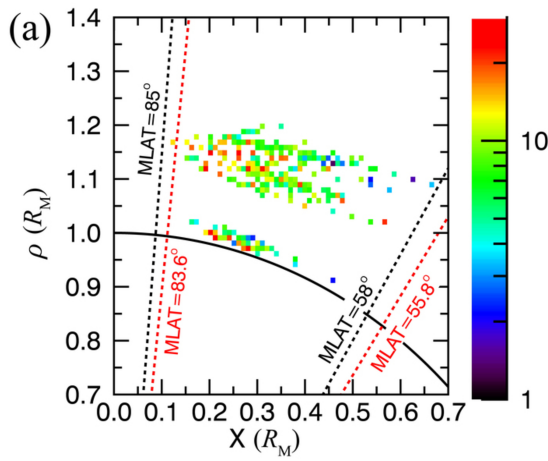
High Altitude

Low Altitude

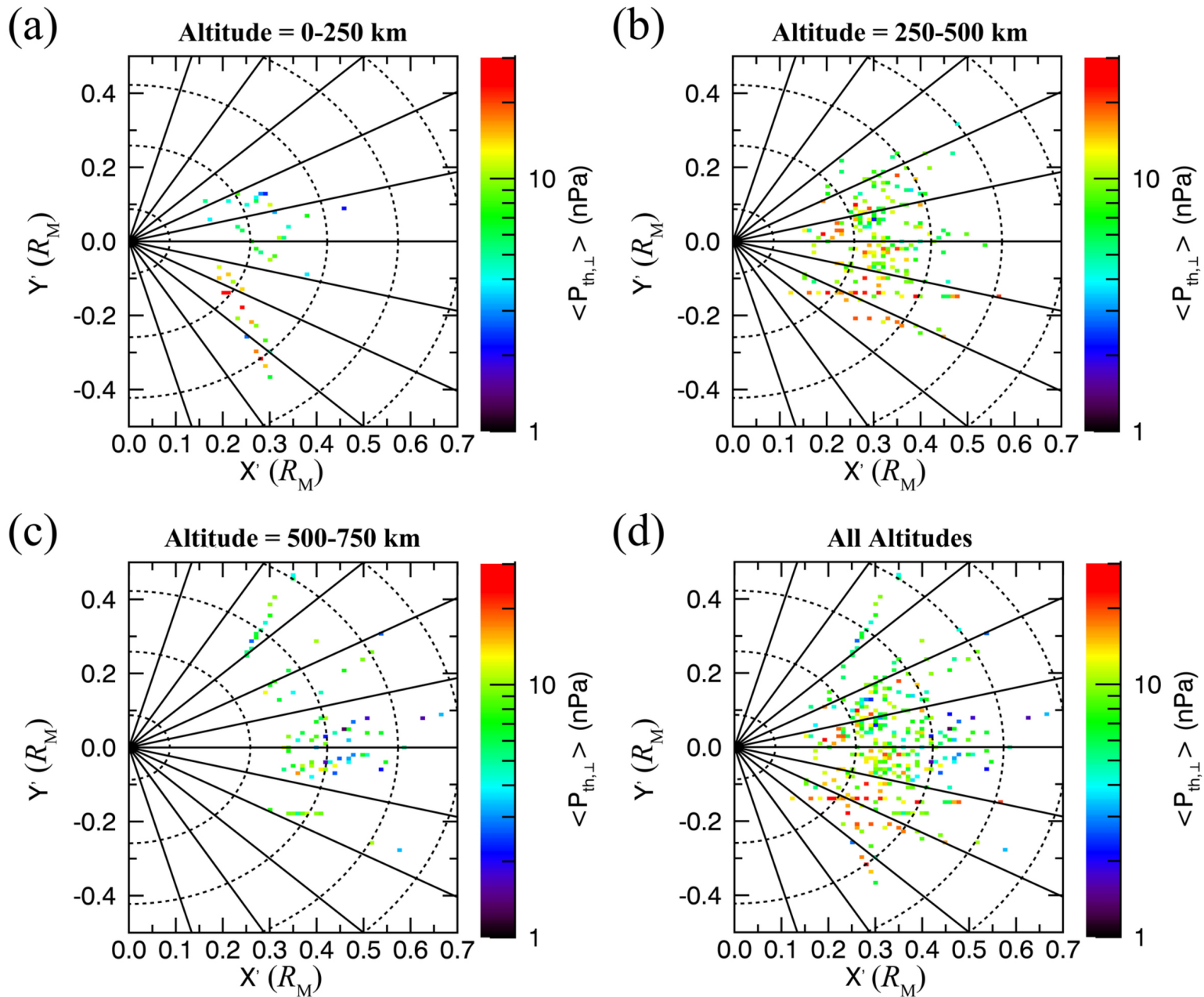


script

Autho



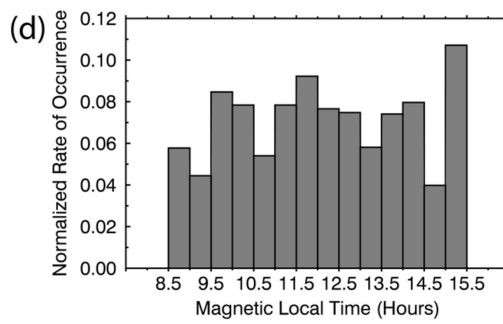
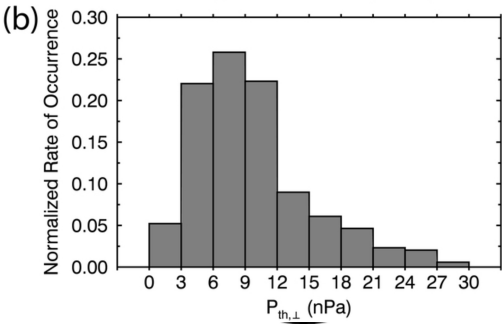
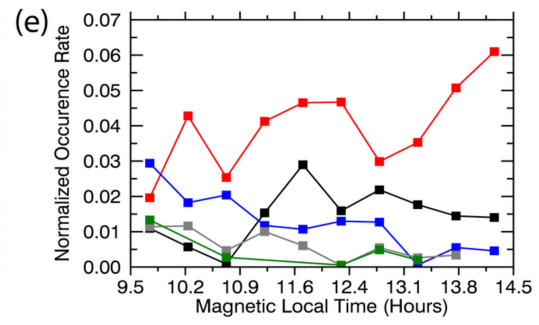
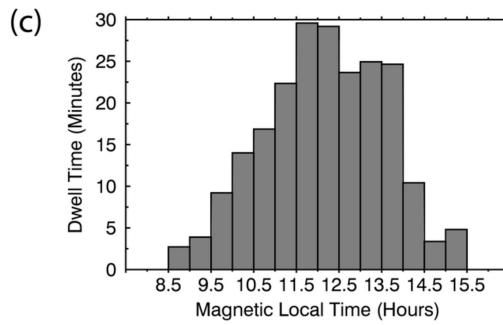
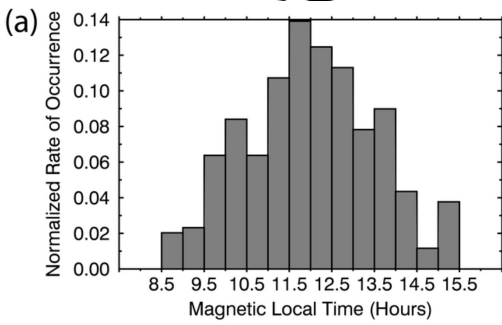
2016JA022552-f13-z-.jpg



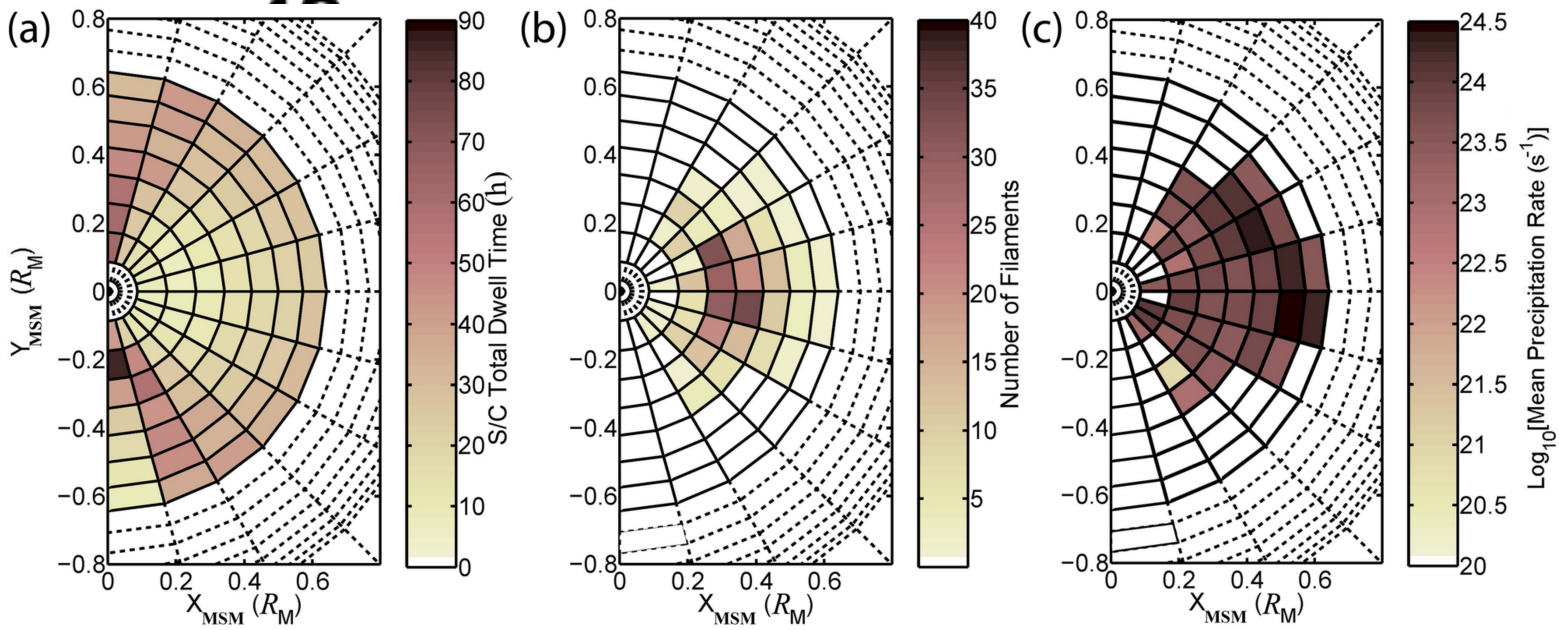
2016JA022552-f14-z-jpg

cript

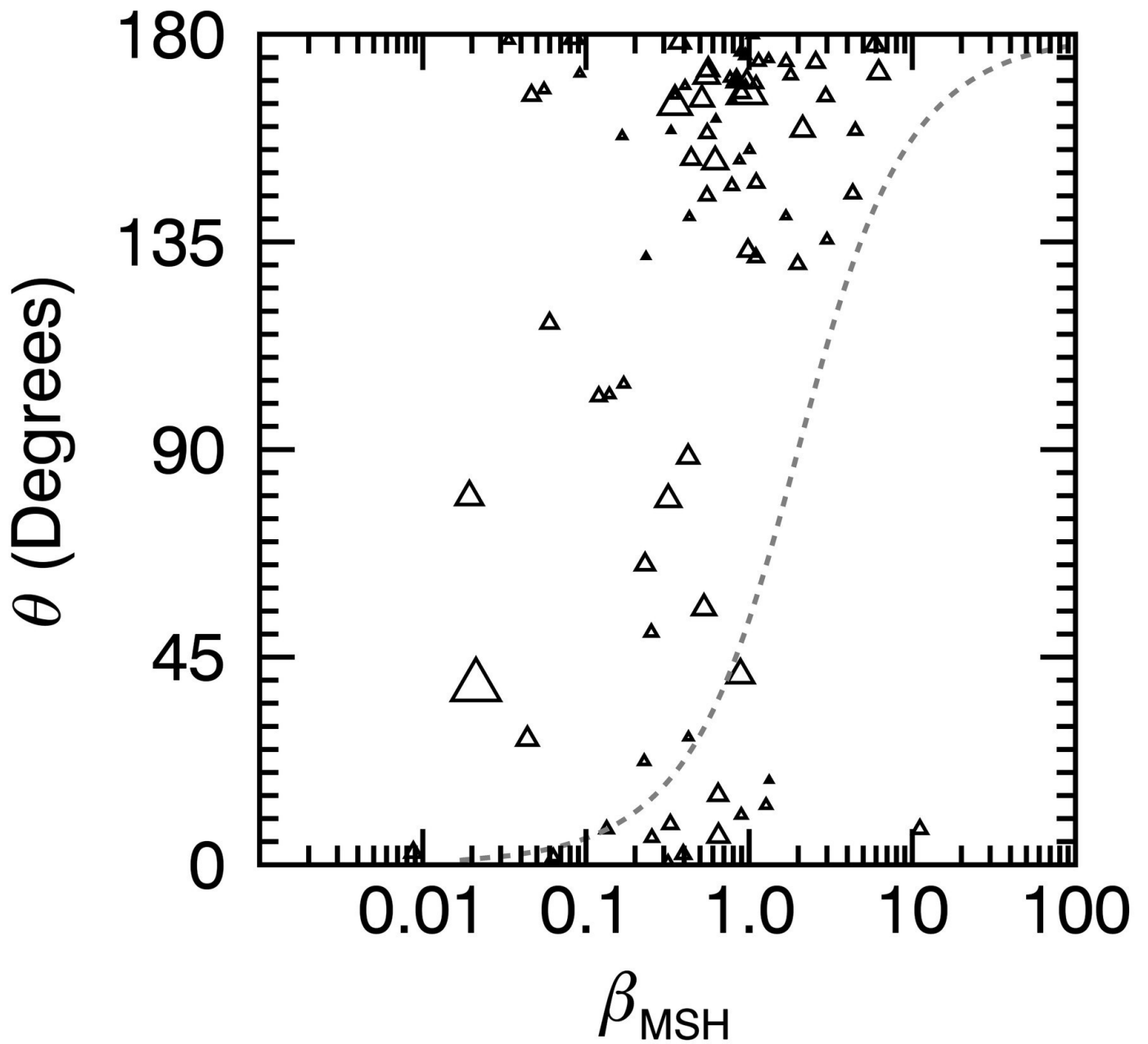
Auth



2016JA022552-f15-z-.jpg



2016JA022552-f16-z-jpg



2016JA022552-f17-z-jpg